Modelling microstructural evolution in binary alloys

Terhi Rautiainen
Linacre College, University of Oxford

Acknowledgements

This research was carried out under the supervision of Prof. Adrian Sutton, to whom I owe big and humble thanks: he had faith and enthusiasm when I had lost mine, he saw ideas and new ways to go where I had got stuck, and he had money to send me off for conferences when he had had enough.

For the good spirits and uplifting working environment I would like to thank all my colleagues in the Materials Modelling Laboratory. Richard Zugic and Steven Kenny deserve especially warm thanks for their efforts in troubleshooting all computer problems well before they encountered me.

Finally, my stay and daily bread in Oxford has financially been possible due to the generosity of Osk. Huttunen Foundation, Jenny and Antti Wihuri Foundation, Finnish Cultural Foundation and British Council.

Kotijoukoille

Modelling microstructural evolution in binary alloys

Terhi Rautiainen
Linacre College, University of Oxford
Thesis submitted for the degree of Doctor of Philosophy
Michaelmas term 1998

Abstract

In this thesis morphologies, coarsening mechanisms and kinetics are examined in a systematic way, when phase separation and subsequent microstructural coarsening is modelled using deterministic mean field and stochastic Monte Carlo methods. For the mean field approach a microscopic diffusion equation due to Khachaturyan is employed, and a variation of it with an environment dependent mobility. Monte Carlo simulations are carried out with vacancy and Kawasaki dynamics, and a residence time algorithm is applied in the vacancy case.

In mean field models microstructural evolution results from a direct minimization of a free energy functional, and the mechanism of atomic diffusion does not appear explicitly. In Monte Carlo models, changes in site occupancies are effected by direct exchanges of neighbouring atoms (Kawasaki dynamics), or through vacancy motion. In this thesis the correspondence between mean field and Monte Carlo models in describing phase transformations in binary alloys is examined. Several examples of cases in which these differences between deterministic and stochastic models affect the phase transformation are given, and the underlying differences are analyzed.

It is also investigated how the choice of diffusion mechanism in the Monte Carlo model affects the microstructural evolution. Most Monte Carlo studies have been carried out with Kawasaki dynamics, although in real metals such direct exchanges are very unlikely to occur. It will be shown how the vacancy diffusion mechanism produces a variety of coarsening mechanisms over a range of temperatures, which the Kawasaki dynamics fails to capture. Consequently, kinetics and resulting morphologies, especially at low temperatures, are affected.

Finally, the question of physicality of time scales in mean field and Monte Carlo models is addressed. Often a linear dependence between Monte Carlo time and real physical time is assumed, although there is no rigorous justification for this. In mean field models, time is defined through the atomic mobility. By examining the effect of a realistic diffusion mechanism in systems undergoing phase transformation, a critical discussion of time scales in microscopic mean field models and a Monte Carlo model with Kawasaki dynamics is presented.

Contents

1 Introduction **1**

1.1 Microstructures - why do they matter? 1

1.2 Aspects of modelling evolving microstructures 3

1.3 Objectives of this thesis 3

2 Deterministic mean field methods **5**

2.1 Darken's phenomenological theory for diffusion 5

2.2 Cahn-Hilliard theory for early stages of spinodal decomposition 8

2.2.1 Stability of homogeneous solid solution 10

2.2.2 Kinetics of the early stages of phase separation 11

2.3 Khachaturyan's kinetic field theory 13

2.3.1 Microscopic mean field equation 13

2.3.2 Continuum kinetic equations 14

2.3.3 On the origin of Cahn and Ginzburg-Landau equations 16

2.4 Salje rate law 18

2.5 Martin-Vaks mean field equation 20

2.6 Microscopic cluster activation method 23

2.7 Discussion 25

3 Driving force for transformation **27**

3.1 Introduction 27

3.2 Bragg-Williams theory 28

3.3 Landau theory 32
3.4 Elastic energy 34
3.5 Implementing Khachaturyan's microscopic mean field equation in reciprocal space 38
3.5.1 Applications of the kinetic field theory - some results reviewed 42
3.6 Discussion 44

4 Stochastic Monte Carlo methods 46
4.1 Diffusion mechanisms in solids 46
4.2 Kawasaki and vacancy dynamics 48
4.3 Residence time Monte Carlo algorithm 50
4.3.1 First order algorithm 50
4.3.2 Second order algorithm 52
4.4 Incorporation of elastic energy 56
4.5 Discussion 57

5 Coarsening theories 60
5.1 The role of interface energy 60
5.2 Gibbs-Thompson effect 61
5.3 Ostwald ripening and LSW-theory 62
5.4 Huse's extension to LSW-theory 67
5.5 Binder-Stauffer theory for particle diffusion 69
5.6 Discussion 72

6 Comparison of the methods 74
6.1 Introduction 74
6.2 Review of the models 76
6.2.1 Microscopic mean field model 76
6.2.2 Monte Carlo model with vacancy dynamics 77
6.3 Phase separation and coarsening 78
6.3.1 Morphologies 79
6.3.2 Coarsening mechanisms 85

6.3.3 Kinetics . . . 93
6.3.4 Physicality of time scales in the models . . . 99
6.3.5 Dynamical scaling in Monte Carlo models . . . 101
6.4 Simultaneous ordering and phase separation . . . 104
6.4.1 Morphologies . . . 105
6.4.2 Kinetics . . . 109
6.5 Phase separation and coarsening in three dimensions . . . 111
6.5.1 Morphologies . . . 112
6.5.2 Kinetics . . . 115
6.6 Discussion . . . 117

7 Future challenges **121**
7.1 Improving the atomic diffusion mechanism(s) . . . 121
7.2 Elastic energy and dissimilar elastic moduli . . . 123
7.3 Semicoherent interfaces and motion of dislocations . . . 124
7.4 Rafting in NiAl superalloys . . . 124

A Mean field phase diagram **127**

B Discretization of Cahn equation **130**

C Elastic energy approximation **132**

D Energies at interfaces **135**
D.1 Interface energies . . . 135
D.1.1 Pure A and B phases . . . 135
D.1.2 Ordered particles in a disordered matrix . . . 136
D.2 Vacancy binding energies to interfaces . . . 137
D.2.1 Pure A and B phases: $\epsilon^{AA} = \epsilon^{BB}$ . . . 137
D.2.2 Pure A and B phases: $\epsilon^{AA} \neq \epsilon^{BB}$ . . . 138
D.2.3 Ordered particles in a disordered matrix . . . 139

Chapter 1

Introduction

1.1 Microstructures - why do they matter?

When a piece of metallic material is looked at with the naked eye, it often seems smooth and homogeneous. However, glance through a microscope may give quite a different view - instead of homogeneous material, one is likely to see structures: particles, bands, aligned precipitates or rafts. Some examples of the variety of microstructures observed in metallic materials are shown in Fig. 1.1. These microstructures are important in many practical applications of our everyday life, since many material properties - how hard it is, how much load it can bear, how it fractures - are determined by them. However, over time microstructures develop into forms with a lower free energy. These give a more stable microstructural configuration, but often also less desirable material properties. Often the microstructural evolution can be made slow enough by suitable alloying and processing treatments to allow a reasonable life span for practical applications, such as railways, bridges or gas turbines.

An unexpected degradation may result in serious consequences. In spinodal decomposition the solute atoms of the alloy enrich without energy barrier to form particles or interconnected solute regions in a solvent matrix. This was observed, for example, in water coolant pipes of nuclear power reactors. These pipes were originally built from stainless steel to prevent corrosion. Later in use, however, it was found that in the initially homogeneous alloy the iron and chromium components had separated, causing a drastic change in the fracture properties

The image originally presented here cannot be made freely available via ORA due to copyright reasons.

Figure 1.1: (a) Micrograph of Ag-rich zones in AlAg alloy [1]. (b) Microstructures observed during ageing of AlCu alloy [1]. (c) Rafting in NiAl superalloy [2].

from ductile to brittle. Ductile material behaves like a piece of chewing gum: it yields, and does not break up immediately. Brittle fracture, on the other hand, is often catastrophic: once it has started, it is practically impossible to stop it - it is like breaking a window glass! In case of water coolant pipes the pressure changes of water could be enough to initiate fracture, which is an extremely undesirable event to happen.

Microstructural changes can also occur under external loading. This is experimentally a well-known phenomenon in technologically important NiAl superalloys, which are used in demanding high temperature applications. An unloaded structure consists of ordered cubic particles in a disordered matrix. When external load is applied, like in turbine blades as a result of the centrifugal force, these particles rearrange and coagulate. As the size of ordered particles grows, elastic strains are generated within the material, since the lattice constant between the matrix and particles usually differ slightly from each other. With increasing particle size, elastic strains are released through interface dislocations. As a result, the strength of the superalloy decreases dramatically. These examples demonstrate that once an alloy with desirable properties is obtained, its stability over time and under external loading has to be considered.

1.2 Aspects of modelling evolving microstructures

When an alloy is rapidly cooled into an ordered phase regime, or heated rapidly into the disordered regime, it tends to lower its free energy by undergoing a sequence of structural and compositional changes. Typical phenomena observed during phase transformations are nucleation and growth of new phase particles from the parent matrix, and coarsening of the multi-phase structure. These non-equilibrium processes are governed by transformation kinetics. In spite of substantial theoretical and experimental efforts, the general theory of the morphological evolution and kinetics of ordering and phase separation in alloys are much less understood than static aspects of phase stability. Therefore the role of modelling in understanding the processes and mechanisms underlying the microstructural evolution in alloys is attracting increasing interest amongst materials scientists and physicists.

The challenges in modelling phase transformations in alloys lie in the time and length scales involved: the time span over which phase separation and coarsening occurs may cover several orders of magnitudes, from seconds to years, and the sizes of precipitates can vary from atomic distances to micrometers. For example, a spherical particle of radius $\sim$ 10 nm, which is a typical particle size in Fig. 1.1, contains about 10^5 atoms. Therefore detailed description of entire microstructures at the atomic level is unrealistic, and attempts to tackle the problem from first principles are rarely, if ever, fruitful. Over the years various kinetic rate equations originating from dynamics of spin systems and thermodynamic considerations have been put forward, and despite their success, there still remains plenty of scope for improvement.

1.3 Objectives of this thesis

In this thesis I will discuss some commonly used methods for modelling phase transformations in binary alloys: their origins, applicability and validity in describing microstructural changes. This thesis is *not* aimed to be a study of any particular experimental system, observed phenomenon or transformation mechanism, but rather a critical glance at the state of the current modelling "toolbox". It has to be kept in mind that models and methods *always* involve a number of assumptions, approximations and simplifications. These in turn may result in un-

physicalities and inevitably in wrong predictions, some of which will be discussed in this thesis. I will concentrate on the early stages of phase transformation, when the average particle sizes are small enough to be described by atomic scale models, and particle-matrix interfaces remain coherent.

Chapter 2 gives an overview of deterministic mean field models. The pioneering work in this field was done in the 50's by John Cahn, and the development of ideas since those days will be followed. Chapter 3 goes deeper into mean field models, and discusses the formulation of the driving force for the transformation. In chapter 4 another category of modelling technique is presented, namely stochastic Monte Carlo methods. Kawasaki and vacancy diffusion mechanisms are discussed, and the residence time algorithm for vacancy Monte Carlo model is introduced. Chapter 5 outlines some theories for coarsening kinetics, which have been tested over the years against both experimental systems and computer simulations to understand coarsening behaviour in real alloys. A goal of this thesis is to compare deterministic mean field and stochastic Monte Carlo approaches in modelling phase separation and coarsening of the microstructure, which chapter 6 is devoted to. The main questions considered are: how do the deterministic mean field and stochastic Monte Carlo models differ in describing phase separation and coarsening in binary alloys? how does the choice of dynamics (vacancy or Kawasaki) in Monte Carlo models affect the microstructural evolution? what is the meaning of time in mean field and Kawasaki Monte Carlo models? to what extent do two dimensional simulations reflect the behaviour in realistic three dimensional systems? Finally, chapter 7 considers some further questions prompted by this research, and outlines some unresolved problems, bottlenecks and challenges in modelling evolving microstructures in binary alloys.

Chapter 2

Deterministic mean field methods

In this chapter some deterministic kinetic equations for modelling microstructural evolution in alloys are discussed. Darken's and Cahn's theories, dating back to 40's and 50's, are amongst the earliest breakthroughs in modelling diffusion and early stages of phase separation in solid solutions. Although the understanding of transformation phenomena has since been improved, these theories deserve to be reviewed not only as pioneering studies, but because many of these ideas are still in use.

Many deterministic approaches used these days, such as Cahn-Hilliard and Khachaturyan kinetic equations, are based on direct minimization of a free energy functional, and are developed without reference to the actual mechanism of atomic migration. More detailed theories should rely on a realistic description of the atomistic diffusion mechanism. The Martin-Vaks mean field kinetic equation is a step towards this direction, since it captures the environment dependence of the atomic mobility. As an example of a method that does not utilize explicit free energy formulation, the microscopic cluster activation method is discussed. Rather than minimizing the free energy directly, it approximates the microscopic master equation for diffusion at the atomic level.

2.1 Darken's phenomenological theory for diffusion

In the 1940's Darken developed a phenomenological theory for diffusion, which is based on Gibbs' idea that diffusion occurs down the chemical potential gradient rather than down the

concentration gradient. Later Bardeen and Herring developed these ideas to a more general theory, which can be applied to any number of components. Consider an alloy containing components A,B,C... and vacancies V, which can formally be treated as one of the alloy components. If the diffusion rate of each species is proportional to the gradient of the chemical potential, the diffusion flux (in one dimension for simplicity) for the α component is

$$J_\alpha = -c_\alpha M_\alpha^{'} \frac{\partial \mu_\alpha}{\partial x} \tag{2.1}$$

where μ_α is the chemical potential per atom, and c_α is the concentration. The gradient of the chemical potential can be understood as the average diffusion force on the atom, and $M_\alpha^{'}$ is the mobility (per atom) of α type atoms. The flux of α atoms does not necessarily depend only on the chemical potential of its own type of atoms, but may also be affected by the gradient of chemical potentials of other components of the alloy, and of the vacancies. In that case Eq. (2.1) becomes

$$J_\alpha = -\sum_\beta c_\beta M_{\alpha\beta}^{'} \frac{\partial \mu_\beta}{\partial x} - c_v M_{\alpha v}^{'} \frac{\partial \mu_v}{\partial x}. \tag{2.2}$$

Instead of writing mobilities per atom, we can express mobilities per unite volume as $M_{\alpha\beta} = c_\beta M_{\alpha\beta}^{'}$, and write Eq. (2.2) as

$$J_\alpha = -\sum_\beta M_{\alpha\beta} \frac{\partial \mu_\beta}{\partial x} - M_{\alpha v} \frac{\partial \mu_v}{\partial x}. \tag{2.3}$$

If the total number of lattice sites remains constant during diffusion, there is a compensating net flow of vacancies moving in the opposite direction to the atoms:

$$J_v = -\sum_\alpha J_\alpha. \tag{2.4}$$

Writing Eq. (2.3) for vacancies in the right hand side of Eq. (2.4) we obtain

$$M_{v\beta} = -\sum_\alpha M_{\alpha\beta}. \tag{2.5}$$

Assuming Onsager relations, $M_{\alpha\beta} = M_{\beta\alpha}$ and $M_{v\beta} = M_{\beta v}$, Eq. (2.3) can now be written as

$$J_\alpha = -\sum_\beta M_{\alpha\beta} \frac{\partial(\mu_\beta - \mu_v)}{\partial x} \tag{2.6}$$

which is the general form of the diffusion equation, if vacancies are present. From this - by making certain assumptions - some more familiar but less general equations may be derived. If vacancies are everywhere in local thermal equilibrium, $\nabla\mu_v = 0$, we have

$$J_\alpha = -\sum_\beta M_{\alpha\beta} \frac{\partial \mu_\beta}{\partial x}. \tag{2.7}$$

The fluxes, for example, for A and B atoms in a binary alloy in this case are

$$J_A = -M_{AA}\frac{\partial \mu_A}{\partial x} - M_{AB}\frac{\partial \mu_B}{\partial x} \tag{2.8}$$

$$J_B = -M_{BB}\frac{\partial \mu_B}{\partial x} - M_{BA}\frac{\partial \mu_A}{\partial x}. \tag{2.9}$$

Infinitesimal changes in chemical potentials of A and B species are related through the Gibbs-Duhen equation [1]

$$-c_A d\mu_A = c_B d\mu_B \tag{2.10}$$

and we can also express the gradient of the chemical potential as

$$\frac{\partial \mu_A}{\partial x} = \frac{\partial \mu_A}{\partial \ln c_A}\frac{1}{c_A}\frac{\partial c_A}{\partial x}. \tag{2.11}$$

With Eqs. (2.10) and (2.11) Eq. (2.8) becomes

$$\begin{aligned} J_A &= -\frac{\partial \mu_A}{\partial \ln c_A}\left(\frac{M_{AA}}{c_A} - \frac{M_{AB}}{c_B}\right)\frac{\partial c_A}{\partial x} \\ &= -\frac{\partial \mu_A}{\partial \ln c_A}(M'_{AA} - M'_{AB})\frac{\partial c_A}{\partial x} \\ &= -D_A\frac{\partial c_A}{\partial x}. \end{aligned} \tag{2.12}$$

[1] Gibbs-Duhen equation actually assumes that the $A-B$ alloy is in equilibrium, but in that case there would be no diffusion. In practise this means that deviations from equilibrium must be very small.

D_A is the diffusion coefficient for A atoms:

$$D_A = \frac{\partial \mu_A}{\partial \ln c_A}(M'_{AA} - M'_{AB}) \tag{2.13}$$

and for B atoms similarly

$$D_B = \frac{\partial \mu_B}{\partial \ln c_B}(M'_{BB} - M'_{BA}). \tag{2.14}$$

These two diffusion coefficients are generally unequal, so that the components diffuse through the crystal lattice at different rates. As a result, there will be a mass flow of atoms relative to the lattice, which is opposite to the vacancy flow. For a binary alloy the vacancy flow is

$$J_v = -(J_A + J_B) = (D_A - D_B)\frac{\partial c_A}{\partial x}. \tag{2.15}$$

This is called the Kirkendall effect, which was first observed experimentally in 1947: inert molybdenium wires, which were wound around a block of α-brass, and encapsulated in a block of pure copper were found to move owing to the differences in diffusivities of the alloy components. If diffusion took place by atomic exchanges, rather than through vacancy hopping, we would have $\sum_\alpha J_\alpha = 0$ and $D_A = D_B$, and there would be no net flow of atoms relative to the lattice, and no Kirkendall effect. The Kirkendall effect is therefore indirect evidence that diffusion takes place by a vacancy mechanism.

2.2 Cahn-Hilliard theory for early stages of spinodal decomposition

Spinodal decomposition can occur in a solid solution when it is quenched into a miscibility gap (Fig. 2.1.(a)). It refers to the initial stages of the phase transformation, when there is no barrier for nucleation. The alloy is thermodynamically unstable to small fluctuations that produce A-rich and B-rich regions, and decrease the total free energy. In principle, this process can take place in alloys where the free energy has a negative curvature, $d^2G/dc^2 < 0$. The

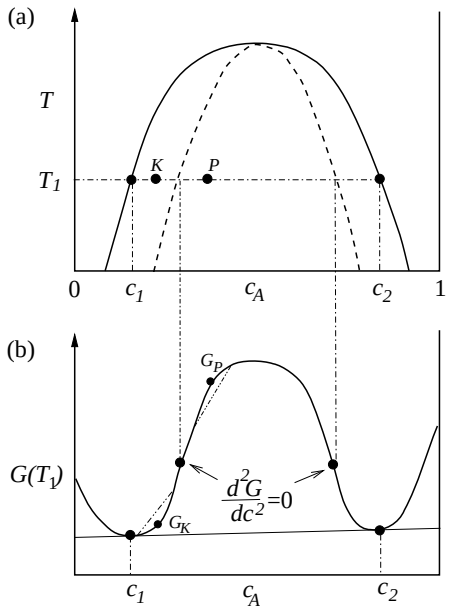


Figure 2.1: (a) Phase diagram with a miscibility gap. Solid line is the coexistence curve and dashed line shows the chemical spinodal. Within the spinodal there is no energy barrier for phase separation, but within the metastable region between the spinodal and coexistence curve fluctuations are needed to seed phase separation. (b) Free energy curve of the system at $T = T_1$ showing the inflection points, and equilibrium compositions, c_1 and c_2, of the two phases.

points of inflection, where $d^2G/dc^2 = 0$ (Fig. 2.1.(b)), determine the chemical spinodal curve [2], which is the dashed line in Fig. 2.1.(a). An alloy quenched to point P in Fig. 2.1.(a) lies within the spinodal, and free energy in Fig. 2.1.(b) decreases monotonically following compositional fluctuations. Outside the spinodal, such as point K, the alloy is in the metastable regime. Small variations in composition result in an increase in free energy, which will subsequently decrease only if sufficiently large nuclei are formed. Therefore, at point K phase separation proceeds through a nucleation and growth mechanism rather than spinodal decomposition. A common example of a metallic alloy exhibiting spinodal decomposition is a Al-rich Al-Zn alloy. It is probable that spinodal decomposition occurs in all alloy systems which have a miscibility gap, but the mechanism may often be obscured by heterogeneous nucleation at grain boundaries or dislocations.

[2] In real systems, where fluctuations are important, the boundary between spinodal decomposition and nucleation is not sharp. Strictly speaking, the spinodal curve can be defined exactly only in mean field models, as shown in appendix A.

2.2.1 Stability of homogeneous solid solution

Cahn and Hilliard's phenomenological theories [3–6] are amongst the most successful theories of the early stages of phase separation. In Refs. [5, 6] Cahn derived some common features of spinodal decomposition. He tested the stability of an initially homogeneous solution against infinitesimal composition variations of the form

$$c - c_0 = A \cos \beta x. \tag{2.16}$$

The alloy is considered as a continuum with solute composition c, which is a continuous function of position. For an isotropic solid solution the total free energy is

$$F = \int_V [f'(c) + \kappa(\nabla c)^2] dV \tag{2.17}$$

where $f'(c)$ is the free energy [3] of a unit volume of homogeneous material of composition c, and $\kappa(\nabla c)^2$ represents the increase in free energy due to composition gradients, i.e. interfaces. Since during the early stages of the phase separation the interfaces between A rich and B rich regions are very diffuse, the second term in Eq. (2.17) is assumed to be sufficient to describe the regions between different composition. By expanding $f'(c)$ about the average composition c_0

$$f'(c) = f'(c_0) + (c - c_0)(\frac{\partial f'}{\partial c})_{c=c_0} + \frac{1}{2}(c - c_0)^2(\frac{\partial^2 f'}{\partial c^2})_{c=c_0} \tag{2.18}$$

the difference in free energy due to compositional variations of the form of Eq. (2.16) can be written as

$$\frac{\Delta F}{V} = \frac{A^2}{4}(\frac{\partial^2 f'}{\partial c^2} + 2\kappa\beta^2). \tag{2.19}$$

With $\partial^2 f'/\partial c^2 > 0$ the solution is stable with respect to infinitesimal sinusoidal fluctuations of all wavelengths. If $\partial^2 f'/\partial c^2 < 0$, the solution is unstable with respect to fluctuations of

[3] The form of $f'(c)$ will be discussed in chapter 3.

wavelengths greater than $2\pi/\beta$. If $\kappa > 0$ (otherwise there would be no surface tension, and no stability even outside the spinodal), the criterion for instability reads as

$$2\pi/\beta = [8\pi^2\kappa/|\partial^2 f'/\partial c^2|]^{\frac{1}{2}}. \tag{2.20}$$

This shows that as the spinodal is approached the critical wavelength approaches infinity. The analysis can be extended to arbitrary composition fluctuations, which can always be described by Fourier components. Because of their orthogonality the total change in free energy is the sum of the free energy accompanying each component. Hence only the individual sinusoidal fluctuations need to be considered in testing the stability of the system: if it is stable to all of them individually, it is also stable to all infinitesimal fluctuations.

2.2.2 Kinetics of the early stages of phase separation

Next we follow Cahn's analysis in determining the kinetics of early stages of phase separation [5]. The local chemical potential is the variational derivative of the free energy

$$F = \int_V f[c, \nabla c, \mathbf{x}]dV. \tag{2.21}$$

with respect to $c(\mathbf{x})$ (i.e. $\mu(\mathbf{x}) = \delta F/\delta c(\mathbf{x})$). From the calculus of variations [7] the variation of free energy F for a variation of $c(\mathbf{x})$ is given by

$$\delta F = \int_V [\frac{\partial f}{\partial c} - \nabla \frac{\partial f}{\partial \nabla c}]\delta c dV = \int_V [\frac{\partial f^{'}}{\partial c} - 2\kappa\nabla^2 c]\delta c dV \tag{2.22}$$

which describes the change in free energy due to a local change of composition δc. Differences in local chemical potentials produce a net flux of atoms

$$J = -M\nabla \frac{\delta F}{\delta c} = -M\nabla[\frac{\partial f^{'}}{\partial c} - 2\kappa\nabla^2 c] \tag{2.23}$$

where M is a positive quantity. The kinetics of the system are obtained when the continuity equation

$$\frac{\partial c}{\partial t} = -\nabla \cdot J \tag{2.24}$$

is applied to Eq. (2.23), giving

$$\frac{\partial c}{\partial t} = \nabla \cdot M\nabla[\frac{\partial f^{'}}{\partial c} - 2\kappa\nabla^2 c]. \tag{2.25}$$

If as a first approximation M is independent of composition, we have

$$\frac{\partial c}{\partial t} = M\frac{\partial^2 f^{'}}{\partial c^2}\nabla^2 c - 2M\kappa\nabla^4 c. \tag{2.26}$$

The quantity $M\partial^2 f^{'}/\partial c^2$ is the "interdiffusion coefficient", and $2M\kappa$ accounts for the effect of incipient surfaces. Eq. (2.26) describes a diffusion process in which the free energy decreases monotonically with time. Therefore fluctuations that are necessary for nucleation events and escapes from metastable states are not allowed. The validity of this kinetic equation is restricted to the very early stages of phase separation, because only the first gradient term is included in the free energy description. At the very beginning of the process compositional fluctuations are small, and higher order gradient terms would be negligible. At later stages, however, when the amplitude of composition fluctuations increase, the higher order gradient terms become important. If the wavelength of a composition modulation is comparable to interatomic distances, the validity of first-order gradient expansion of the free energy is doubtful even at early stages of spinodal decomposition. In this case the coarse-grained composition variations approach the length scales of interatomic distances, and the gradients of the coarse-grained composition become inevitably large. Therefore the applicability of Cahn-Hilliard theory for very short wavelengths, or steep concentration gradients, breaks down.

2.3 Khachaturyan's kinetic field theory

2.3.1 Microscopic mean field equation

Khachaturyan has proposed [8,9] a diffusion equation for a microscopic (discrete) field variable, which governs the transformation kinetics at the atomic scale. The transformation kinetics of a binary alloy are described by

$$\frac{dn_i(t)}{dt} = \sum_j M_{ij} \frac{\partial F}{\partial n_j(t)}. \tag{2.27}$$

$n_i(t)$ is the probability that site i is occupied by an A-type atom, and $1 - n_i(t)$ the probability that it is occupied by a B-type atom ($0 \leq n_i(t) \leq 1$). F is the free energy of the system, and $\frac{\partial F}{\partial n_j(t)}$ is the thermodynamic driving force for the transformation. M_{ij} are probabilities for elementary diffusional jumps between lattice sites i and j. In Khachaturyan's microscopic equation it is assumed that M is constant, and inversely proportional to the time that the atom spends on a site on average. In reality this assumption fails, since the atomic mobility is known to depend on the local composition and environment.

The number of atoms in the system is fixed, i.e. $N = \sum_i n_i(t)$ and $dN/dt = 0$. Summing Eq. (2.27) over all lattice sites i gives

$$\frac{dN}{dt} = \sum_i \sum_j M_{ij} \frac{\partial F}{\partial n_j(t)} = \sum_j \left(\sum_i M_{ij} \right) \frac{\partial F}{\partial n_j(t)} = 0 \tag{2.28}$$

where M_{ij} is independent of the lattice site. Since the partial derivative part does not necessarily vanish, we must have $\sum_i M_{ij} = 0$, or $M_{ii} = -\sum_{j \neq i} M_{ij}$. Eq. (2.27) then becomes

$$\frac{dn_i(t)}{dt} = \sum_{j \neq i} M_{ij} \left(\frac{\partial F}{\partial n_j(t)} - \frac{\partial F}{\partial n_i(t)} \right) \tag{2.29}$$

which is a discrete form of the continuum Cahn-Hilliard equation [4], (2.25). The single site occupation probability n_i contains both the microscopic and macroscopic information related to the atomic structure of the ordered state, and its morphology at a given time. Therefore,

[4] See appendix B.

microscopic kinetic equation is not restricted by any prior assumptions about the forthcoming transformation path, and the intermediate transient states rise naturally from the kinetics. The major drawback of the microscopic approach is, however, its restriction to volumes which are generally too small to capture the formation and development of collective morphological patterns at mesoscopic scales. In that case continuum kinetic equation have to be used.

2.3.2 Continuum kinetic equations

The continuum field approach is appropriate at scales which well exceed the interatomic distances of the underlying crystal structure. It ignores structural details at the microscopic (atomic) level, and the properties of the material are considered as coarse grained quantities, which have a thermodynamic meaning in the sense that they are locally averaged over large numbers of atoms. In continuum kinetic field models a set of field variables is chosen to describe the state of the system and its compositional and structural development during phase transformation. The spatial evolution of the field variables is expected to be slow compared to interatomic distances. The size of the (computational) cell is chosen such that the variation of the field variables within the cell is negligible, and generally several cells are required to cover a typical wavelength of the resulting microstructure.

The field variables may be either *conserved* or *non-conserved* in character. In a closed system, which does not interact with its surroundings, composition $c(\mathbf{r}, t)$ is treated as a conserved quantity, since the number of constituent atoms remains constant. A long range order (LRO) parameter or a displacive mode are examples of non-conserved field variables. LRO is a measure for correctness of atomic positions with respect to some reference configuration, and during ordering the LRO parameter is the relevant measure of the thermodynamic state of the material. Displacive mode represents displacements of atoms from their undistorted lattice positions. Depending on the nature of the chosen field variables, their kinetic development at the continuum level can be presented in either the time-dependent Ginzburg-Landau equation (also known as Onsager, or Landau-Khalatnikov equation) for non-conserved kinetics

$$\frac{d\psi(\mathbf{r}, t)}{dt} = -\Gamma \frac{\delta F}{\delta \psi(\mathbf{r}, t)} \tag{2.30}$$

or the Cahn equation for conserved kinetics

$$\frac{dc(\mathbf{r},t)}{dt} = M\nabla^2 \frac{\delta F}{\delta c(\mathbf{r},t)}. \tag{2.31}$$

Γ is a constant characterizing the structural relaxation, and M is diffusional mobility, which is related to diffusivity by the Einstein equation $M = Dc(1-c)/k_BT$. Here c is the average composition and D diffusivity. Cahn's equation (2.31) has its origin in linear irreversible thermodynamics and the continuity equation. When writing the continuum field equations for a specific system, we have to determine the permitted structural parameter fields in advance, and this already involves assumptions about the transformation path. Therefore, there is always a possibility that we may omit some transient structural states, which are out of reach of our chosen field variables.

If the typical wavelength d of the modulated structure due to concentration inhomogeneities has dimensions much larger than the interatomic distance a, Khachaturyan's microscopic kinetic equation (2.27) shows a limit transition to continuum field equations, (2.30) and (2.31) [8]. During spinodal decomposition, this wavelength corresponds to the wave vector $2\pi/d$ in $\mathbf{k}$-space, and in the long wavelength limit the amplitudes of concentration waves show large values only close to $\mathbf{k} = 0$. Thus the wave vectors close to $\mathbf{k} = 0$ can be interpreted as a Fourier transformation of the macroscopic concentration profile $c(\mathbf{r})$. For ordering, where the superstructure is described by a characteristic wave vector $\mathbf{k}_0$, and the typical domain size of ordered regimes is $d_0 \gg a$, the reciprocal space representation of the structure exhibits peaks around $\mathbf{k} = 0$ and $\mathbf{k} = \mathbf{k}_0$, corresponding to inhomogeneities in concentration profile and LRO parameter, respectively. By neglecting all the other Fourier components generated by the structure, and focusing only on limited regions in $\mathbf{k}$-space, the characteristic functions can be expanded into Taylor series. In spinodal decomposition, the first non-vanishing term of $\tilde{M}_{\mathbf{k}}$ (the Fourier transform of mobility) around $\mathbf{k} = 0$ is quadratic, because conservation of atoms [5] makes the zeroth order term zero, and the first order term must vanish due to the invariance with respect to wave vector inversion. Substitution and back-Fourier transformation

[5] Fourier transformation of M at $\mathbf{k} = 0$ yields $\tilde{M}_{\mathbf{k}=0} = \sum_j M_{ij}$, and gives $\tilde{M}_0 = 0$.

result in the macroscopic continuum equation (2.31). A similar procedure for ordering results in its macroscopic counterpart, Eq. (2.30).

Both the continuum and microscopic field equations are deterministic. They always drive the system towards the direction which decreases the energy, but they remain in the first energy minimum, which may be a local one in the multivalley potential surface. In order to overcome this, a term corresponding to random fluctuations can be introduced to the equations [8]

$$\frac{dn_i(t)}{dt} = \sum_j M_{ij} \frac{\partial F}{\partial n_j(t)} + \xi_j(t) \tag{2.32}$$

where $\xi_j(t)$ satisfies

$$< \xi_i(t)\xi_j(t) >= -2k_B T M_{ij}\delta(t-t')\delta(i-j) \tag{2.33}$$

In principle, this also enables nucleation, where energy is needed to reach the critical nucleus size, after which the nucleus grows spontaneously.

2.3.3 On the origin of Cahn and Ginzburg-Landau equations

It has been shown by Metiu *et al.* [10–12], that by using a path-integral method both non-conserved Ginzburg-Landau and conserved Cahn equations can be derived from the same Markovian master equation

$$\tau \frac{\partial P(x,t)}{\partial t} = -\sum_\delta W(x \to x+\delta)P(x,t) + \sum_\delta W(x-\delta \to x)P(x-\delta,t) \tag{2.34}$$

where $P(x,t)$ is the probability that the chosen field variable (e.g. density profile) has value x at time t, and δ denotes a change in the field variable. This equation is general, and does not contain much physical information, unless some assumptions about the transition probability W are made. In Refs. [10–12] it was chosen as

$$W(x \to x+\delta) = \exp\left(\frac{-\delta^2}{\Delta}\right) \exp\left[-\frac{F(x+\delta)-F(x)}{2k_B T}\right]. \tag{2.35}$$

This form of transition probability assumes that at all times the system can be characterized by a free energy F, and changes which, during a time interval τ, result in an increase in the free energy are less likely than those which decrease it. The transition probabilities for the density profile follow Boltzmann statistics, and changes greater than Δ are unlikely. The master equation is formally solved to give conditional probability that the density distribution changes from its initial value $c_0(\mathbf{r})$ to some other value $c(\mathbf{r})$. This conditional probability appears as a weighted sum of all contributions from all possible paths from $c_0(\mathbf{r})$ to $c(\mathbf{r})$. The most likely transformation path will be the one whose probability is largest.

The differences between Cahn and Ginzburg-Landau equations arise from the way how correlations between changes in local field variables are treated in the expression for the transition probability. If no constraints are imposed on density changes at each spatial location, which corresponds to uncorrelated changes throughout the system, Ginzburg-Landau equation (2.30) is obtained. In this case only the magnitude and direction of changes matter, but not the way how the changes occur in the system. If conservation constraints are imposed, i.e. increase in order parameter in one area is followed by decrease in neighbouring regions, Cahn's equation (2.31) is achieved.

Assuming correlated changes, the general continuum Metiu-Kitahara-Ross (MKR) equation reads as

$$\frac{d\psi(\mathbf{r},t)}{dt} = -\alpha\left[1 - \exp\left(-\frac{\xi^2}{2}\nabla^2\right)\right]\frac{\delta F}{\delta\psi(\mathbf{r},t)}. \tag{2.36}$$

ξ characterizes the typical length scale of conservation, over which changes in order parameter ψ are compensated in surrounding areas. If the variation of $\psi(\mathbf{r},t)$ within the length scale ξ is small, the exponential term can be expanded, and the lowest order term gives

$$\frac{d\psi}{dt} = \frac{\alpha\xi^2}{2}\nabla^2\frac{\delta F}{\delta\psi} \tag{2.37}$$

which is equivalent to the Cahn-Hilliard equation. On the other hand, if ξ is very large compared

to the length scales over which ψ varies, the spatial derivatives can be neglected, and we obtain

$$\frac{d\psi}{dt} = -\alpha \frac{\delta F}{\delta \psi}, \tag{2.38}$$

which has the Ginzburg-Landau form. In derivation of Eq. (2.36) it is assumed that correlations between different sites decrease rapidly and isotropically with increasing distance. Hence - rather arbitrarily though - the correlation function is assumed to have a Gaussian shape, and in case it has some other form, the resulting kinetic equation will differ from Eq. (2.36).

2.4 Salje rate law

Salje considered the question of whether it is reasonable to characterize order parameters as either conserved or non-conserved quantities. These are limiting extremes with obvious physical representations, but why could not there be cases, where partial conservation occurs, or conservation occurs within a certain distance (compared to the correlation length) within the sample? Salje proposed a kinetic rate law interpolating between conserved and non-conserved kinetics. His rate law has its roots in the continuum Metiu-Kitahara-Ross equation (2.36), which he interpolated in the form [13, 14]

$$\frac{d\psi(\mathbf{r},t)}{dt} = -\alpha \left[1 - \frac{{\xi_c}^2}{\xi^2} \exp\left(-\frac{\xi^2}{2} \nabla^2 \right) \right] \frac{\delta F}{\delta \psi(\mathbf{r},t)}. \tag{2.39}$$

Compared to equations used by Khachaturyan, the time derivative of ψ in Eq. (2.39) is not generally linearly dependent on the driving force, but it is related to it *through an operator*. ψ is a continuous order parameter (field variable), which restricts the applicability of Eq. (2.39) to mesoscopic and macroscopic scales. ξ and ξ_c are length scales for correlation and conservation, respectively, and α is a material dependent mobility parameter, which has the form $\alpha \propto \lambda \exp(-\Delta E_a / k_B T)$. E_a is the mean activation or saddle point energy, and λ represents the "attempt frequency" for a jump. To a first approximation E_a may be considered a constant, and independent of the order parameter. In mesoscopic scales, ψ is a quantity averaged over

a large number of atoms, and describes, for example, composition or lattice distortions. At macroscopic scales, ψ is the average of local mesoscopic values of order parameter throughout the whole crystal, and it can be for example the average displacement of atoms from their equilibrium positions. The time-development of (discrete) order parameter in microscopic scale, such as the number of (in)correct bonds around a given site, is beyond the applicability of the Salje rate law.

The ratio of the length scales ξ_c and ξ, called the mixing coefficient between the kinetics, sets the "degree of conservation" for the Salje rate equation. ξ is the correlation length of ψ, which is a measure for the distance over which a change in the value ψ in one area of the crystal causes correlated changes in other areas. ξ_c is the length scale of conservation, the meaning of which is best illustrated by examples.

In spinodal decomposition, an increase in one constituent component at a specific point is compensated exactly by a decrease of that same component in surrounding areas. In this case the length scale of conservation corresponds to the typical wavelength of the composition modulation. In an ordering process, however, there are no compositional changes, but exchanges occur only between neighbouring sites. In this case ξ_c is comparable to an interatomic distance. If in displacive transitions displacement of one atom is not accompanied by any compensatory movements in its neighbourhood, $\xi_c = 0$. If the conservation length is the same as the length of correlation, we get from Eq. (2.39), after expansion of the exponential and keeping the lowest order term,

$$\frac{d\psi(\mathbf{r},t)}{dt} = \frac{\alpha}{2}{\xi_c}^2\nabla^2\frac{\delta F}{\delta\psi(\mathbf{r},t)}, \tag{2.40}$$

which has the form of Cahn's equation. On the other hand, if the correlation length is large compared to the length of conservation, equation Eq. (2.39) is cast to the Ginzburg-Landau form:

$$\frac{d\psi(\mathbf{r},t)}{dt} = -\alpha\frac{\delta F}{\delta\psi(\mathbf{r},t)}. \tag{2.41}$$

The ratio ξ_c/ξ is usually close to one or zero. Generally, not much is known about cases where

$0 < \xi_c/\xi < 1$. This could be a process where ordering is followed by mass transport from the surroundings. This intermediate region has so far been only of theoretical curiosity, and serves as a possible bridge between conserved and non-conserved kinetics.

Interestingly, a rate law very similar to Eq. (2.39) has also been derived from the stochastic processes in a kinetic Ising model. Dattagupta *et al.* [15, 16] assumed competing kinetics between conserved Kawasaki and non-conserved Glauber dynamics, and considered a combined equation like

$$\frac{d\psi}{dt} = \left(\frac{d\psi}{dt}\right)_{Glauber} + \left(\frac{d\psi}{dt}\right)_{Kawasaki}. \tag{2.42}$$

For nearly uniform systems [6] not far from equilibrium [15] Eq. (2.42) coincides with the Salje rate law. For non-uniform systems [16], however, the resulting kinetic equation has a complex structure, which is not transparent to simple physical interpretations.

2.5 Martin-Vaks mean field equation

Khachaturyan's microscopic mean field equation (2.27) does not take into account the fact that in reality the atomic mobility depends on the local composition. Martin introduced a simple stochastic model, which includes an expression for the environment dependent atomic mobility [17]. Later a non-linear direct-exchange mean field kinetic equation for a concentration field was established more rigorously [18, 19].

The time evolution of the mean occupation number n_i is described as a mean field master equation for a direct atomic exchange:

$$\begin{aligned}\frac{dn_i}{dt} = \sum_j \nu[&n_j(1-n_i)\exp(-\frac{E^s - E_i^B}{k_BT})\exp(-\frac{E^s - E_j^A}{k_BT}) \\ &- n_i(1-n_j)\exp(-\frac{E^s - E_j^B}{k_BT})\exp(-\frac{E^s - E_i^A}{k_BT})]\end{aligned} \tag{2.43}$$

[6] Uniformity = the value of the order parameter is independent of the (lattice) site.

or, if the saddle point energy E^s is assumed to be independent of the environment,

$$\frac{dn_i}{dt} = \sum_j \gamma_{ij}[n_j(1-n_i)\exp(\frac{E_i^B}{k_BT})\exp(\frac{E_j^A}{k_BT}) - n_i(1-n_j)\exp(\frac{E_j^B}{k_BT})\exp(\frac{E_i^A}{k_BT})]. \tag{2.44}$$

$\gamma_{ij} = \nu\exp(-2E^s/k_BT)$ is the composition independent part, where ν is the attempt frequency. The first term in Eq. (2.44) describes jumps of A atoms in to site i, and the second one out of it to site j. The activation energy for an A jump from site i is $E^s - E_i^A$, where E^s is a constant, and E_i^A is the mean field potential acting on atom A at i. It is the energy required to cut the bonds between A and its neighbours in order to allow it to jump.

The similarities and differences between Martin-Vaks mean field equation (2.44) and Khachaturyan microscopic kinetic equation (2.27) become transparent, if we employ the mean field master equation further. The time evolution of the site-occupation probability (say for A atoms) n_i is written as

$$\frac{dn_i}{dt} = \sum_{j\neq i} J_j \tag{2.45}$$

$$J_j = n_j(1-n_i)\Gamma_{ji} - n_i(1-n_j)\Gamma_{ij} \tag{2.46}$$

The first term describes the flux of A atoms from site j to site i, and the second term from site i to j. At the same time there is a compensating flux of B atoms in the opposite direction. Γ_{ji} and Γ_{ij} are jump frequencies. Eq. (2.46) can be written in a more useful way by calling the first term b (backward jumps) and the second f (forward jumps)[7]:

$$J_j = b - f = \sqrt{bf}(\sqrt{\frac{b}{f}} - \sqrt{\frac{f}{b}}) \tag{2.47}$$

[7] The directions "backward" and "forward" refer to the motion of A atoms along the $i-j$ bond.

where

$$\sqrt{bf} = (n_i n_j (1-n_i)(1-n_j)\Gamma_{ij}\Gamma_{ji})^{1/2} \tag{2.48}$$

$$\sqrt{\frac{b}{f}} = (\frac{n_j(1-n_i)\Gamma_{ji}}{n_i(1-n_j)\Gamma_{ij}})^{1/2} \tag{2.49}$$

$$\sqrt{\frac{f}{b}} = (\frac{n_i(1-n_j)\Gamma_{ij}}{n_j(1-n_i)\Gamma_{ji}})^{1/2} \tag{2.50}$$

Assuming that the attempt frequency ν is independent of the type of atom, the jump frequencies are written as follows:

$$\Gamma_{ij} = \nu \exp(-\frac{E_s^A - E_i^A}{k_B T}) \exp(-\frac{E_s^B - E_j^B}{k_B T}) \tag{2.51}$$

$$\Gamma_{ji} = \nu \exp(-\frac{E_s^B - E_i^B}{k_B T}) \exp(-\frac{E_s^A - E_j^A}{k_B T}) \tag{2.52}$$

E_s^A (E_s^B) being the saddle point energy for atom $A(B)$ and E_i^A (E_i^B) the energy of $A(B)$ atom at site i. Now we can write Eq. (2.49) as

$$\begin{aligned}\sqrt{\frac{b}{f}} &= (\frac{n_j}{1-n_j})^{1/2}(\frac{n_i}{1-n_i})^{-1/2} \exp\Big\{\frac{-(E_i^A - E_i^B) - (E_j^B - E_j^A)}{2k_B T}\Big\} \\ &= \exp\Big\{-\frac{1}{2k_B T}\Big[(E_i^A - E_i^B + k_B T \ln\frac{n_i}{1-n_i}) - (E_j^A - E_j^B + k_B T \ln\frac{n_j}{1-n_j})\Big]\Big\}\end{aligned} \tag{2.53}$$

The energy of an A atom at site i is given in the mean field approximation by $E_i^A = \sum_{k\neq i} n_k \epsilon_{AA} + (1-n_k)\epsilon_{AB}$ and similarly, $E_i^B = \sum_{k\neq i}(1-n_k)\epsilon_{BB} + n_k\epsilon_{AB}$. $E_i^A - E_i^B$ thus becomes

$$\begin{aligned}E_i^A - E_i^B &= \sum_{k\neq i}[(\epsilon_{AA} + \epsilon_{BB} - 2\epsilon_{AB})n_k + \epsilon_{AB} - \epsilon_{BB}] \\ &= \sum_{k\neq i}[V_{ik} n_k + \epsilon_{AB} - \epsilon_{BB}] = \frac{\partial U}{\partial n_i}\end{aligned} \tag{2.54}$$

where U is the internal energy of the system, and V_{ik} the atomic interaction parameter. The terms in the exponential of Eq. (2.53) are the "local chemical potentials", $\partial F/\partial n_i$ and $\partial F/\partial n_j$, at sites i and j respectively, and Eq. (2.53) can be written as

$$\sqrt{\frac{b}{f}} = \exp\Big\{\frac{1}{2k_B T}(\frac{\partial F}{\partial n_j} - \frac{\partial F}{\partial n_i})\Big\} \tag{2.55}$$

and Eq. (2.47) as

$$\begin{aligned} J_j &= \sqrt{bf}\left[\exp\left\{\frac{1}{2k_BT}(\frac{\partial F}{\partial n_j}-\frac{\partial F}{\partial n_i})\right\}-\exp\left\{\frac{1}{2k_BT}(\frac{\partial F}{\partial n_i}-\frac{\partial F}{\partial n_j})\right\}\right] \\ &= 2M_{ij}\sinh\left\{\frac{1}{2k_BT}(\frac{\partial F}{\partial n_j}-\frac{\partial F}{\partial n_i})\right\}. \end{aligned} \tag{2.56}$$

$M=\sqrt{bf}$ is identified as the mobility which is clearly environment dependent:

$$M_{ij}=\nu\sqrt{n_in_j(1-n_i)(1-n_j)}\exp(-\frac{2E_s^A-E_i^A-E_j^A}{2k_BT})\exp(-\frac{2E_s^B-E_i^B-E_j^B}{2k_BT}). \tag{2.57}$$

The choice of the saddle point energy E_s in Eq. (2.57) fixes the exact form of the mobility.

Close to equilibrium, where driving forces are small, the Martin-Vaks mean field equation reduces to a form similar to the Khachaturyan microscopic diffusion equation (2.27):

$$\frac{dn_i}{dt}=\sum_{j\neq i}\frac{M_{ij}}{k_BT}\left\{\frac{\partial F}{\partial n_j}-\frac{\partial F}{\partial n_i}\right\}. \tag{2.58}$$

However, in contrast to the Khachaturyan form, the mobility in Eq. (2.58) is environment dependent through Eq. (2.57), in which M_{ij} is predicted to be a maximum when $n_i=n_j=1/2$ and tend to zero as n_i or $n_j\to 0$ or 1.

2.6 Microscopic cluster activation method

The Salje rate law, the Martin-Vaks mean field equation, and kinetic field equations used by Khachaturyan are all based on the formulation of the appropriate free energy functional, which depends on the inhomogeneous distribution of field variables. If the rate of change of the field variable is linearly dependent on the thermodynamic driving force, or the proportionality constants are assumed to be independent of local field variables, as is the case in kinetic field theory, the description of kinetics becomes invalid very far from equilibrium and quantitative rates of change are inaccurate.

Chen and coworkers [20–23] applied a microscopic kinetic model, which utilizes cluster correlation functions and microscopic master equation for diffusion, and no free energy functionals

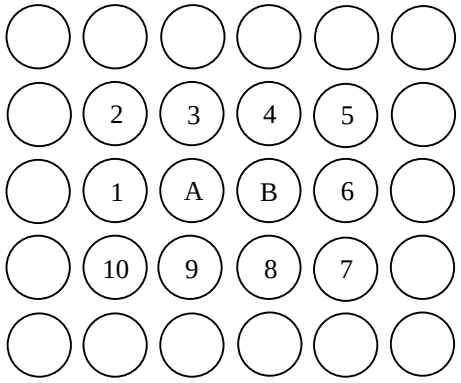


Figure 2.2: Schematic picture showing the interchanging $A-B$ pair, and the set of neighbours affecting the energetics of the exchange.

are explicitly utilized in kinetic equations. In this model a pair of interchange sites at $\mathbf{r}$ and a next nearest neighbour site $\mathbf{r}+\delta$ are considered. A set of nearby sites affect the interchange probability [24]. For example, in Fig. 2.2, the swop of the $A-B$ pair is affected by the surrounding nearest neighbour and next nearest neighbour atoms, numbered from 1 to 10.

The rate at which the $A-B$ pair will swap within an environment of atoms of types $\mathbf{X}$ at sites $\mathbf{x}$ is denoted by $R_{AB}(\mathbf{X})$. The rate of change of probability of finding an A atom at site $\mathbf{r}$, $P_A(\mathbf{r})$, is

$$\frac{dP_A(\mathbf{r})}{dt} = \sum_{\delta}\Big[\sum_{\mathbf{X}} P_{BA\mathbf{X}}(\mathbf{r},\mathbf{r}+\delta,\mathbf{x})R_{BA}(\mathbf{X}) - \sum_{\mathbf{X}} P_{AB\mathbf{X}}(\mathbf{r},\mathbf{r}+\delta,\mathbf{x})R_{AB}(\mathbf{X})\Big] \tag{2.59}$$

where the first term describes A atoms arriving at site $\mathbf{r}$, and the second one A atoms leaving the site. In order to carry out the sum in the right-hand side, we need to approximate the joint distribution function $P_{BA\mathbf{X}}(\mathbf{r},\mathbf{r}+\delta,\mathbf{x})$. If statistical independence among occupation probabilities is assumed, as in the mean field approximation, we have

$$P_{BA\mathbf{X}}(\mathbf{r},\mathbf{r}+\delta,\mathbf{x}) = P_A(\mathbf{r})P_B(\mathbf{r}+\delta)P_{X_1}(\mathbf{x}_1)P_{X_2}(\mathbf{x}_2)...P_{X_n}(\mathbf{x}_n) \tag{2.60}$$

The activation energy associated with the interchanging pair is represented as the sum of contributions from neighbouring atoms of the pair. If we have interactions up to the second

nearest neighbours, as in Fig. 2.2, we have

$$R_{AB}(\mathbf{X}) = \nu \exp\left(-\sum_{i=1}^{10} \frac{U(AB, X_i)}{k_B T}\right) \tag{2.61}$$

$$R_{BA}(\mathbf{X}) = \nu \exp\left(-\sum_{i=1}^{10} \frac{U(BA, X_i)}{k_B T}\right) \tag{2.62}$$

where ν is the attempt frequency for the $A-B$ exchange, and $U(AB, X_i)$ is the contribution to the activation energy from site i occupied by atom X. Two different contributions can be separated from $U(AB, X_i)$. If, for example, we have an A atom at site 1 in Fig. 2.2, we obtain

$$U(AB, A_1) = \epsilon^1_{AA} + \epsilon^*_{AB} \tag{2.63}$$

where ϵ^1_{AA} is the energy for a first nearest neighbour $A-A$ bond, and ϵ^*_{AB} is the contribution to the total energy of the $A-B$ pair at the activated position. No explicit free energy functional is needed, since the dependency of atomic diffusion on local configuration is taken into account in evaluating the activation energy. The microscopic cluster activation method is valid in describing states, which are far from the equilibrium. It has been applied to systems undergoing ordering and spinodal decomposition [20–23].

2.7 Discussion

Generally speaking, mean field kinetic equations are of greatest use in describing spinodal decomposition or ordering in alloys. Since they are deterministic in character, and most are based on direct minimization of free energy, they are not naturally capable of describing processes like nucleation and growth, where fluctuations play an essential role in overcoming the free energy barrier. Microscopic kinetic equations, like Khachaturyan's microscopic diffusion equation, and the Martin-Vaks mean field equation, are applicable at the atomic level, and the only order parameter required is the single site occupation probability. However, when the length scale of the microstructure increases, these approaches are not applicable, and continuum field methods are needed. Then the formulation of the appropriate free energy functional plays a crucial role, since the choice of order parameters involves assumptions of the structural stages

arising during phase transformation. The formulation of the mean field free energy functional is discussed more detail in the next chapter.

Many kinetic equations, such as Khachaturyan's microscopic diffusion equation, Martin-Vaks mean field equation and cluster activation method, can, without any major difficulties, be extended to multicomponent alloys, which also include vacancies. Although in real metallic alloys diffusion occurs through vacancy motion, this extension does not necessarily bring in much more physics if the diffusion mechanism remains undefined. This is the case in Khachaturyan's microscopic equation.

The lack of a well defined diffusion mechanism in Khachaturyan's microscopic field equation does not allow a proper physical definition of the time scale in the model. Time scale arises from the mobility M, which is an environment independent coefficient, and cannot be related to any atomistic diffusion processes in the system. Therefore it is impossible to relate times to transformation stages, although the sequence of microstructural stages during the transformation may be unaffected. The Martin-Vaks kinetic mean field equation takes into account the environment dependence of the mobility, but when the diffusion mechanism relies on direct atomic exchanges rather than realistic vacancy hopping, the problem of defining a physical time scale remains.

Interestingly, many kinetic equations have been found to have common interfaces, or be equivalent under certain circumstances. It has been shown that the conserved Cahn-Hilliard and non-conserved Ginzburg-Landau can be derived from the same master equation, and Salje proposed an interpolating rate equation mixing both kinetics. Khachaturyan's diffusion equation is a microscopic counterpart of continuum Cahn-Hilliard equation, and shows a long wavelength limit transition to both conserved and non-conserved continuum equations. If driving forces for transformation are small, Khachaturyan microscopic diffusion equation and Martin-Vaks mean field equations have the same form. If, however, the driving forces are large, Martin-Vaks equation is non-linear with respect to the driving force, and is claimed to be more accurate.

Chapter 3

Driving force for transformation

3.1 Introduction

So far not much has been said about the specific form of the driving force appearing in kinetic equations in chapter 2. It is assumed that there exists a free energy functional describing both equilibrium and non-equilibrium states of the system. Although strictly speaking, free energy is a valid and well-defined concept only at equilibrium, mean field kinetic equations are nevertheless based on the assumption that for a system undergoing phase transformation an expression for "excess" free energy can be written. Generally, construction of a free energy functional from first principles and microscopic atomic theories is complicated. It is claimed, however, that for a mean field model to produce the correct transformation sequence of microstructures only the essential features of the exact free energy functional are required [8]. Therefore, one has to be able to express the free energy as a function of the chosen field variables, normally composition or some structural order parameter(s).

Condensed systems may exhibit a variety of spatial order, which cannot be described uniquely by volume, number of particles or internal energy, but description of ordered phases requires introduction of new variables quantifying the degree of local or global order. An order parameter representation is a standard approach in describing the state of a system, when mean field theories are applied in constructing the free energy functional. The order parameter is a local (i.e. site dependent), or global (i.e. spatially uniform) parameter that distinguishes

an ordered phase from a disordered one. It has different values in different phases reflecting the symmetry of the underlying Hamiltonian that describes the energetics of the system.

In this chapter I will discuss the formulation of the free energy functional using two mean field theories, which have been extensively used in studies of phase transformations: the Bragg-Williams theory and the Landau theory. For many alloys of practical importance, the chemical free energy is insufficient to describe the energetics of the phase transformation, because elastic interactions between phases of different lattice constants have to be taken into account. In (rare) cases, where particle-matrix interfaces remain coherent and all phases have the same elastic moduli, the elastic energy can be conveniently incorporated into the mean field description of the driving force. Implementation of the Khachaturyan microscopic mean field equation in reciprocal space and some computational aspects are also discussed.

3.2 Bragg-Williams theory

Bragg-Williams theory was developed in the '30s for an Ising ferromagnet. It is an approximation to the free energy, in which configurational entropy is calculated exactly for an ideal, i.e. non-interacting, mixture of components, and in which the internal energy is approximated by replacing local, fluctuating order parameters, by their average values.

Consider first the case in which the order parameter is spatially uniform throughout the system. This is a useful approach in understanding basic ideas and approximations behind mean field theories, and it can be later applied to set up the basis for Landau theory. The uniform order parameter formalism can also be extended to a case in which the order parameter varies spatially [25]. This is a more useful description for alloys undergoing phase transformations, since in microscopic mean field kinetic equations, such as Khachaturyan and Martin-Vaks equations, (2.27) and (2.44), local order parameters are the occupation probabilities of atomic lattice sites.

As a simple but illustrative example we employ an Ising model representation of a ferromagnetic system. The uniform order parameter is the total magnetic moment, which is the

average of the spin occupations:

$$m = \frac{N_+ - N_-}{N}. \tag{3.1}$$

$N = N_+ + N_-$ is the total numbers of lattice sites, and N_+ and N_- are the number of "up" and "down" spins. The order parameter is zero at high temperatures, when the spins are randomly oriented, and non-zero below the critical ordering temperature T_c.

Entropy is a measure of the degree of disorder in the system. Configurational entropy arises from the different distinguishable ways in which spins can be arranged, and for a system with spatially uniform magnetization m it can be calculated exactly. It is therefore assumed that all configurations with fixed N_+ and N_- are equally probable, and the number of ways of arranging spins on lattice sites is

$$\Omega = \binom{N}{N_+} = \binom{N}{N(1+m)/2} = \left(\frac{N!}{(N(1+m)/2)!(N(1-m)/2)!}\right) \tag{3.2}$$

Configurational entropy is proportional to the logarithm of the number of possible configurations Ω:

$$S = k_B \ln \Omega \tag{3.3}$$

and, if expressed as entropy per spin, becomes [1]

$$s(m) = \frac{S}{N} \approx k_B[\ln 2 - \frac{1}{2}(1+m)\ln(1+m) - \frac{1}{2}(1-m)\ln(1-m)] \tag{3.4}$$

In order to evaluate the internal energy U in the Helmholtz free energy $F = U - TS$, spins at each atomic sites are replaced by their position independent average m. The exact evaluation of internal energy U would require calculation of $\langle H \rangle = \mathrm{Tr}_m H \exp(-\beta H)/Z_m$, where Tr_m is a trace (i.e. sum or integral) over all configurations with fixed m, $\beta = \frac{1}{k_B T}$, and $Z_m = \mathrm{Tr}_m \exp(-\beta H)$. This would give the exact solution of the Ising model, and is considered a task to be avoided due

[1] Stirling's formula $\ln X! = X \ln X - X$ (for large X) is used to approximate the logarithmic term.

to its complexity. In the Bragg-Williams approximation the internal energy is approximated as

$$U = -J \sum_{<i,j>} m^2 = -\frac{1}{2} JNzm^2 \tag{3.5}$$

where z is the number of nearest neighbour lattice sites, J is the interaction parameter between spins, and the sum goes over nearest neighbour bonds. The complete Bragg-Williams free energy per site is

$$f(T,m) = \frac{(U - TS)}{N} = -\frac{1}{2} Jzm^2 + \frac{1}{2} k_B T[(1+m)\ln(1+m) + (1-m)\ln(1-m)] - k_B T \ln 2 \tag{3.6}$$

This function is plotted [2] in Fig. 3.1 at various temperatures T. At high temperatures, f has a single minimum at $m = 0$, which corresponds to a disordered state. As temperature decreases the function shows two minima, and as $T \to 0$ these minima shift closer to unity.

The Bragg-Williams theory for a uniform order parameter can be generalized to spatially non-uniform order parameters [25]. The spatially non-uniform formulation of the Bragg-Williams theory is used in describing alloys undergoing phase transformations, where spatial variation of order parameter(s) generates microstructures. Now the local order parameter is $n_i =< p_i >$, where [3] n_i is the occupation probability of lattice site i: $p_i = 1$, if site i is occupied by an A atom, and $p_i = 0$, if it is occupied by a B atom.

In solid solutions, there are two contributions to the entropy: thermal and configurational [1]. Thermal entropy describes different ways how thermal energy can be divided amongst the atoms forming the solid solution. If no volume or heat change occur during mixing of A and B components of the alloy, there is no contribution of thermal entropy to the free energy. In Bragg-Williams treatment the effect of thermal entropy is not included. For configurational

[2] Note that in Fig. 3.1 Eq. (3.6) is scaled by the mean field critical temperature $k_B T_c = zJ$, and shifted by $\ln 2$ to always have $f = 0$ at $m = 0$.

[3] Here we assume a binary alloy.

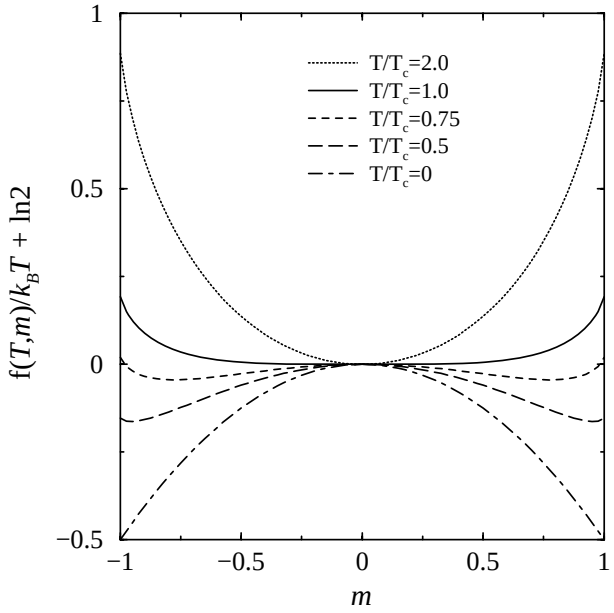


Figure 3.1: The Bragg-Williams free energy of Eq. (3.6) at different temperatures T/T_c. At $T = T_c$ there is a single, very broad minimum at magnetization $m = 0$. For $T > T_c$ the single minimum is more clear, and for $T < T_c$ two minima occur symmetrically at $\pm m$ with the same free energy. At $T = 0$, these two minima occur at $m = \pm 1$.

entropy, the number of ways how N_A solute atoms can be arranged in N lattice sites is

$$\Omega = \binom{N}{N_A} = \binom{N}{cN} \tag{3.7}$$

where $c = N_A/N$ is the solute concentration. Configurational entropy per atomic site now becomes

$$s = \frac{1}{N} k_B \ln \frac{N!}{(cN)!(N - cN)!} \approx -k_B[c \ln c + (1 - c) \ln(1 - c)]. \tag{3.8}$$

For a spatially non-uniform system, however, it is assumed that entropy is a sum of "local" entropies [25]:

$$S = -k_B \sum_i [n_i \ln n_i + (1 - n_i) \ln(1 - n_i)]. \tag{3.9}$$

This ensures that entropy increases, as non-uniform microstructures are generated. The internal

energy of a binary alloy is

$$U = \frac{1}{2}\sum_{i,j} n_i n_j \epsilon_{ij}^{AA} + [n_i(1-n_j) + n_j(1-n_i)]\epsilon_{ij}^{AB} + (1-n_i)(1-n_j)\epsilon_{ij}^{BB} \tag{3.10}$$

where ϵ_{ij}^{XY} are bond energies between X and Y atoms at sites i and j. After rearranging terms in Eq. (3.10) the generalized Bragg-Williams mean field free energy becomes [4]

$$F = \frac{1}{2}\sum_{i,j} V_{ij} n_i n_j + Q_{ij}(n_i + n_j) + \epsilon_{ij}^{BB} + k_B T \sum_i [n_i \ln n_i + (1-n_i)\ln(1-n_i)] \tag{3.11}$$

where $V_{ij} = \epsilon_{ij}^{AA} + \epsilon_{ij}^{BB} - 2\epsilon_{ij}^{AB}$ is the usual interaction parameter in quasichemical theory and $Q_{ij} = \epsilon_{ij}^{AB} - \epsilon_{ij}^{BB}$ is the asymmetry parameter [5]. The Bragg-Williams free energy is used in Khachaturyan's microscopic mean field equation (2.27), and in the Martin-Vaks equation (2.44). It has to be recalled here that configurational entropy is not exact, since atomic interactions introduce correlations between site occupancies, and the assumption of non-interacting components in violated.

3.3 Landau theory

Landau theory is a phenomenological form of mean field theory. It expresses free energy in terms of local free energy density $f(T, \psi(\mathbf{x}))$, which is a function of the local order parameter $\psi(\mathbf{x})$ at $\mathbf{x}$ only, and a part that produces an increase in free energy due to deviations from spatial uniformity. The simplest form of free energy is therefore

$$F = \int_V f(T, \psi(\mathbf{x})) + \frac{1}{2}[\nabla\psi(\mathbf{x})]^2 dV. \tag{3.12}$$

[4] Note the difference in formulations for entropies in Eqs. (3.4) and (3.8). In our binary alloy example for the non-uniform system the order parameter n_i varies between 0 and 1, but in the uniform Ising model it has values between -1 and 1. The binary alloy system can be formulated without any difficulty in the "spin language" as well, and this would not change the main lines of reasoning in any way.

[5] Note that the second term in Eq. (3.11) is constant, if the number of atoms of each type in the system is fixed, and therefore this term does not affect the transformation process. Later the reciprocal space formulation for the driving force, Eq. (3.32), also shows that in Khachaturyan's microscopic mean field equation this asymmetry parameter has no role.

For $T > T_c$ the local order parameter $\psi(\mathbf{x})$ is zero. In the vicinity of the critical temperature T_c, where ψ is small the local free energy density f is approximated by a power series in ψ:

$$f(T,\psi) = a + \frac{1}{2}b\psi^2 + \frac{1}{4}c\psi^4 + ... \tag{3.13}$$

where coefficients $a, b, c, ...$ are temperature dependent, and can be derived from first principles simulations or experimental data. The series of Eq. (3.13) seldom contains odd powers of ψ, since the expansion must be invariant under the symmetry group of the disordered phase. The Ising Hamiltonian $H = \sum J_{ij}\sigma_i\sigma_j$, for example, is invariant under spin inversion, $\sigma_i \to -\sigma_i$, and the free energy is a function of $m^2 = \sigma^2$, as seen in the Bragg-Williams representation of the free energy, Eq. (3.6).

If the Bragg-Williams free energy, Eq. (3.6), is expanded in powers [6] of m, we obtain

$$\begin{aligned} f &= -\frac{1}{2}Jzm^2 - k_BT(\ln 2 - \frac{1}{2}m^2 - \frac{1}{12}m^4 + ...) \\ &= -k_BT\ln 2 + \frac{1}{2}k_B(T - T_c)m^2 + \frac{1}{12}k_BTm^4 + ... \end{aligned} \tag{3.14}$$

where $k_BT_c = zJ$ is the critical temperature [7]. It can be seen that the Landau free energy expansion, Eq. (3.13), has the same form as the free energy per site of Bragg-Williams theory. This is the main physical motivation for the power series expansion of the local free energy density $f(T,\psi)$.

A common interface between Landau and Bragg-Williams free energies can also be achieved by taking a long wavelength limit of Bragg-Williams free energy for a non-uniform alloy, Eq. (3.11). After a Fourier transform [8] of the first term (and neglecting the constant terms), which is the internal energy, Eq. (3.11) reads as

$$F = \frac{1}{2}\sum_{\mathbf{k}} \tilde{V}_{\mathbf{k}}|\tilde{n}_{\mathbf{k}}|^2 + k_BT\sum_i n_i\ln n_i + (1-n_i)\ln(1-n_i). \tag{3.15}$$

Taking the Taylor expansion of $\tilde{V}_{\mathbf{k}}$ around $\mathbf{k} = 0$, and keeping only the first non-vanishing

[6] $\ln x = (x-1) - \frac{1}{2}(x-1)^2 - \frac{1}{3}(x-1)^3 - ....$

[7] Mean field critical temperature and phase diagram with miscibility gap are discussed in appendix A.

[8] A Fourier transform of a function is defined as $\tilde{f}_{\mathbf{k}} = \sum_{\mathbf{r}} f_{\mathbf{r}} e^{-i\mathbf{kr}}$.

term, we have

$$F = \frac{1}{2}\sum_{\mathbf{k}}(\tilde{V}_{\mathbf{k}=0} + \alpha k^2)|\tilde{n}_{\mathbf{k}}|^2 + k_B T \sum_i n_i \ln n_i + (1-n_i)\ln(1-n_i) \tag{3.16}$$

and a back Fourier transform gives

$$F = \frac{1}{2}\sum_{i}\tilde{V}_{\mathbf{k}=0} n_i^2 + k_B T \sum_i n_i \ln n_i + (1-n_i)\ln(1-n_i) + \alpha(\nabla n)^2. \tag{3.17}$$

By denoting $f(n_i) = \tilde{V}_{\mathbf{k}=0} n_i^2 + k_B T[n_i \ln n_i + (1-n_i)\ln(1-n_i)]$, changing to a continuous order parameter presentation $\psi(\mathbf{r})$, and replacing the sum by integration, we get a Landau-type free energy, which is used in continuum field equations, (2.30) and (2.31):

$$F = \int f(\psi(\mathbf{r})) + \alpha(\nabla\psi(\mathbf{r}))^2 dV. \tag{3.18}$$

By including more terms in Taylor expansion in Eq. (3.16) we will end up with higher powers of the gradient term:

$$F = \int f(\psi(\mathbf{r})) + A(\nabla\psi(\mathbf{r}))^2 + B(\nabla\psi(\mathbf{r}))^4 + ...dV \tag{3.19}$$

Gradient terms describe the energy increase due to inhomogeneities, whereas the polynomial terms determine the basic thermodynamic bulk properties of the material. If the logarithmic term in Eq. (3.16) is approximated as power series, as in Eq. (3.14), powers in the local free energy term are obtained. Several examples of formulating Landau free energy functionals for physical systems with both conserved and non-conserved order parameters are given in Refs. [8, 26].

3.4 Elastic energy

Compositional variations are not always adequate to characterize and explain the variety of phenomena observed during microstructural evolution, because infinite range, strain induced interactions between coherent new-phase inclusions are known to have a profound effect on

the transformation path. When sizes of constituent atoms differ considerably from each other, distortions due to lattice mismatch influence the kinetics and morphological development of the alloy. Since each particle generates an anisotropic strain field around it, particles prefer to locate themselves so that their strain fields cancel out, and the total strain energy decreases considerably. As a result, different particle shapes and mesoscale patterns are produced by transformation induced elastic strains, a description of which should be included in any proper theory.

There are some significant differences between conventional chemical free energy and transformation induced strain energy [27]. In contrast to conventional Gibbsian thermodynamics, the total strain energy cannot be presented as a sum of energies per unit volume, i.e. it is not an extensive thermodynamic property. This is due to the infinite range nature of strain interactions. Strain energy is not additive, either, i.e. the free energy of a multiphase mixture cannot be expressed as a sum of free energies of constituent phases irrespective of the compositions and volumes of the others. This is because the lattice misfit along interfaces depends on the compositions of phases on both side of the coherent boundary, which makes strain energy dependent also on the composition of the host matrix. These features together with the infinite ranged character of strain induced interactions make theoretical analysis of the time-evolution of pattern morphologies complicated. Knowledge of the strain energy functional, however, is an essential component for modelling many phase transformations of immense practical importance. The question has been addressed since the 40's in numerous publications [9, 27–37].

Khachaturyan has developed an analytical theory for the case, in which the transformation process generates coherent new phase particles, and *differences in elastic moduli can be neglected* [9]. In this case, an expression for the strain energy of an arbitrary structural pattern as a sum of pair-wise interactions between the constituent phases can be formulated in reciprocal space in closed form. The elastic displacement field generated by distorting solute atoms is worked out in detail in Ref. [9] using microscopic elasticity, which takes into account the discrete nature of the crystal lattice. In this case the elastic energy of a binary substitutional solution is

$$E_{el} = \frac{1}{2N} \sum_{\mathbf{k}} \tilde{B}_{\mathbf{k}} |\tilde{n}_{\mathbf{k}}(t)|^2 \tag{3.20}$$

where

$$\tilde{B}_{\mathbf{k}} = v_0 \lambda_{ijkl} \epsilon^0_{ij} \epsilon^0_{kl} - \tilde{F}_{(i)\mathbf{k}} \tilde{G}_{(ij)\mathbf{k}} \tilde{F}^*_{(j)\mathbf{k}} \tag{3.21}$$

is the "elastic potential", which includes all the information of the elastic properties of the system. The first term in Eq. (3.21) describes the configuration independent contribution to the elastic energy, which is not affected by spatial redistribution of solute atoms. The second term gives the elastic energy related to spatial redistribution of solute in the alloy. In Eq. (3.21) λ_{ijkl} the elastic moduli tensor, $\epsilon^0_{ij} = \frac{da}{ad\bar{c}}\delta_{ij}$ a tensor of the expansion coefficient of the crystal lattice (a is the lattice parameter), $\sigma^0_{ij} = \lambda_{ijkl}\epsilon^0_{kl}$, $\tilde{G}_{\mathbf{k}}$ the Fourier transform of the Green function of anisotropic elasticity, which is the inverse of the dynamic matrix of the system, and $\tilde{F}_{\mathbf{k}}$ is the Fourier transform of so-called Kanzaki forces with which a solute atom acts on a host atom of the undistorted host lattice.

Since elastic interactions are long-range in character, and if it is assumed that only heterogeneities considerably larger than a few interatomic distances are expected to contribute to elastic strain energy, a long-wavelength limit of $\tilde{B}_{\mathbf{k}}$ is adequate for computational purposes. In addition, if only the configurationally dependent part of Eq. (3.21) (the second term) is included [9], we have

$$\tilde{B}_{\mathbf{e}} = -e_i \sigma^0_{ij} \Omega_{(jk)\mathbf{e}} \sigma^0_{kl} e_l + < e_i \sigma^0_{ij} \Omega_{(jk)\mathbf{e}} \sigma^0_{kl} e_l > \tag{3.22}$$

where $< ... >$ is a symbol for averaging over all directions of the $\mathbf{k}$-space unit vector $\mathbf{e}$, and $\Omega_{(jk)\mathbf{e}}$ is a Green function tensor reciprocal to $\Omega^{-1}_{(ij)\mathbf{e}} = \lambda_{ijkl} e_k e_l$. For cubic substitutional solutions in two dimensions Eq. (3.22) can be approximated as (shown in appendix C) [9]

$$\tilde{B}_{\mathbf{e}} = B^*(e_1^2 e_2^2 - \frac{1}{8}) \tag{3.23}$$

where e_i is the ith component of a unit vector in reciprocal space along $\mathbf{k}$, and B^* is a material

constant characterizing elastic properties:

$$B^* = \frac{-4\Delta(c_{11}+2c_{12})^2\epsilon_0^2}{c_{11}(c_{11}+c_{12}+2c_{44})}. \tag{3.24}$$

$\Delta = c_{11} - c_{12} - 2c_{44}$ is the elastic anisotropy constant, and $< e_1^2 e_2^2 >= 1/8$. Positive values of B^* describe systems with negative elastic anisotropy. Note that $\tilde{B}_{\mathbf{e}}$ depends only on the direction of the $\mathbf{k}$, but not on its absolute length. Despite its simplicity, Eq. (3.23) approximates $\tilde{B}_{\mathbf{e}}$ in Eq. (3.22) with a very high accuracy. This approach has been successfully applied to theoretical analysis and computer simulations of coherent phase transformations, some results of which will be briefly reviewed in section 3.5.1.

The above consideration, however, assumes that boundary regions between particles and parent matrix stay coherent during the entire transformation process, which is a valid assumption only for small particles at the beginning of the transformation. Strains at coherent interfaces raise the total energy of the system, and for a sufficiently large atomic misfit, or interfacial area, it becomes energetically more favourable to replace a coherent interface with a semicoherent one. Part of the elastic energy is then released via misfit dislocations, which increase the interfacial energy by an amount associated with the dislocations.

In reality there are also systems in which the difference in elastic moduli of the constituent phases cannot be ignored, even in the simplest approximations. For example, it is believed that differences in elastic moduli between precipitates and the parent phase can be important in understanding the morphology of NiAl superalloys [38–40]. Recently Khachaturyan considered the inhomogeneous elastic moduli case in loaded and unloaded conditions [27], where the Green function of homogeneous elasticity is expanded as a perturbation series. The situation is now much more complicated than in elastically homogeneous mixture of phases, since strain induced interactions cannot be reduced to pairwise interactions, but the character of interactions between finite elements changes to a multiparticle one. The elastic energy formulation for dissimilar elastic moduli has not yet been applied to numerical simulations.

For comparison, the formulation of strain mediated interactions in real space is given by Bratkovsky *et al.* [36, 37]. It is represented by means of some appropriate spherical harmonics,

but has a very cumbersome form compared to Khachaturyan's homogeneous elastic moduli expression in reciprocal space.

3.5 Implementing Khachaturyan's microscopic mean field equation in reciprocal space

For the Khachaturyan microscopic equation

$$\frac{dn_i(t)}{dt} = \sum_j M_{ij} \frac{\partial F}{\partial n_j(t)} \tag{3.25}$$

the Bragg-Williams mean field approximation of Eq. (3.11) for the free energy is used. The partial derivative of the free energy is the local chemical potential, the differences of which throughout the system is the driving force for the transformation:

$$\frac{\partial F}{\partial n_i} = \sum_{j \neq i} (V_{ij} n_j + Q_{ij}) + k_B T \ln \frac{n_i}{1 - n_i}. \tag{3.26}$$

Although Eq. (3.25) is straightforward to be implemented directly in real space, simulations are usually carried out in **k**-space to simplify calculations and save CPU-time. This is especially beneficial if the expression for free energy includes multiple integrations, or the elastic energy interaction, which in **k**-space has a relatively simple form.

A Fourier transform of a function is defined as

$$\tilde{f}_{\mathbf{k}} = \sum_{\mathbf{r}} f_{\mathbf{r}} e^{-i\mathbf{kr}}, \tag{3.27}$$

where the summation is over lattice sites **r**. Taking a Fourier transform of Eq. (3.25) gives

$$\frac{d\tilde{n}_{\mathbf{k}}(t)}{dt} = \tilde{M}_{\mathbf{k}} \left[\tilde{V}_{\mathbf{k}} \tilde{n}_{\mathbf{k}}(t) + \tilde{Q}_{\mathbf{k}=0} N_s \delta_{\mathbf{k}} + k_B T \left\{ \ln\left(\frac{n_i(t)}{1 - n_i(t)} \right) \right\}_{\mathbf{k}} \right]. \tag{3.28}$$

The total number of lattice sites in each computational cell is denoted by N_s, and $\delta_{\mathbf{k}}$ is Dirac delta function. Incorporation of elastic energy, Eq. (3.20), into the driving force does not add

much complexity, but the Fourier transform becomes

$$\frac{d\tilde{n}_{\mathbf{k}}(t)}{dt} = \tilde{M}_{\mathbf{k}}\left[(\tilde{V}_{\mathbf{k}} + \tilde{B}_{\mathbf{e}})\tilde{n}_{\mathbf{k}}(t) + \tilde{Q}_{\mathbf{k}=0}N_s\delta_{\mathbf{k}} + k_BT\left\{\ln\left(\frac{n_i(t)}{1-n_i(t)}\right)\right\}_{\mathbf{k}}\right]. \tag{3.29}$$

With interactions up to second nearest neighbours in a two dimensional square lattice, the Fourier transform of the interaction energy V_{ij} becomes

$$\tilde{V}_{\mathbf{k}} = 2V_1[\cos(\frac{2\pi h}{L}) + \cos(\frac{2\pi l}{L})] + 4V_2\cos(\frac{2\pi h}{L})\cos(\frac{2\pi l}{L}) \tag{3.30}$$

where the wave vector in the first Brillouin zone is $\mathbf{k} = \frac{2\pi}{L}(h,l)$, $h,l = 0,\pm1,...,\pm L/2$, and L is the number of lattice sites along each side of the square periodic cell; $N_s = L^2$. The interaction parameters between first and second nearest neighbours are V_1 and V_2, respectively. Allowing only nearest neighbour jumps, and applying the condition $\sum_j M_{ij} = 0$ from Eq. (2.28), we have

$$\tilde{M}_{\mathbf{k}} = -4M_1[\sin^2(\frac{\pi h}{L}) + \sin^2(\frac{\pi l}{L})]. \tag{3.31}$$

It has been assumed in Eqs. (3.28) and (3.29) that $\tilde{Q}_{\mathbf{k}=0} = \sum_{j\neq i} Q_{ij}$ is constant, independent of site i, which is true in the absence of any relaxation of atoms from lattice sites. $\delta_{\mathbf{k}}$ is zero unless $\mathbf{k} = 0$, in which case $\delta_{\mathbf{k}} = 1$. Since $\tilde{M}_{\mathbf{k}=0} = 0$, Eq. (3.29) becomes

$$\frac{d\tilde{n}_{\mathbf{k}}(t)}{dt} = \tilde{M}_{\mathbf{k}}\left[(\tilde{V}_{\mathbf{k}} + \tilde{B}_{\mathbf{e}})\tilde{n}_{\mathbf{k}}(t) + k_BT\left\{\ln\left(\frac{n_i(t)}{1-n_i(t)}\right)\right\}_{\mathbf{k}}\right]. \tag{3.32}$$

At low temperatures, however, when at late times the site occupation probabilities approach 0 and 1, the logarithmic term in Eq. (3.26) diverges rapidly. This causes numerical problems, since time steps have to be very short to keep the order parameters between 0 and 1, and prevent the simulation from crashing. In order to correct this, a penalty function is introduced in the logarithmic term of Eq. (3.32). In simulations reported in chapter 6 this penalty function was chosen as

$$f(n_i) = \frac{1}{1-(2n_i-1)^{2p}}. \tag{3.33}$$

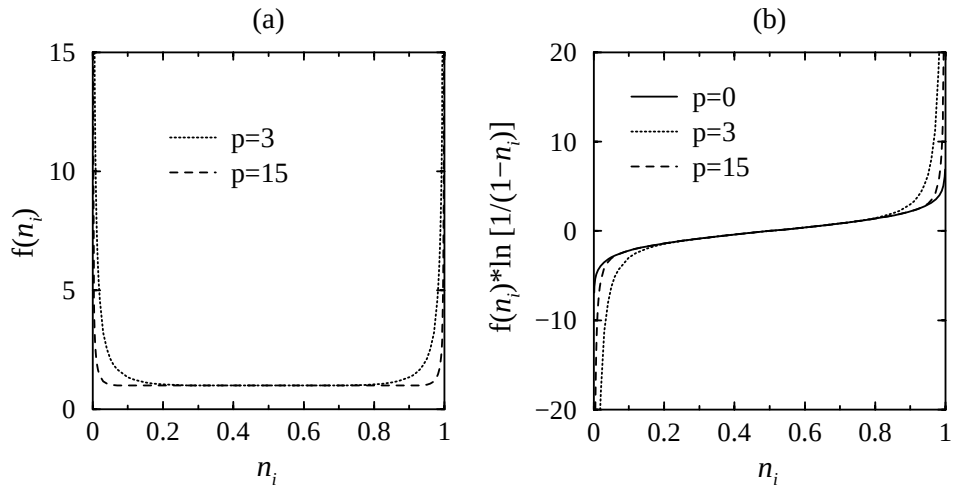


Figure 3.2: (a) Penalty function of Eq. (3.33) with two different values of p. It affects the occupation probabilities near 0 and 1. (b) Effect of penalty function on the logarithmic entropy term.

It is one at $n = 1/2$, and very small around it, but increases rapidly near $n = 0$ and $n = 1$, as shown in Fig. 3.2.(a). The effect of the penalty function on the logarithmic term is shown in Fig. 3.2.(b). Parameter p has to be "large enough" to avoid distortion at compositions far from 0 or 1, but not too large still to possess the desired penalty effect. For my simulations, $p = 20$ was chosen. Therefore, the complete microscopic kinetic equation with penalty reads as

$$\frac{d\tilde{n}_{\mathbf{k}}(t)}{dt} = \tilde{M}_{\mathbf{k}}\left[(\tilde{V}_{\mathbf{k}} + \tilde{B}_{\mathbf{e}})\tilde{n}_{\mathbf{k}}(t) + k_B T\left\{\frac{1}{1-(2n_i-1)^{2p}} \times \ln\left(\frac{n_i(t)}{1-n_i(t)}\right)\right\}_{\mathbf{k}}\right]. \tag{3.34}$$

Equations are differenced in reciprocal space by choosing equally spaced points, the number of which corresponds to the number of lattice sites in real space. Chen *et al.* [41–43] record the temporal evolution of the system by solving the equations with the forward Euler algorithm. It is, however, only first-order accurate in Δt, and its stability is a computational concern. In this particular case, however, the desired effectiveness aimed at by transformation of equations into reciprocal space is partly lost due to the logarithmic term on the right hand side of Eq. (3.34): during each integration step the back-Fourier transformation has to be carried out in order to evaluate the logarithmic entropy term for the next simulation step. This

swapping is costly in CPU-time. The solutions, the Fourier components $\tilde{n}_{\mathbf{k}}(t)$ of the single-site occupation probabilities, are transformed back to real space to produce the temporal evolution of the atomic structure and mesoscale morphologies. Note that the reciprocal space formulation automatically implies the application of periodic boundary conditions.

Although the Euler algorithm is simple, straightforward to implement, relatively fast and requires little storage of previous values of variables compared with many other integration algorithms, it is not very accurate (first-order in Δt). When used, its stability with respect to the time increments should be secured. I have implemented microscopic kinetic field equations both in real and reciprocal space in two and three dimensions. In addition to Euler integration method, I have solved kinetic field equations with the NAG library Runge-Kutta routine. The Runge-Kutta method shows superior performance over Euler with respect to both speed and accuracy. Despite the back-Fourier transformation at each integration step the reciprocal space simulations run remarkably faster than the real space ones. This is because in real space simulations the calculation of the driving force is also a time-consuming task. At each time step a lot of summation over neighbours is needed, and the more nearest neighbours are taken into account the more tedious the calculations become. One of the benefits of solving the time evolution in reciprocal space is that the simulation times are not influenced by the range of the interaction potential. The incorporation of elastic energy does not introduce any additional complexity either. This is because the Fourier transformation of the interactions has to be calculated only once at the very beginning of the simulation. Thereafter they remain intact and each Fourier component can be treated independently throughout the whole simulation, as can be seen from Eqs. (3.30) and (3.34).

When the microstructure develops during the transformation, generally a more advanced algorithm with adjustable mesh size would be most useful. It would capture the detailed changes with decreasing mesh size for example in grain boundary and interface regions, whereas large cells would be adequate in areas where changes are slow and modulated structures exhibit large wavelengths.

3.5.1 Applications of the kinetic field theory - some results reviewed

Precipitation of ordered intermetallics from disordered solid solution is widely used to improve mechanical and physical properties of alloys in modern alloy design. Chen and Khachaturyan [41–43] have carried out simulations of ordering and spinodal decomposition in binary substitutional solutions with a miscibility gap using Khachaturyan's microscopic mean field equation (3.25). One of the advantages of using the microscopic model is its ability to predict the formation of intermediate phases along the transformation path without any a priori knowledge. Their simulations indicated that the decomposition mechanism is mainly associated with an instability in antiphase boundary domain (APB) regions resulting in the replacement of APBs by the equilibrium disordered phase films [41]. It was also found that atomic clustering may be accompanied by ordering and disordering, as a result of which one phase may temporarily have an ordered structure prior to formation of two equilibrium ordered phases [42,43]. Interestingly, these transient ordered states have also been observed in Monte Carlo simulations [44].

The classical Lifshitz-Slyozov-Wagner (LSW) theory considers the coarsening driven by the reduction in total interfacial energy of a system. This coarsening process, however, does not affect the shapes of particles or their spatial distribution, which is known to occur due to strain induced interactions. Khachaturyan's formulation for elastic energy has been used for both theoretical investigations [27, 45, 46] and simulations [46–52] on evolution of coherent precipitates and mesoscale twin and tweed structures in elastic media. The preferred shapes and habits of precipitates are determined by the requirement that the sum of elastic and surface energies be minimized. Both the theory, computer simulations, and experiments have shown that precipitates do not always coarsen monotonically, but may resist coarsening and even decompose into smaller subunits after reaching some critical size.

Khachaturyan *et al.* [45, 46] have considered the crystallographic character of elastic interactions and analytically studied the preferred shapes of a cubic precipitate, as it grows by coarsening. If the elastic mismatch between the precipitate and the matrix can be neglected, it is possible to obtain accurate solutions for the preferred shape. It was observed that with increasing size the precipitate changes from a sphere to a cube to a pair of parallel plates, to a

compact octet of small cubes, and, finally, to a thin plate. The same analysis of decomposition cannot, however, be repeated infinitely: at small particle sizes the interfacial energy increases thus preventing the reverse coarsening. Basically the coarsening can be divided into "interface-controlled" and "strain-controlled" regimes. Coarsening is interface-controlled when particles are very small, and the surface tension dominates the energy of the system. When particles become larger, elastic energy dominates and coarsening is strain-controlled.

Elastic interactions may also be generated due to the formation of ordered domains, which produce twin and tweed structures [49,50]. Precipitation starts from a congruent ordering - just as in the absence of elastic interactions - which results in the formation of a non-stoichiometric ordered single-phase without any preferential alignments. This is because the congruently ordered state is a single phase with almost completely homogeneous composition, and no elastic strains are generated. Morphological alignment develops during decomposition of the congruently ordered phase into the equilibrium ordered and disordered phases, resulting in modulated structures observed in many two-phase alloys.

The effect of long-range Coulomb interactions on dynamics of ordering and phase separation is a relatively seldom discussed topic, although it is directly related to the formation of nanoscale ordered domains for example in oxide compounds. Microscopic Khachaturyan equation (3.25) has been applied to study a ceramic model system undergoing a diffusional transformation involving ions of the same sign [53]. When clustering these ions cause local charge inhomogeneities, which in turn generate local electric fields. This is expected to dramatically increase the electrostatic energy of the system. Now the finite-range interactions compete with screened Coulomb repulsion. In systems with only finite range interactions, the resultant two-phase mixture will continuously coarsen, thus reducing its interfacial energy. Simulations have indicated that the Coulomb interaction has the effect of stopping the coarsening after the ordered particles reach a certain size. It is attractive to assume that the formation of nanoscale ordered domains in ceramic systems could be explained by electrostatic interactions. It has been experimentally observed that the formation of these nanoscale structures contradicts normal coarsening kinetics: although they are formed in a disordered matrix, they do not grow during prolonged aging. An example of a material with both strain induced and

electrostatic interactions is a ceramic oxide $YBa_2Cu_3O_{7-\delta}$. In Refs. [54–56] Khachaturyan's microscopic diffusion equation was applied to study structural transformation kinetics caused by oxygen ordering and to explain the observed mesoscopic structure patterns.

3.6 Discussion

This chapter has addressed the question of how to formulate the thermodynamic driving force for deterministic mean field kinetic equations, which are based on the assumption that even at non-equilibrium states an expression for the "excess" free energy exists. Construction of the free energy functional relies on the order parameter representation of the state of the system. At the atomic level this is usually physically transparent, but with continuum kinetic equations the choice of representative order parameters may be somewhat ambiguous and may already involve some assumptions of the transformation path.

The basic assumption in mean field theories is that each atom interacts only with the mean field of all the other atoms in the system. This concept of an 'average field' is a crucial point at the very heart of all mean field approximations, the consequences of which have been recognized. Moreover, in defining the entropy of the system, it is assumed that the alloying components are ideal and non-interacting, which is far from true in most systems of practical interest. Since, by definition, order parameters are some sort of averages or expectation values of real, fluctuating variables, fluctuations are considered unimportant, and have no role in mean field theories. This is also inherent in Landau theory where the free energy is expanded in terms of the mean value of the local order parameters, rather than allowing an average over all atomic configurations weighted by the appropriate Boltzmann factor. As a result, all mean field models intrinsically suppress nucleation phenomena, which involve a free energy increase enabled by fluctuations! This is why mean field approaches can be valid only in systems, where fluctuations are known to have no significance. These are the prices for the simplicity of mean field theories, which, however, have use as long as the shortcomings and range of applicability are recognized.

The Bragg-Williams mean field free energy was originally designed for systems in which the

order parameter is uniform. It can be generalized to non-uniform systems, which nowadays is the standard approximation for treating the free energy in mean field kinetic equations. The Bragg-Williams and phenomenological Landau theories have a common interface, which is achieved by taking a long wavelength transition of the Bragg-Williams free energy for a non-uniform system. This common interface also supports the scalability of Khachaturyan microscopic mean field equation to the continuum field equations, which was discussed in chapter 2.

Despite the well-known shortcomings, mean field approaches have also had some success and a range of applicability. They usually give correct qualitative predictions for phase diagrams, the construction of which is a relatively simple task compared to phase diagrams generated by Monte Carlo simulations. The accuracy of mean field theories improves for three-dimensional systems, in which the number of nearest neighbour atoms is higher than in two dimensions, and the concept of 'mean field' becomes more justified. Although in systems undergoing phase transformations the respective transformation rates may be distorted when using mean field approaches, the sequences of transformation phases are likely to be correctly described [8, 9]. Generally speaking, mean field approaches provide a feasible approach to complicated problems, and can be used as a starting point for more complicated calculations.

Mean field theories, where interactions are with an average of all the other atoms in the system, improve as the number of nearest neighbours or the range of the interactions increases, as in the presence of infinite range elastic interactions. Incorporation of elastic energy into the driving force is an essential ingredient in modelling many practical systems. The theory for describing elastic interactions is, however, limited to the very early stages of phase transformation, when particle-matrix interfaces remain coherent, and systems in which different phases have the same elastic moduli. Therefore, there is still plenty of scope for some improvement and major breakthroughs in these aspects.

Chapter 4

Stochastic Monte Carlo methods

Monte Carlo techniques generally refer to direct simulation methods that use random numbers to generate a chain of successive configurations starting from some initial configuration. Since randomness is inherently built into Monte Carlo models, they are naturally capable of describing activated and random processes, which occasionally increase the total energy of the system. Monte Carlo models also treat real atoms rather than atomic occupation probabilities used in mean field models, which enables a realistic diffusion mechanism to be defined and applied in models for microstructural evolution in binary alloys.

In this chapter the characteristics of Monte Carlo methods are discussed in comparison to deterministic mean field models, which were discussed in chapter 2. First the commonly used Metropolis algorithm, and Kawasaki and vacancy dynamics underlying the atomic migration in solid solutions are considered. As a next step, residence time algorithms are advanced Monte Carlo simulation techniques through which the problem of defining a physical time scale in Metropolis methods can be settled. Finally, incorporation of elastic energy into Monte Carlo models is discussed.

4.1 Diffusion mechanisms in solids

The operative diffusion mechanism in a solid solution depends on the type of lattice site that is occupied by the diffusing atom [57]. If a solute atom is considerably smaller than solvent atoms of the matrix, it may occupy one of the interstitial sites between solvent atoms. In

The image originally presented here cannot be made freely available via ORA due to copyright reasons.

Figure 4.1: (a) Diffusion in interstitial solid solutions. The solute atoms are generally smaller in size than the solvent atoms, and they may migrate relatively easily between the solute atoms. (b) Direct exchange and ring mechanism in substitutional solid solutions. (c) Diffusion through vacancy motion (reproduced after [57]).

interstitial diffusion the smaller solute atoms migrate through the interstitial sites by forcing their way between the larger solvent atoms, as shown in Fig. 4.1.(a). Often the concentration of interstitial atoms is so low that only a small fraction of available sites is occupied. Therefore interstitial atoms are usually surrounded by vacant sites, and atoms can jump to neighbouring positions if the thermal energy is sufficient to overcome the energy barrier for atomic migration.

In substitutional alloys, solute atoms have replaced some of the solvent atoms in the lattice. Normally atoms are not as free to move to other sites as in interstitial solutions, since the movement of a substitutional atom is restricted by its neighbours. In principle, there are several possible mechanisms for substitutional diffusion to take place [57]. One possibility is a direct interchange of neighbouring A and B atoms, as in Fig. 4.1.(b). If this is to occur by rotating the atoms around their joint center of separation, the exchange will distort the surrounding crystal structure enormously, and cause long-range elastic strains. The activation energy for this process is very high, and consequently the probability of such a direct exchange is extremely low in metallic crystals. An extension to the direct exchange mechanism is a co-operative process of ring diffusion, shown in Fig. 4.1.(b). If a small number of atoms move together as a ring, the lattice distortion is spread over a larger volume and the activation energy is reduced compared to the direct pair exchange. Another mechanism would be the movement through interstitial sites, similar to the mechanism in Fig. 4.1.(a), with the migrating atom arriving

finally at a vacant substitutional site. Alternatively, the migrating atom may displace another substitutional atom into an interstitial site, if there are no vacant sites available [57]. Such atomic migration will also be energetically expensive and hence unlikely, unless the structure happens to be very open.

The most common mechanism for diffusion in metals is through vacancies: atoms next to a vacant site may jump into it. The relative motion of A and B atoms results from the migration of vacancies through the lattice. The rate at which atoms are able to migrate depends on how often they encounter vacancies, and are able to exchange sites. This in turn is determined by the concentration of vacancies in the solid, and atomic attempt frequencies. Both the probability of atomic jumps and vacancy concentration are sensitive to the temperature: at higher temperatures atoms vibrate more vigorously and the formation of point defects, such as vacancies, is enhanced. In pure metals self diffusion occurs through random motion of vacancies, but in ordered alloys random vacancy motion would disrupt the ordered arrangement of atoms on lattice sites. In that case a highly correlated six-jump vacancy cycle has been found to be the most favourable mechanism energetically [58, 59].

4.2 Kawasaki and vacancy dynamics

The probability P_i of having a configuration with energy E_i in a system follows the Boltzmann distribution, $P_i \propto \exp(-E_i/k_BT)$. In a Metropolis algorithm for Monte Carlo simulations, a new trial configuration j with energy E_j is proposed, and the probability of this new configuration relative to the old configuration i is [1]

$$\frac{P_j}{P_i} = \exp\left(-\frac{E_j - E_i}{k_BT}\right). \tag{4.1}$$

If P_j/P_i is greater than unity, i.e. the move would decrease the total energy of the system, the new configuration j is accepted. If the energy of the new state is larger than the previous state,

[1] The Metropolis function of Eq. (4.1) is not the only possible choice for transition probability. There are other choices, such as Glauber function $\frac{P_j}{P_i} = \frac{1}{2}(1 - \tanh(\Delta E/k_BT)$. Note that in Glauber dynamics with $\Delta E = 0$ the exchange probability is 0.5 compared to 1.0 in Metropolis dynamics. This affects the rate at which the system approaches equilibrium [60].

i.e. $E_j > E_i$ and P_j/P_i is less than one, the new configuration is accepted with probability P_j/P_i. This is done by comparing P_j/P_i with a random number r between 0 and 1: if r is less than P_j/P_i, the new configuration is accepted. By allowing moves that increase the energy, we ensure that the system does not get stuck in a local minimum. Clearly, the higher the temperature, the greater the chance for the acceptance of a configuration which increases the energy. For the next atomic jump the initial configuration is the accepted configuration from the previous step.

There are different mechanisms of how configurational changes in a model system for a binary alloy can occur. In Kawasaki dynamics a change in energy is considered for a swop, in which an exchange of two randomly chosen neighbouring atoms of different types is proposed. This choice of dynamics corresponds to an unrealistic direct exchange mechanism of Fig. 4.1.(b), which is extremely unlikely to occur in real alloys. However, in spite of this obvious unphysicality of the diffusion mechanism, Kawasaki dynamics has been often used in modelling microstructural evolution in binary alloys. It has been widely thought that the microstructures of diffusional processes are not qualitatively affected by the details of the underlying diffusion mechanism.

In a more realistic vacancy diffusion mechanism one of the neighbouring atoms of the vacancy is (randomly) chosen to jump to the vacant site, and the acceptance is subject to the Metropolis decision. Usually only jumps of nearest neighbour atoms to the vacant site are allowed. With vacancy dynamics only the areas in the immediate proximity of the vacancy are affected, whereas Kawasaki dynamics generates changes throughout the lattice.

Time in conventional Metropolis Monte Carlo simulations is measured as Monte Carlo steps per site. Once the number of attempts equals the total number of sites in the lattice, one Monte Carlo step has been made. Since the sites visited are chosen randomly [2], during one Monte Carlo step some sites may have been visited several times, while some others are completely ignored. A realistic time scale can be assigned to kinetic processes, if saddle point energies and atomic vibration frequencies are known. This is done in next section using a residence time Monte Carlo algorithm.

[2] With Kawasaki dynamics also a sequential sweep through the lattice has sometimes been used.

4.3 Residence time Monte Carlo algorithm

The residence time algorithm [61–64] was developed to increase the efficiency of the usual Metropolis algorithm, which becomes very slow at low temperatures due to the high rejection rate of trial moves. Since the probability of accepting moves that increase internal energy becomes extremely small at low temperatures, the system becomes easily trapped at metastable states with the Metropolis algorithm.

In conventional Monte Carlo simulations, a constant - but arbitrary - time increment is chosen such that at most one event occurs during each increment. This time increment has no direct connection to real physical time. In residence time algorithms a realistic time scale can be defined through atomic vibration frequencies and activation energy barrier heights. Also, the residence time algorithm *always* allows one event at each step, but the time increment is variable. The use of a variable time step enables events that occur on a wide range of time scales to be modelled [65]. The residence time method has been found to be equivalent statistically to conventional Monte Carlo schemes with a fixed time step [63].

4.3.1 First order algorithm

Consider a vacancy surrounded by z nearest neighbours, as in Fig. 4.2.(a). Each neighbouring atom i of the vacant site is vibrating around its equilibrium lattice position with frequency ν_i. For simplicity, the masses and the attempt frequencies of A and B atoms in the alloy are assumed to be equal [3]. In order to jump to the vacant lattice site, an atom has to overcome an activation free energy barrier of height $E_a^i = E_s^i - E_1^i$ (Fig. 4.2.(b)), where E_s^i is the environmentally dependent saddle point energy and E_1^i is the initial energy state of the jumping atom i. Activation energy barriers for vacancy migration are sensitive to the local atomic environment, and vary, in general, from site to site. This is captured in our model, the results of which are discussed in chapter 6, in a physically sensible fashion by making the saddle point

[3] This condition can be easily relaxed to dissimilar attempt frequencies and masses.

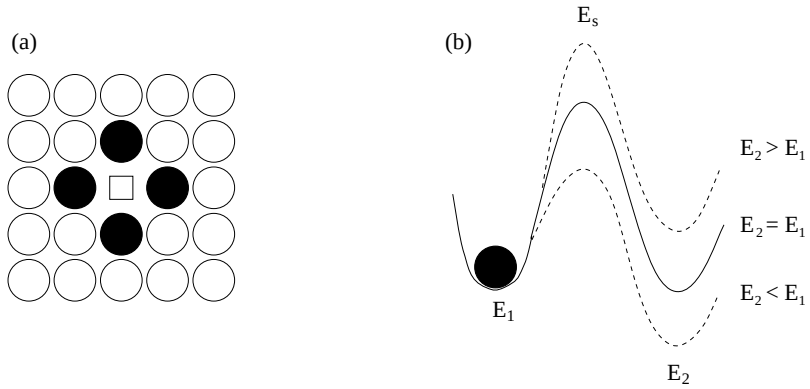


Figure 4.2: (a) Nearest neighbour atoms of the vacancy (square) in a 2D square lattice model are competing to jump to the vacant site. (b) Atomic jump probabilities depend on the activation energy barrier height $E_a = E_s - E_1$. E_1 and E_2 are the energies of initial and final states of the jumping atom. Saddle point energy is environmentally dependent, and given by Eq. (4.2).

energy a function of both the initial and final states [66]:

$$E_s^i = \frac{E_1^i + E_2^i}{2} + e_0. \tag{4.2}$$

The constant e_0 is fixed throughout the simulation, and is chosen such that all activation energies are positive[4]. The effect of the final state is included directly through the saddle point energy: a higher E_2 increases the saddle point (and activation) energy for the jump, as shown Fig. 4.2.(b). Our choice is also symmetric with respect to initial and final states, and satisfies detailed balance. Note that $E_a^i = e_0 + \frac{E_2^i - E_1^i}{2}$, which varies linearly with the energy difference, $E_2^i - E_1^i$, between the initial and final states, as in the Metropolis function of Eq. (4.1).

For the ith atom surrounding a vacancy the transition probability per unit time is

$$\omega_i = \nu_i \exp(-E_a^i / k_B T). \tag{4.3}$$

[4]More generally, e_0 may be expected to be a function of the average composition in a region that is large compared with the atomic scale but small compared with the wavelength of macroscopic compositional modulations. In the context of the present atomistic simulations e_0 will then be a function of the average composition in the computational supercell.

The relative probability that the vacancy will jump to any of its neighbours is

$$\alpha_i = \frac{\nu_i e^{-E_a^i/k_BT}}{\sum_j \nu_j e^{-E_a^j/k_BT}} \tag{4.4}$$

where the sum is over the nearest neighbours of a vacancy [5]. A random number r between 0 and 1 is generated, and the vacancy jumps to the site k that fulfils the condition

$$\sum_{i=1}^{k-1} \alpha_i < r \leq \sum_{i=1}^{k} \alpha_i. \tag{4.5}$$

In the residence time Monte Carlo algorithm a time scale is defined through the atomic vibration frequencies and activation energy barrier heights. It is assumed that atoms take their equilibrium lattice positions before the vacancy jumps. The mean residence time τ is the average time the system is expected to remain in a given configuration between vacancy jumps:

$$\tau = \frac{1}{\sum_i \nu_i e^{-E_a^i/k_BT}}. \tag{4.6}$$

In the Metropolis algorithm a vacancy jump is accepted if a random number (between 0 and 1) is less than $\exp(-\Delta E/k_BT)$, where ΔE is the energy associated with the vacancy-atom exchange. At low temperatures the rejection rate increases dramatically if the vacancy is trapped at a low energy site, and the Metropolis algorithm becomes inefficient. By contrast, with the residence time algorithm a transition is made at each step even at very low temperatures, and the time increment is given by Eq. (4.6). Note that the mean residence time at all sites is directly proportional to $\exp(e_0/k_BT)$, and thus the mobility is proportional to $\exp(-e_0/k_BT)$.

4.3.2 Second order algorithm

Although a vacancy jump is made at every attempt, the first order residence time algorithm does not take into account the possibility that the vacancy may jump straight back to its previous lattice position. This corresponds to a rejection in the conventional Monte Carlo sense, since the atomic configuration has not changed, but time has elapsed. The first order

[5] Or, if next nearest neighbour jumps are allowed, the sum goes over all atoms competing to jump.

residence time Monte Carlo procedure has been extended to higher order algorithms [64], which take into account the unproductive direct reverse jumps. The original derivations of the second and third order algorithms are given in Ref. [64]. In this section a slightly different derivation of the second order algorithm from that given in Ref. [64] is presented.

In order to eliminate direct reversals, transition probabilities should be modified. If α_i is the normalized probability for a vacancy to jump to site i (Eq. (4.4)), let us denote by $\hat{\alpha}_i$ the probability that the vacancy jumps directly back to its previous site. The probability for this reversal jump is now

$$\bar{\beta}_i = \alpha_i \hat{\alpha}_i, \tag{4.7}$$

and the probability that the vacancy does not jump back directly is

$$\beta_i = \alpha_i (1 - \hat{\alpha}_i). \tag{4.8}$$

Correspondingly, the probability that the vacancy makes a reversal jump to any neighbouring site is

$$\bar{\beta} = \sum_i \bar{\beta}_i, \tag{4.9}$$

and the probability for a jump to any neighbouring site without a direct reversal is

$$\beta = \sum_i \beta_i. \tag{4.10}$$

Note that $\beta + \bar{\beta} = 1$.

If the last vacancy jump was say from site j, we can write the probability for other types of jumps (second order jumps i.e. direct jumps to other lattice sites, or jumps after performing at least one reversal):

$$1 - \alpha_j = \sum_{i \neq j} \beta_i + (\sum_{i \neq j} \bar{\beta}_i)(1 + ... + \bar{\beta}^n + ...)(\sum_i \beta_i). \tag{4.11}$$

The first term corresponds to direct escapes to any neighbouring site except j and the second represents the probabilities for $1, 2, .., n, ..$ reversal jumps before escaping. From Eq. (4.11) we can distinguish relative transition probabilities for indirect jumps back to site j, P_j, and to sites $i \neq j$, $P_{i\neq j}$:

$$P_j = \frac{1}{1-\alpha_j}[(\sum_{i\neq j}\bar{\beta}_i)(1 + ... + \bar{\beta}^n + ...)\beta_j] = \frac{1}{1-\alpha_j}\frac{\sum_{i\neq j}\bar{\beta}_i}{\beta}\beta_j \tag{4.12}$$

$$P_{i\neq j} = \frac{1}{1-\alpha_j}[\beta_i + (\sum_{i\neq j}\bar{\beta}_i)(1 + ... + \bar{\beta}^n + ...)\beta_i] = \frac{1}{1-\alpha_j}[1 + \frac{\sum_{i\neq j}\bar{\beta}_i}{\beta}]\beta_i \tag{4.13}$$

Note that in Eq. (4.12) a direct jump back to j is forbidden.

As seen from Eq. (4.11), the second order residence time is a weighted average of direct escape times and escapes after performing reverse jumps. The time related to direct escapes, excluding j, is $\sum_{i\neq j}\beta_i\tau$, where τ is the (first order) residence time at the site the vacancy is currently occupying. The average time spent during a single reversal is a weighted average of all the reverse jumps to the neighbouring sites:

$$\tau_S = \frac{\sum_i \bar{\beta}_i(\tau + \tau_i)}{\sum_i \bar{\beta}_i} \tag{4.14}$$

where τ_i is the (first order) residence time at site i, given by Eq. (4.6). The expected number of reversals done is [6]

$$\frac{\bar{\beta} + 2\bar{\beta}^2 + 3\bar{\beta}^3 + ...}{\bar{\beta} + \bar{\beta}^2 + \bar{\beta}^3 + ...} = \frac{1-\bar{\beta}}{\bar{\beta}}\frac{\bar{\beta}}{(1-\bar{\beta})^2} = \frac{1}{\beta} \tag{4.15}$$

and the average time spent on reversals is $\frac{\bar{\beta}}{\beta}\tau_S$. If the vacancy does not escape directly the average time spent on the first reversal differs from the average time spent on subsequent reversals, because a direct jump back to j is forbidden:

$$\tau_S^{(j)} = \frac{\sum_{i\neq j}\bar{\beta}_i(\tau + \tau_i)}{\sum_{i\neq j}\bar{\beta}_i}. \tag{4.16}$$

[6] For an arithmetic-geometric series $a + (a+b)x + (a+2b)x^2 + (a+3b)x^3 + ... = \frac{a}{1-x} + \frac{bx}{(1-x)^2}$, if $|x| < 1$.

The average time spent on reverse jumps prior to escaping is a weighted sum of different reversal events:

$$\begin{aligned}(\sum_{i\neq j}\bar{\beta}_i)\beta(\tau_S^{(j)}+\tau)+(\sum_{i\neq j}\bar{\beta}_i)\bar{\beta}\beta(\tau_S^{(j)}+\tau_S+\tau)+(\sum_{i\neq j}\bar{\beta}_i)\bar{\beta}^2\beta(\tau_S^{(j)}+2\tau_S+\tau)\\ +(\sum_{i\neq j}\bar{\beta}_i)\bar{\beta}^3\beta(\tau_S^{(j)}+3\tau_S+\tau)+...\\ =\sum_{i\neq j}\bar{\beta}_i\tau_S^{(j)}+\sum_{i\neq j}\bar{\beta}_i\tau+(\sum_{i\neq j}\bar{\beta}_i)\frac{\bar{\beta}}{\beta}\tau_S.\end{aligned} \tag{4.17}$$

Therefore, the second order mean residence time is the average of the time associated with direct escapes, excluding to site j, i.e. $\sum_{i\neq j}\beta_i\tau$, and of the average time spent on reverse jumps prior to escaping, Eq. (4.17), scaled by the probability of a second order jump:

$$\tau^{(2)}=\frac{1}{1-\alpha_j}[(\sum_{i\neq j}\beta_i)\tau+(\sum_{i\neq j}\bar{\beta}_i)(\tau_S^{(j)}+\tau+\frac{\bar{\beta}}{\beta}\tau_S)] \tag{4.18}$$

which is equivalent to Eq. (B9) of [64].

This is the residence time for a system with only one vacant site, but it can easily be extended to systems with several vacancies. In that case, however, the simulation time is affected dramatically, and the desired effectiveness of residence time algorithms is lost, as the number of possible transition at each attempt increases. Consider a system with two vacancies, for example. Now at each attempt the transition probabilities have to be calculated to all neighbours of *both* vacancies. Since the number of possible moves has doubled, the mean residence time at each configuration is halved on average. Consequently, the physical time spent on two events roughly corresponds to the same physical time that with one event in a system with one vacancy. Therefore, if the same total amount of physical time is required, it can be seen that the computing time increases as N_V^2, where N_V is the number of vacancies in the system. On the other hand, if the same total number of jumps is required, the computing time scales as N_V.

4.4 Incorporation of elastic energy

In principle, the Khachaturyan formulation for microscopic elastic energy for an elastically homogeneous system, Eq. (3.20), is directly applicable to Kawasaki Monte Carlo models. If vacancy dynamics are used, however, a correction due to the relaxation of the lattice around the vacant site is required.

There are only few Monte Carlo studies with elastic interactions included. Fratzl and Penrose [67,68] have studied phase separation in alloys with anisotropic elastic interactions. In their model the elastic energy is modelled through linear springs joining pairs of atoms, and long-range elastic interactions result from differences in sizes of A and B atoms. Between the jumps the atoms are assumed to have enough time to adopt minimum energy positions near lattice sites. In that case the energy can be expressed in $\mathbf{k}$-space in terms of the arrangements of atoms only, as in Khachaturyan's microscopic elasticity. If the average domain size of the microstructure is large compared to the interatomic distance, only $\mathbf{k}$-values close to zero contribute considerably to the total elastic energy. In that case the "elastic potential" depends on the direction of the reciprocal vector $\mathbf{k}$, but not on its absolute value. The spring model for elasticity takes into account the dispersion of $|\mathbf{k}|$, which may be important in the formation of small precipitates. Like Khachaturyan's microscopic elasticity, the spring model still suffers from the fact that particles with dissimilar elastic moduli cannot be described within the formalism.

Willis and Gosling [31] proposed a real-space microscopic theory for elastic interactions that allows local variations in elastic response. The energy associated with particular local patterns of atoms is described through multipoint correlation functions. This theory has potential applications in kinetic equations for microstructural evolution, which require the evaluation of energy changes upon interchange of atoms in specified local environments. At present there are no other methods that are able to assess differences in elastic moduli. So far this aspect of phase transformations has remained largely unexplored, since no computer simulations have been carried out using the lattice statics description of elastic energy of Ref. [31].

4.5 Discussion

Many transformation processes in metallic alloys depend on the details of the diffusion mechanism. Mean field models discussed in chapter 2 either have no information about the diffusion mechanism, or are based on the master equation of direct exchange mechanism. Usually vacancies can be added into the models by treating them as the third alloy component. This, however, does not allow any truly sensible description of atomic migration processes, either: the nature of the order parameter is continuous, and transformations result from free energy minimization rather than local stochastic atomic processes.

In Monte Carlo models for binary alloys A and B atoms are located in rigid lattice sites. The atoms vibrate around their equilibrium lattice positions until occasionally some of them gain enough thermal energy to change local configuration. A kinetic Ising model with Kawasaki dynamics is very simple, transparent, and easy to implement, but an unphysical choice for the underlying mechanism of phase transformations. Although this fact is well recognized, it has been often assumed that the kinetics and resulting morphologies are not affected by this choice of dynamics. The direct exchange mechanism brings about changes uniformly throughout the system, and it is impossible to assign any realistic time scale to Kawasaki dynamics. A linear dependence between the Monte Carlo steps and the physical time is often assumed, but there are no rigorous arguments to justify this assumption.

With vacancy dynamics only areas near the vacant site are affected. Changes in remote areas take place only if the vacancy diffuses to them. A vacancy diffusion mechanism together with a residence time algorithm is a remarkable improvement to the standard Metropolis method. Atomic migration is sensitive to the details of the local atomic environment, and this can be incorporated into the model through environmentally dependent saddle point energies. A time scale can then be assigned to each jump through atomic masses, vibration frequencies and activation energy barriers. Moreover, unlike in Metropolis algorithm, a jump is made at every attempt, which considerably improves the efficiency especially at low temperatures. The first order residence time algorithm has been extended to more advanced second and third order algorithms, which circumvent the unproductive direct reversal jumps and second reversals.

This can be done by defining a higher order residence time which includes the contribution of configurationally unproductive (back and forth) moves. Residence time algorithms are most efficient in systems, where the number of possible moves at each attempt is small, i.e. there is only one vacant site in the system. If there are several events occurring simultaneously, such as several vacancies jumping, these are not addressed with Monte Carlo models in a simple way.

In real systems there may be other processes, such as defect recombination and elimination, which may have some importance for phase transformations, but cannot easily be taken into account in Monte Carlo models. Only conservative point defects have been considered, although the non-conservative nature of point defects may sometimes be important [69]. During a quench from the high temperature state into a miscibility gap, the number of vacancies decreases due to annihilation. In Monte Carlo models, like in mean field models, the A and B atoms are located in rigid lattice sites, so that only coherent phase transformations can be modelled. For real metals, however, this may sometimes be too great a simplification, because it also affects the atomic migration: diffusion is a structure sensitive phenomenon, and the activation energy for diffusion is lower in regions of 'bad' crystal, such as dislocations and interfaces.

Salje and coworkers [70, 71] have combined Monte Carlo and molecular dynamics modelling techniques in studying phase transformations in minerals. Now atoms are not required to remain in rigid lattice positions, but are allowed to move to minimize the total energy of the system. Forces on each atoms are calculated exactly, and proposed atomic moves are subject to a Monte Carlo decision. This approach naturally allows deformations due to elastic interactions, and formation of interface dislocations, but is computationally costly. Each proposed configuration has to be the relaxed, and for each Monte Carlo step several configurations have to be evaluated. Another problem arises from the time scale: at low temperatures it is assumed that each configuration is fully relaxed before the next move is made, and therefore the time scale of the model is determined by the Monte Carlo procedure. At high temperatures, however, it is not obvious that atoms have enough time to adjust themselves to the minimum energy lattice configuration before the jump, and therefore the time scale does not necessarily arise directly from the Monte Carlo process, but has some ambiguity in it [7].

[7] Here I acknowledge E. Salje for a useful discussion in Portugal in April 1997.

The contribution of elastic interactions to the internal energy can, in principle, be calculated in the same way as in mean field models. Computationally it is, however, a much more laborious procedure than in the microscopic mean field model, especially if combined with a residence time algorithm. This is because energies for *each* proposed configuration have to be computed in order to assign the transition probabilities. This involves several back and forth Fourier transforms, which will slow down the computation considerably. The load of computing may be somewhat eased by utilizing lookup tables, as Fratzl and Penrose have done [68].

Analytic results are more readily derived with mean field than Monte Carlo models. In order to obtain statistically satisfactory results, averages over several independent Monte Carlo runs are required. In Monte Carlo models, all correlations are automatically included, whereas the mean field approximation ignores all correlations.

Chapter 5

Coarsening theories

5.1 The role of interface energy

The microstructure of a two-phase alloy may be unstable owing to the finite energy of interfaces it contains. This interfacial energy is reduced through coarsening, which often produces an undesirable degradation of material properties, such as loss of strength. A fine dispersion of hard precipitate particles in a metallic matrix, such as in a copper-aluminium system, for example, is one of the most important microstructures in metallic alloys. This is achieved by a rapid quench to room temperature, when a supersaturated solid solution is obtained. On subsequent annealing thermal energy enables nucleation, through which numerous small particles are formed. Ageing of the alloy results in a transition from a fine dispersion of coherent particles to a coarse dispersion of particles with incoherent interfaces. These structures provide different resistances to dislocation motion. When interparticle spacing increases, dislocations are able to bypass the particles. Therefore, increase in interparticle spacing will rapidly reduce the strength of the alloy, as the microstructure coarsens over time.

Typical interfacial energies in metallic alloys vary from 0.02 J/m^2 to 1.0 J/m^2 [72], the smallest values being for a fully coherent precipitates with a small lattice misfit, e.g. for ordered Ni_3Al precipitates in nickel matrix [38]. An alloy containing particles with an interparticle spacing of 30 nm, for example, will have approximately 4×10^{22} precipitates per cubic metre. If the precipitate volume concentration is 5 percent and interfacial free energy 0.2 J/m^2, the

total interfacial area in the alloy is 5×10^6 m^2/m^3, giving an interfacial energy 1 MJ/m^3 of alloy. If the interparticle spacing, however, is 10 times larger, interfacial energy is reduced to 1×10^5J/m^3, which is 10 times less than for the fine particle distribution. Therefore, for the very fine precipitates seen in the electron microscope there is still a considerable driving force for microstructural coarsening.

5.2 Gibbs-Thompson effect

Interphase interfaces can become extremely important in the early stages of phase transformation, when one phase, say A is present as very fine particles in the other phase, B. Due to the curvature of the A/B interface, A particles are subjected to an extra pressure, like a balloon exerts an extra pressure on the air inside it. If γ is the interfacial energy, and particles are spherical with radius R, the extra pressure is

$$\Delta P = \frac{2\gamma}{R}. \tag{5.1}$$

This pressure results in a difference in molar Gibbs free energy

$$\Delta G = \frac{2\gamma V_m}{R} \tag{5.2}$$

where V_m is the molar volume of the A phase. An increase in free energy due to interfacial energy is called capillarity, or Gibbs-Thompson effect, which shifts the free energy curves of A phase precipitates compared to infinitely large particles, as shown in Fig. 5.1. An important practical consequence of the Gibbs-Thompson effect is that the solubility of A in B is sensitive to the size of A particles. The common tangent construction in Fig. 5.1 shows that the concentration of A in B, c_R, in the immediate vicinity of A particle of radius R is greater than c_∞, the solute concentration near an infinitely large particle (i.e. "infinite" R). If the two phases are almost pure A and pure B, and we have a regular solution [1] the Gibbs-Thompson equation

[1] For regular solutions the enthalpy of mixing ΔH varies parabolically with composition, $\Delta H \propto c_A c_B = c_A(1 - c_A)$. As often in solids, the pV term in enthalpy $H = U + pV$ is small, and $\Delta H \approx \Delta U$, the change in internal energy. In ideal solutions the enthalpy of mixing $\Delta H = 0$, and the free energy change accompanying mixing is only due to the change in entropy.

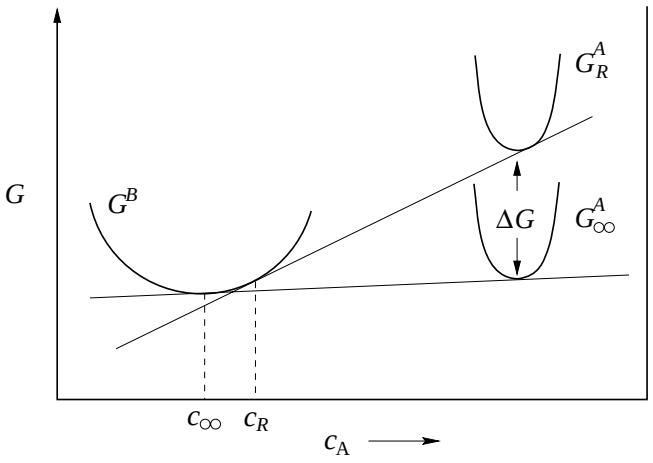


Figure 5.1: The effect of interfacial energy on the solubility of small particles. The free energy curve of A phase is shifted due to the finite particle radius, Eq. (5.2), and the solubility of A in B increases from c_∞ to c_R.

gives the equilibrium solute concentration in the matrix c_R near the A phase precipitate of radius R [2]

$$\ln \frac{c_R}{c_\infty} = \frac{2\gamma V_m}{R_0 T R} \tag{5.3}$$

where R_0 is the molar gas constant. Therefore, in Fig. 5.2 the solute concentration in the matrix in equilibrium with the small precipitate is greater than with the larger particle, and this creates concentration gradients in the matrix. There is a diffusive flux of A atoms from smaller to larger particles, which results in the shrinkage of small particles and the growth of large particles, such that the average particle size increases.

5.3 Ostwald ripening and LSW-theory

In Ostwald ripening small particles shrink and large particles grow, because, due to the Gibbs-Thompson effect, small particles are in equilibrium with higher solute concentration in the matrix. As a consequence, the total number of particles decreases, and the average particle size $\bar{R}$ increases. Particles of different sizes are distributed randomly throughout the system,

[2] The detailed derivation of Gibbs-Thompson equation is given for example in Ref. [72].

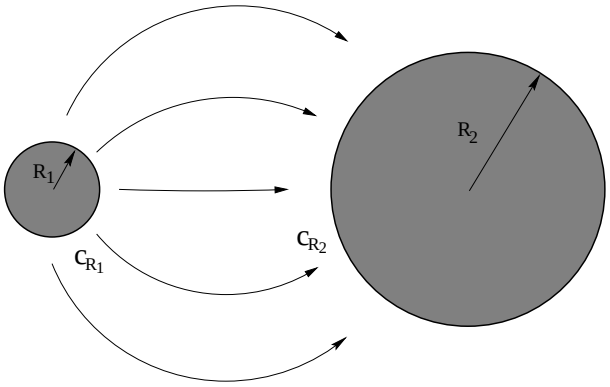


Figure 5.2: Two particles of radii R_1 and R_2. Since the solute concentration in the vicinity of the smaller particle is greater than in the vicinity of the bigger particle, $c_{R_1} > c_{R_2}$, there is a diffusive flux of solute from the smaller to the larger particle.

and solving the solute diffusion between the particles rigorously is not a simple task. Here we follow the outlines of the theory deriving the growth law for Ostwald ripening, which over the years has been analysed at various levels of details [73–76]. Theoretical results by Lifshitz and Slyozov [73] and independently by Wagner [74] are mathematically rigorously derived - thus giving the name for the theory. Here we follow a less mathematical, but maybe more illuminating, treatment of the Ostwald ripening process [72].

In applying the Gibbs-Thompson equation (5.3) to precipitate coarsening we consider a system where the volume fraction of particles is small, and the interparticle spacing is large, i.e. several particle diameters. Particles are assumed to have spherical shapes with isotropic interfacial energies. If the energy barrier for atomic transport across the matrix-precipitate interface is low, the limiting process controlling the coarsening rate is diffusion of solute atoms through the matrix. The solute concentration c_R in the matrix near a particle of radius R is given by the equilibrium Gibbs-Thompson value of Eq. (5.3). The solute concentration inside a particle is c_A (assumed to be close to one), and at distances far from the particle, $r >> R$, it is $c_{\bar{R}}$, which is the equilibrium solute concentration in the matrix corresponding to the average particle radius $\bar{R}$. The non-uniform solute concentration around particles of different sizes in different regions in the system causes solute diffusion through the matrix, through which the microstructure coarsens towards lower free energy.

Consider a single particle i in an ensemble of particles in the system. If particle i is growing,

at distance r from its surface there is a diffusive flux (in moles per second) of solute to the particle:

$$j = -\frac{4\pi r^2 D}{V_m}\frac{\partial c}{\partial r}, \tag{5.4}$$

where c is concentration as molar fraction [3], and D is diffusivity. The minus sign indicates that the flux is down the concentration gradient. This is the flux feeding the growth of the particle. If the number of moles, n, inside a particle is

$$n = \frac{V}{V_m} = \frac{4\pi R^3}{3V_m} \tag{5.5}$$

the change of moles in the particle, as it grows, changes as

$$\frac{dn}{dR} = \frac{4\pi R^2}{V_m}, \tag{5.6}$$

or, as a function of time, as

$$\frac{dn}{dt} = \frac{\partial n}{\partial R}\frac{dR}{dt} = \frac{4\pi R^2}{V_m}\frac{dR}{dt}. \tag{5.7}$$

Since Eq. (5.7) is the molar growth rate of the particle, and Eq. (5.4) describes the flux supplying solute for the growth, by equating Eqs. (5.7) and (5.4) we obtain

$$-\frac{dr}{r^2} = \frac{Ddc}{R^2(dR/dt)}. \tag{5.8}$$

Integrating this from the surface of the precipitate to large distances (in terms of interparticle spacing), where the composition of a solution in equilibrium with particles of average radius $\bar{R}$ is $c_{\bar{R}}$, we obtain

$$\int_R^\infty -\frac{dr}{r^2} = \int_{c_R}^{c_{\bar{R}}} \frac{Ddc}{R^2(dR/dt)}. \tag{5.9}$$

[3] c/V_m would be concentration as atoms per unit volume.

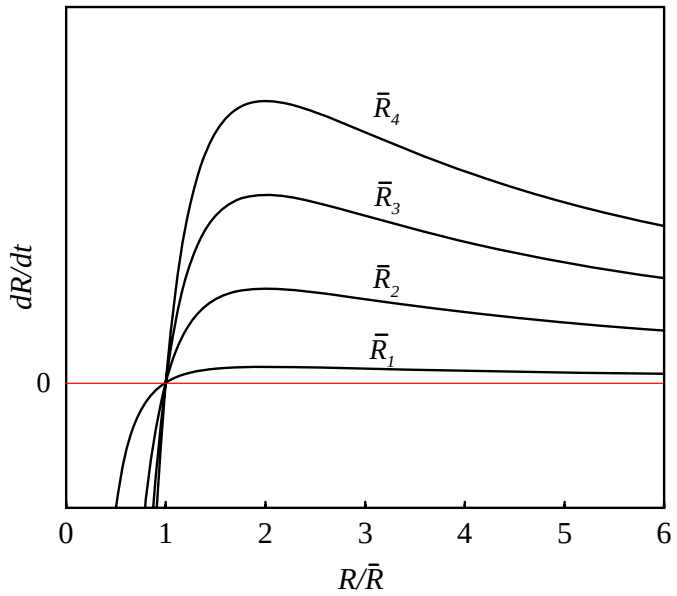


Figure 5.3: Normalized growth rates for increasing average particle sizes, e.g. increasing times: $\bar{R}_1 > \bar{R}_2 > \bar{R}_3 > \bar{R}_4$.

If the growth rate dR/dt is assumed independent of concentration, the integration gives

$$\frac{1}{R} = \frac{D}{R^2(dR/dt)}(c_{\bar{R}} - c_R) \tag{5.10}$$

or, with help of Gibbs-Thompson equation (5.3),

$$\frac{dR}{dt} = \frac{2D\gamma V_m c_\infty}{R_0 T R}(\frac{1}{\bar{R}} - \frac{1}{R}) \tag{5.11}$$

Fig. 5.3 shows normalized growth rates at different times of coarsening. Particles are shrinking (i.e. $\frac{dR}{dt} < 0$), if their size R is smaller than the average particle size $\bar{R}$. As R becomes smaller, e.g. $R/\bar{R}$ approaches to zero, the rate of shrinking accelerates until the particle disappears. Particles of radii larger than $\bar{R}$ are growing, but as $\bar{R}$ increases, the growth rate for all precipitate sizes decreases. Particles with fastest growth rate obey $\frac{d}{dR}(\frac{dR}{dt}) = 0$, which gives

$$-\frac{2D\gamma V_m c_\infty}{\bar{R} R_0 T R^2} + \frac{4D\gamma V_m c_\infty}{R_0 T R^3} = 0, \tag{5.12}$$

or $R = 2\bar{R}$. Some of the particles that initially were growing, i.e. $(dR/dt > 0)_{t=0}$ may later be shrinking, if their growth rate is less than $(dR/dt)_{max}$. In that case they are overtaken by faster growing nearby particles, and at later times they start to shrink. From Fig. 5.3 we also see that for particles larger than $R = 2\bar{R}$ the growth rate is less than $(dR/dt)_{max}$, and they will be caught up by faster growing particles of size $2\bar{R}$. As a result, the mean particle size $\bar{R}$ increases with time, and the distribution of particle sizes becomes coarser. After some time it is expected that there are no particles much larger than $2\bar{R}$ in the system. Therefore, it can be approximated that at late times the growth rate for the average particle size follows the growth rate of the fastest growing particles of size $2\bar{R}$:

$$\frac{d\bar{R}}{dt} = (\frac{dR}{dt})_{max} \tag{5.13}$$

which yields

$$\bar{R}^3(t) - \bar{R}^3(0) = \frac{3}{2}\frac{D\gamma V_m c_\infty t}{R_0 T}. \tag{5.14}$$

The rigorous - and more laborious - analysis of Lifzhitz and Slyozov [73] and Wagner [74] gives a result that differs from Eq. (5.14) only in the numerical constant:

$$\bar{R}^3(t) - \bar{R}^3(0) = \frac{8}{9}\frac{D\gamma V_m c_\infty t}{R_0 T}. \tag{5.15}$$

or

$$\bar{R}^3(t) = A + Bt \tag{5.16}$$

where $A = \bar{R}^3(0)$ and $B = \frac{8}{9}\frac{D\gamma V_m c_\infty}{R_0 T}$. Despite its simplicity and the number of assumptions made in the derivation, relatively ideal [4] systems, such as Co/Cu, and Li/Al systems can be expected to follow the $t^{1/3}$ growth law of Eq. (5.15) [77]. However, significant deviations are observed in most cases. This is not too surprising due to several approximations made in

[4] Systems with approximately spherical particles and interfaces with a high step density.

the simple model. The assumption of well separated particles becomes invalid at large solute volume fractions. In that case the validity of uniform equilibrium solute concentration in the matrix far away from particles fails due to the proximity of particles. At high solute concentrations, diffusion along interfaces cannot be neglected even at high temperatures. Moreover, for particles that have grown into non-equilibrium shapes, simultaneous coarsening and particle shape equilibration may complicate the analysis considerably.

5.4 Huse's extension to LSW-theory

Huse proposed some finite-time corrections to LSW-theory, which takes into account the effect of diffusion along domain-boundaries [78]. This extends the theory to cases, where instead of isolated particles the structure forms interconnected domains. At interfaces diffusivity is enhanced, because there are more low-energy paths available for transport. At low temperatures transport along interfaces dominates, and coarsening cannot be considered as a classical LSW-evaporation and condensation process. Diffusion along interfaces becomes less important at higher temperatures, since diffusion across the interface is also operative.

Huse considered a system that is near local equilibrium at length scales small compared to a characteristic length scale R in the system. The interfaces have a local curvature of order R. The solute concentration near interfaces is then (from Eq. (5.3))

$$c_R \propto \exp(\frac{2\gamma V_m}{R_0 T R}) \tag{5.17}$$

and local differences in solute concentration, which cause diffusional fluxes in the system, can be approximated [5] as

$$\begin{aligned} c_{R_1} - c_{R_2} &\propto \exp(\frac{2\gamma V_m}{R_0 T R_1}) - \exp(\frac{2\gamma V_m}{R_0 T R_2}) \\ &\approx (1 + \frac{2\gamma V_m}{R_0 T R_1}) - (1 + \frac{2\gamma V_m}{R_0 T R_2}) \propto \frac{1}{R_1} - \frac{1}{R_2}. \end{aligned} \tag{5.18}$$

These variations in composition occur over a distance R, giving compositional gradients of

[5] at high enough temperatures and large R's

order $1/R^2$. If coarsening is limited by lattice diffusion, the characteristic length scale grows as

$$\frac{dR(t)}{dt} \sim \frac{A}{R^2(t)}. \tag{5.19}$$

This gives a growth law equivalent to the Lifshitz-Slyozow-Wagner law, Eq. (5.15). If the volume fraction of solute is non-vanishing, the assumption of well separated particles fails, and interfaces play an increasingly important role during coarsening. The amount of interface per unit volume is of order $1/R$. If diffusion occurs only along domain boundaries in connected microstructures, the driving force for coarsening, $\sim 1/R^2$, is multiplied by the availability of transport channels, i.e. the amount of interface. In this case the coarsening rate becomes

$$\frac{dR(t)}{dt} \sim \frac{B}{R^3(t)} \tag{5.20}$$

giving a power law description $R \sim t^n$, with $n = 1/4$. If both diffusion mechanisms - along and across the interface - are important and operative simultaneously, we have

$$\frac{dR(t)}{dt} \sim \frac{A}{R^2(t)} + \frac{B}{R^3(t)} = \frac{AR + B}{R^3(t)} \tag{5.21}$$

or

$$\int_{R(0)}^{R(t)} \left[\frac{1}{A} R^2(t) - \frac{B}{A^2} R(t) + \frac{B^2}{A^2} \frac{R(t)}{AR(t) + B} \right] dR \sim \int_0^t dt \tag{5.22}$$

which, after integration, gives

$$\frac{1}{3A}[R^3(t) - R^3(0)] - \frac{B}{2A^2}[R^2(t) - R^2(0)] + \frac{B^2}{A^3}[R(t) - R(0)] - \frac{B^3}{A^4}\left[\ln \frac{AR(t) + B}{AR(0) + B}\right] \sim t. \tag{5.23}$$

Since in Eq. (5.23) at late times R^2 and R^3 terms dominate over the linear and logarithmic

terms, they have only little effect in the asymptotic analysis. For large R and t we then have

$$R(t) \sim (3At)^{1/3} + \frac{B}{2A} + O(t^{-1/3}). \tag{5.24}$$

The effective coarsening exponent n_{eff} is defined as

$$n_{eff}(t) \equiv \frac{d[\ln R(t)]}{d[\ln t]} = \frac{t}{R(t)} \frac{dR(t)}{dt} \tag{5.25}$$

which applied to Eq. (5.24) yields

$$n_{eff} = \frac{t}{3R(t)} (3A)^{1/3} t^{-2/3} = \frac{1}{3}(1 - \frac{B}{2AR(t)}). \tag{5.26}$$

In their Monte Carlo study with vacancy dynamics, Yaldram and Binder [79] obtained an estimate for the growth exponent that was somewhat lower than the theoretical LSW-prediction. Fratzl and Penrose [80,81] compared Kawasaki and vacancy dynamics, and especially at lower temperatures for a 50/50 binary alloy they had no difficulties in achieving the asymptotic behaviour with vacancy dynamics. Frontera *et al.* [82, 83] reported similar results. Extensive simulations with Kawasaki dynamics by Amar *et al.* [84] finally confirmed Huse's theory of increasing effective exponent with an asymptotic value of 1/3 - with vacancy dynamics no such extensive simulations of increasing exponent have been carried out.

5.5 Binder-Stauffer theory for particle diffusion

At temperatures well below T_c the thermal energy available may be insufficient to allow solute atoms to escape into the matrix. Instead of being controlled by the diffusivity of solute through the matrix, the rate limiting process is now diffusion across interfaces, if the solute is present in the form of isolated particles. Coarsening proceeds through Brownian motion of particles rather than LSW-evaporation and condensation of atoms. Binder and Stauffer [85–87] proposed a phenomenological theory for coarsening, where entire particles diffuse without changing size, until they meet and coalesce to form one bigger particle.

Binder and Stauffer showed that there are at least four mechanisms for particle diffusion,

The image originally presented here cannot be made freely available via ORA due to copyright reasons.

Figure 5.4: Different mechanisms of particle diffusion: (a) atomic movement along the particle surface (b) atom evaporates and condenses back to the particle (c) matrix atom moves within the particle (d) atom from a different particle attaches to the particle, and another atom evaporates (after Ref. [88]).

shown in Fig. 5.4. In Fig. 5.4.(a) an atom moves at the surface of the particle without any cost of energy. In Fig. 5.4.(b) an atom evaporates from the surface of the particle, and condenses back to the same particle a few lattice spacings further along. In Fig. 5.4.(c) diffusion results from an interior displacement of one of the atoms of the species forming the matrix in which particles diffuse, and in Fig. 5.4.(d) diffusion occurs by condensation of one atom from a neighbouring particle, and evaporation of another from the particle.

At low temperatures, it is assumed that the mechanism described in Fig. 5.4.(a) dominates, since the activation energy for the atomic evaporation that occurs in Figs. 5.4.(b) and (d) is too high. Also, at low temperatures particles consists of pure A-atoms in B-matrix, so the 'bubble' diffusion of Fig. 5.4.(c) is suppressed. The diffusion constant of a particle is defined as $D = \omega(\Delta x_G)^2$, where Δx_G is the shift in the center of mass position due to some atomic movement, and ω is the rate at which these atomic diffusion processes occur. At low temperatures, the particle volume V_m is directly proportional to the number of atoms l in the particle, $V_m \propto l$. Since at low temperatures atomic diffusion takes place at the particle surface, the rate of atomic diffusion processes is proportional to the number of surface sites. At low

temperatures for roughly spherical particles, the particle radius scales as $R \propto l^{\frac{1}{d}}$. The number of surface sites is therefore $S_l \propto R^{d-1}$, giving $\omega \propto S_l \propto l^{1-1/d}$. As a result of atomic movement, the position of the centre of mass of the particle changes as $\Delta x_G \propto l^{-1}$. Therefore the particle diffusivity reads as $D \propto l^{-1-1/d}$.

If the average size of particles is R, the number of particles in the system is proportional to R^{-d}, and the average distance between particles is $\Delta r \propto (R^d)^{1/d} = R$. The average time needed for the particle to travel distance Δr is $\Delta t \propto R^2/D$. Coalescence of two particles produces a change in particle size $\Delta l \propto R^d$. The rate law can now be written as

$$\frac{dl}{dt} \propto \frac{\Delta l}{\Delta t} \propto \frac{R^d}{R^2/D} = DR^{d-2}. \tag{5.27}$$

By inserting D and recalling that $R \propto l^{1/d}$, we have

$$\frac{dl}{dt} \propto l^{-1-\frac{1}{d}} l^{\frac{d-2}{d}} = l^{-\frac{3}{d}} \tag{5.28}$$

which, after integration, gives a growth law

$$l \propto t^{\frac{d}{3+d}}. \tag{5.29}$$

From this we get for the average particle radius, R, in the system

$$R \propto t^{\frac{1}{3+d}}, \tag{5.30}$$

giving $R \propto t^{1/5}$ in two, and $R \propto t^{1/6}$ in three dimensions. This simplified analysis assumes that only one diffusion mechanism, e.g. free atomic motion on particle surface, is responsible for particle diffusion. In reality, however, the particle movement may be effected by several competing particle diffusion processes simultaneously. In addition, if atomic motion is mainly due to vacancy hopping, the analysis will be altered, since the vacancy is likely to be trapped at interfaces at low temperatures.

5.6 Discussion

This chapter summarizes some of the theories governing time evolution of microstructural coarsening, as the average particle size increases, driven by the reduction of interfacial energy. If coarsening is limited by diffusion of solute through the matrix, the problem of describing diffusion among a distribution of particles of different sizes and shapes is mathematically very complicated. In that case even the most advanced theories involve a number of simplifications, which limit the validity of theories to well defined, almost ideal systems.

Lifzhitz-Slyozov-Wagner theory is the most famous attempt to describe time evolution of an ensemble of particles, which are well separated from each other. It applies the Gibbs-Thompson equation to describe fluxes between particles of different sizes, and gives a power law prediction $\bar{R} \propto t^{1/3}$ for late times of coarsening, when the steady state particle size distribution has been achieved. LSW-theory assumes isotropic interfacial energies, spherical particle shapes and negligible volume fraction of solute, and therefore its validity in real systems is very restricted. Nevertheless, due to the lack of any better theories for diffusion limited coarsening, the LSW-theory serves as a well established benchmark to many experimental systems and computer simulations.

Huse proposed some simple but intuitively plausible extensions to the LSW-theory. His amendments extend the theory to cases, where solute concentration is non-negligible, and the structure forms interconnected domains instead. In that case diffusion along interfaces plays a significant role during coarsening even at late times, and the effective coarsening exponent n_{eff} approaches its asymptotic value of 1/3, as the amount of interface decreases.

At low temperatures diffusion across interfaces becomes the limiting factor for coarsening. Instead of Ostwald ripening, the microstructure coarsens through Brownian motion of particles, which diffuse randomly, and coalesce to form larger particles. This mechanism is not within the scope of LSW-Huse analysis. At low temperatures the activation energy for an atom to evaporate from a particle is too high to establish solute concentration gradients near particles. For coarsening by coalescence Binder and Stauffer developed a phenomenological theory, which predicts coarsening exponents smaller than LSW-theory: 1/5 in 2D and 1/6 in

3D. For simplicity, this theory assumes that atomic movement along particle surfaces is the mechanism enabling particle diffusion, but if other mechanisms are operative simultaneously, as is likely to happen in real systems, the analysis becomes more complicated. Also, if atomic diffusion is effected by vacancy motion, the vacancy has to enter the particle sometimes to cause a net displacement of the center of mass the particle. This consideration would make the Binder-Stauffer theory more realistic.

In summary, theories describing time evolution of a coarsening microstructure are all very idealized, and involve a number of simplifications and assumptions about concentration, interfacial energies and particle shapes. Moreover, they do not take into account effects like elastic or electrostatic energies. In spite of these known shortcomings, together with numerous computer simulations these theories have promoted understanding of what could be happening during coarsening in real systems, whenever experimental data is rare, or difficult to interpret.

Chapter 6

Comparison of the methods

6.1 Introduction

In this chapter morphologies, coarsening mechanisms and kinetics are compared in a systematic way, when phase separation is modelled using deterministic mean field and stochastic Monte Carlo methods. Some comparisons are also made in a model system undergoing simultaneous ordering and phase separation, and finally some of the trends observed in two dimensional simulations for phase separation and coarsening are compared with those obtained in three dimensions. For the mean field approach a linear microscopic diffusion equation due to Khachaturyan [8, 9] is employed, and a variation of it with an environment dependent mobility. Monte Carlo simulations are carried out with vacancy and Kawasaki dynamics, and a residence time algorithm [61–64] is applied in the vacancy case. Although these models are commonly used to model phase transformations, the influence of the diffusion mechanism on microstructural evolution has received little attention, especially the kinetics.

The first question addressed in this chapter is the correspondence of mean field and Monte Carlo models in describing phase transformations in binary alloys. Mean field models are based on the assumption that there exists a free energy functional describing both equilibrium and non-equilibrium states of a system. In Khachaturyan's microscopic mean field model the rate of change of the local order parameter is linear with respect to the local thermodynamic driving force. In principle, this description of kinetics is valid when a system is not too far

from its equilibrium state, and the driving force for the transformation is small. Also, instead of treating entire atoms, mean field models use atomic occupation probabilities, which are continuous variables. Therefore, the mechanism of atomic diffusion does not appear explicitly, and dynamics of fluctuations do not arise naturally, but can be introduced through an additional thermal noise term. In Monte Carlo models changes in site occupancies are effected by direct exchanges of pairs of neighbouring atoms, or through vacancy motion. Examples of cases in which these differences between deterministic and stochastic models affect the course of the phase transformation are given throughout this chapter.

Another important question discussed is how the choice of diffusion mechanism in the Monte Carlo model affects the morphology, kinetics and the coarsening mechanism of a binary alloy undergoing phase separation. Most Monte Carlo studies on phase separation and coarsening have been carried out by allowing neighbouring dissimilar atoms to undergo direct exchanges, known as Kawasaki dynamics, although in real metals such direct exchanges are very unlikely to occur. Nevertheless, it has been widely assumed that morphologies and kinetics of the evolving microstructures during phase separation are not affected by this choice of diffusion mechanism. So far there has been no detailed comparative studies between the two mechanisms in this respect, although some recent publications have referred to the question [80, 89]. Some aspects of the effect of diffusion mechanism on simultaneous phase separation and ordering will be also briefly discussed, since it is a problem receiving increasing attention in modelling communities due to its technological importance in NiAl superalloys.

A physical time scale can be assigned in a vacancy dynamics Monte Carlo model through atomic attempt frequencies and activation energy barriers, but can physical time somehow be defined with Kawasaki dynamics, or in mean field models? With Kawasaki dynamics time is measured as Monte Carlo time, i.e. attempts of exchanges per lattice site. Although there is no evident physical justification for correspondence between time in Kawasaki simulations and real time, since diffusion in real alloys is almost always effected by vacancy hops and not by direct atomic exchanges, a linear dependence between the Monte Carlo time and real physical time is often assumed. As for the mean field models, time is defined through atomic mobility, which is either treated as being constant, or environment dependent. By examining the effect of

a realistic diffusion mechanism on a binary system undergoing phase transformation, a critical discussion of the time scales in microscopic mean field models and a Monte Carlo model with Kawasaki dynamics can be presented.

Finally, most studies on phase transformations in binary alloys have been carried out in two dimensional model systems - most often in a simple square lattice. This naturally prompts the question, to what extent two dimensional simulation results are representative of what happens in real three dimensional systems. Therefore some simulations of phase separation and coarsening are repeated in a three dimensional cubic lattice for comparisons to be made.

6.2 Review of the models

6.2.1 Microscopic mean field model

For the mean field approach a microscopic diffusion equation due to Khachaturyan [8, 9] is employed. It is a direct counterpart of the continuum Cahn-Hilliard equation that applies to a binary alloy at the microscopic level:

$$\frac{dn_i(t)}{dt} = \sum_j M_{ij} \frac{\partial F}{\partial n_j(t)}. \tag{6.1}$$

$n_i(t)$ is the probability that site i is occupied by an A-type atom, and in free energy F the Bragg-Williams approximation is used for the configurational entropy:

$$F = \frac{1}{2} \sum_{i,j} V_{ij} n_i n_j + k_B T \sum_i [n_i \ln n_i + (1 - n_i) \ln(1 - n_i)]. \tag{6.2}$$

In Eq. (6.1) M_{ij} is a mobility for diffusional jumps between nearest neighbour sites i and j. It is chosen to be constant, i.e. environment independent, in most of the simulations. For comparison, this condition is later relaxed, and an environment dependent mobility is introduced. Note that Eq. (6.1) is a linearized version of a more general microscopic diffusion equation (Eq. (2.44) in chapter 2), originally derived from a microscopic master equation by Martin and Vaks [18, 19].

In this study, a 128×128 real space lattice with periodic boundary conditions is used.

Initially each lattice site is assigned a composition, which deviates by a small random amount from an average value, corresponding to a high temperature disordered state. Time evolution of the system is solved in reciprocal space, as described in detail in section 3.5.

6.2.2 Monte Carlo model with vacancy dynamics

The second approach employed in this study is a Monte Carlo model with a second order residence time algorithm. One lattice site is vacant, corresponding to a vacancy concentration of $1/128^2 = 6.1 \times 10^{-5}$, which is a realistic value for a metallic alloy. Interaction energies between nearest neighbour ($p = 1$) and next nearest neighbour ($p = 2$) atoms are denoted by ϵ_p^{AA}, ϵ_p^{BB} and ϵ_p^{AB}, and interactions between atoms and the vacancy are set to zero. The total energy of the system is written as

$$\begin{aligned} H = \sum_{p=1,2} \sum_{<ij>_p} \frac{1}{4} [\epsilon_p^{AA}(1+\sigma_i)(1+\sigma_j) + \epsilon_p^{BB}(1-\sigma_i)(1-\sigma_j) \\ + \epsilon_p^{AB}((1+\sigma_i)(1-\sigma_j) + (1-\sigma_i)(1+\sigma_j))] \\ - \sum_{p=1,2} \sum_{<vj>_p} \frac{1}{4}(\epsilon_p^{AA} - \epsilon_p^{BB})\sigma_j + C_0 \end{aligned} \tag{6.3}$$

where σ_i is 1,-1, or 0, if the ith site is occupied by an A-atom, a B-atom or a vacancy [1]. The first sums are over all nearest neighbour (NN) and next nearest neighbour (NNN) bonds, the last sums go over the NN and NNN bonds of the vacancy, and C_0 is a constant. If $\epsilon_p^{AA} = \epsilon_p^{BB}$, Eq. (6.3) can be rearranged as an Ising type Hamiltonian

$$H = J_1 \sum_{<NN>} \sigma_i\sigma_j + J_2 \sum_{<NNN>} \sigma_i\sigma_j + C_1 \tag{6.4}$$

in which $J_1 = \frac{1}{4}(\epsilon_1^{AA} + \epsilon_1^{BB} - 2\epsilon_1^{AB})$ and $J_2 = \frac{1}{4}(\epsilon_2^{AA} + \epsilon_2^{BB} - 2\epsilon_2^{AB})$ are the NN and NNN interactions and C_1 is a constant.

The initial state for the simulation is a completely disordered state, where atomic occupations are determined by a random number generator subject to the selected average composition being attained. This corresponds to an infinite temperature, $T = \infty$, state of the system. The

[1] The site occupation probability n_i in the mean field model is an expectation value of $\frac{\sigma_i+1}{2}$.

sample is quenched below T_c into the two phase regime in its phase diagram. The system evolves through a second order residence time Monte Carlo algorithm, which was discussed in section 4.3. All changes in site occupancies are effected by the motion of the single vacancy, which is allowed to perform jumps only to nearest neighbour positions. For comparison, some simulations with direct exchange Kawasaki dynamics were also carried out.

6.3 Phase separation and coarsening

In the mean field model atomic interactions between nearest and next nearest neighbours were chosen to be $V_1 = -1$ and $V_2 = -1/\sqrt{2}$, in arbitrary units. The mean field critical temperature for phase separation is $k_B T_c^{MF} = |V_1 + V_2|$. A schematic phase diagram of a system with a miscibility gap is shown in Fig. 6.1.

In order to make parameters of the Monte Carlo model comparable to the mean field model, they were chosen to be negative, and $J_1/J_2 = \sqrt{2}$. By using grand canonical ensembles and a fourth order cumulant method [92] the critical temperature of the Monte Carlo system was estimated to be $k_B T_c = 2.58|J_1 + J_2|$. The equilibrium properties of the model system are assumed to be unaffected by the low vacancy concentration. The longest low temperature Monte Carlo runs with vacancy dynamics include 20000 updates per site. However, each update is not equivalent to a conventional Monte Carlo step per site, since there are no unsuccessful jumps in the residence time algorithm, and direct reversal jumps back are not allowed.

For the vacancy Monte Carlo simulations, e_0 in Eq. (4.2) has to be chosen so that the activation energy $E_a^i = E_s^i - E_1^i$ is always positive. In the following simulations it was chosen as $e_0 = \frac{1}{2}(E_{max} - E_{min}) + 1$, where E_{max} (E_{min}) is the maximum (minimum) energy when summed over the NN and NNN bonds of an(y) atom in the system. Therefore, in a two dimensional square lattice $E_{min} = -4|J_1 + J_2|$ and $E_{max} = 4|J_1 + J_2|$, giving $e_0 = 4|J_1 + J_2| + 1$. With only nearest neighbour interactions we have $e_0 = 4|J_1| + 1$.

The critical temperatures for the mean field and Monte Carlo models are different, but the simulations were run for the same normalized temperatures T/T_c to enable meaningful comparisons to be made. However, the mean field and Monte Carlo phase diagrams have

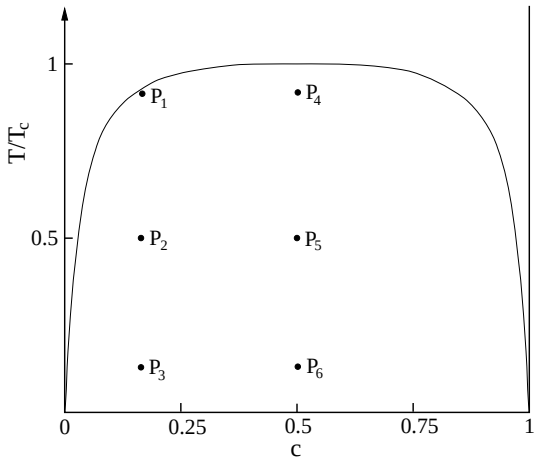


Figure 6.1: Schematic phase diagram for phase separation. Points $P_1 - P_6$ within the miscibility gap show some quenches discussed in the text.

different shapes, e.g. the Monte Carlo phase diagram is "broader". Therefore the degrees of undercooling for Monte Carlo and mean field models are not fully comparable at other compositions than $c = 0.50$. Because accurate phase diagrams for Monte Carlo models with second nearest neighbour interactions were not available, it was decided to run the simulations at same T/T_c rather than, for example, at the same undercooling.

6.3.1 Morphologies

Fig. 6.2 shows snapshots of evolving microstructures following a quench to $T/T_c = 0.16$ with $c = 0.50$ (P_6 in Fig. 6.1), and run times are chosen so as to give the same average domain sizes in the mean field and Monte Carlo models. These microstructures are interconnected domains, which coarsen over time. At the beginning of the phase separation, Figs. 6.2.(a) and 6.2.(b), there are no significant differences between the predicted microstructures. At later stages the Monte Carlo simulations show a preferred alignment of the domains along $\langle 11 \rangle$ directions (Fig. 6.2.(d)) which is not seen in the mean field microstructures (Fig. 6.2.(c)). The change in morphology in Monte Carlo simulation of Figs. 6.2.(b) and (d) is confirmed by corresponding diffraction intensity patterns in Fig. 6.3. At the earlier stage (Fig. 6.3.(a)) the round shape of the diffraction pattern indicates uniform alignment of structures, but later peaks in $\langle 11 \rangle$ directions appear (Fig. 6.3.(b)).

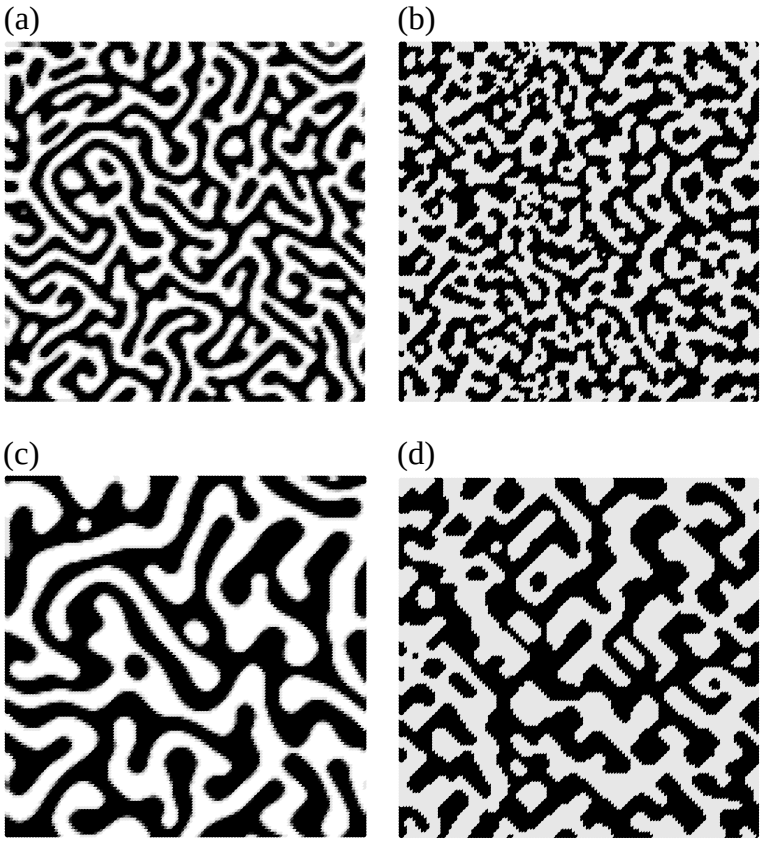


Figure 6.2: Snapshots of evolving microstructures with $c = 0.50$ and $T/T_c = 0.16$. (a) and (c) are mean field (constant mobility), (b) and (d) Monte Carlo vacancy model results. Simulation times are in (a) $t = 1.9 \times 10^7$, (b) $t = 1.2 \times 10^7$, (c) $t = 7.0 \times 10^7$, (d) $t = 2.9 \times 10^8$. In the mean field microstructures white corresponds to pure A-regions ($n_i = 1$), and black pure B-regions ($n_i = 0$), and gray shading denotes intermediate compositions. The average domain sizes in each left and right pair are equal.

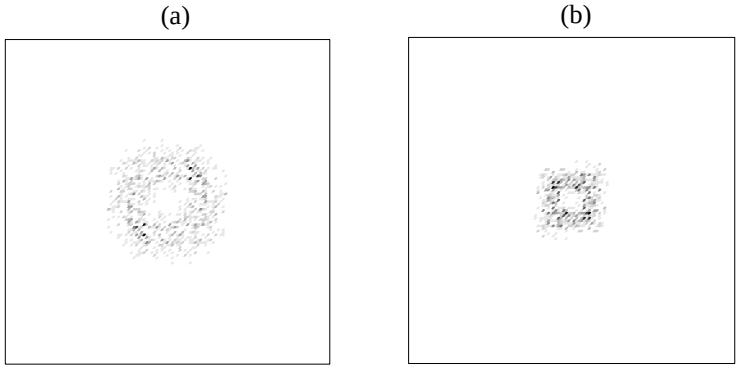


Figure 6.3: Diffraction patterns of Figs. 6.2.(b) and (d) indicating microstructural alignment along $\langle 11 \rangle$ directions. Wave vector $\mathbf{k} = (0, 0)$ is located in the center of the figures.

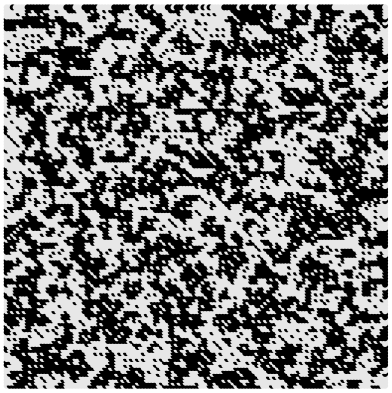


Figure 6.4: Snapshot of a microstructure obtained with the vacancy Monte Carlo model, $c = 0.50$ and $T/T_c = 0.16$. Only next nearest neighbour vacancy jumps jumps are allowed. Although in this way only half the lattice sites can be visited, appearance of $\{10\}$ facets can be distinguished. The simulation time is $t = 1.6 \times 10^8$.

The energies per unit length of $\{10\}$ and $\{11\}$ facets are $\frac{2}{a}|J_1 + 2J_2|$ and $\frac{2\sqrt{2}}{a}|J_1 + J_2|$ respectively [2], where a is the square lattice parameter. With $J_1/J_2 = \sqrt{2}$, as in the present case, the energies of $\{10\}$ and $\{11\}$ facets are equal. The predominance of $\{11\}$ facets in Fig. 6.2.(d) is not, therefore, a result of anisotropy of the interfacial energy.

The binding energies of a vacancy to the $\{10\}$ and $\{11\}$ interfaces are $2|J_1 + 2J_2|$ and $2|2J_1 + J_2|$, respectively (i.e. with $J_1/J_2 = \sqrt{2}$ the binding energy is higher to $\{11\}$ interfaces). Therefore, at low temperatures the vacancy becomes trapped at the interfaces. Since the vacancy is allowed to hop only along $\langle 10\rangle$ nearest neighbour directions, vacancy migration along a $\{11\}$ facet involves the vacancy leaving the interface at a cost of $4|J_1|$ energy. This energy is recovered when the vacancy returns to the interface at a $\langle 11\rangle$ primitive vector further along. By contrast, there is no energy cost associated with vacancy migration parallel to a $\{10\}$ interface, and steps on $\{10\}$ interfaces are therefore much more mobile than those on $\{11\}$ interfaces. Consequently, steps move along $\{10\}$ facets rapidly until they reach $\{11\}$ facets and then become relatively immobile. In this way $\{11\}$ facets become predominant, because they are the least mobile interfaces in the system. This interpretation was checked by allowing the vacancy to hop only to next nearest neighbour sites, i.e. along $\langle 11\rangle$ directions,

[2] See appendix D.

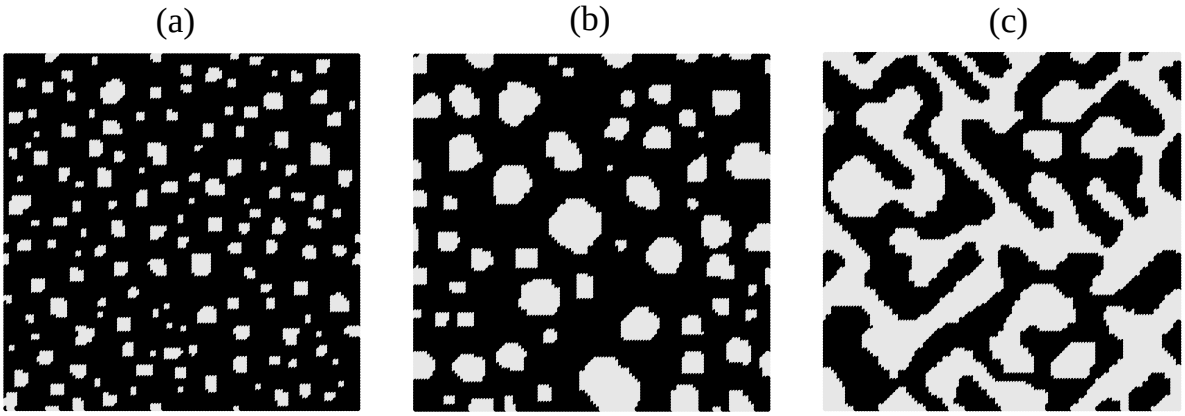


Figure 6.5: Snapshots of evolving microstructures obtained with vacancy dynamics Monte Carlo simulations with $J_2 = 0$. In (a) $c = 0.15$, $t = 2.5 \times 10^6$, (b) $c = 0.25$, $t = 1.0 \times 10^7$, (c) $c = 0.50$, $t = 2.6 \times 10^6$. The absolute temperature is same as in Figs. 6.2.(b) and (d) and 6.9.(a), corresponding to a relative temperature $T/T_c = 0.30$.

and a snapshot of resulting morphology is shown in Fig. 6.4. In that case vacancies become mobile on $\{11\}$ facets and relatively immobile on $\{10\}$ facets, and therefore $\{10\}$ facets are expected to predominate at larger concentrations and particle sizes. Although only half the lattice sites are accessible with vacancy jumps along $\langle 11 \rangle$ vectors, simulations confirmed the preferred tendency for $\{10\}$ facets.

Further simulations were carried out to illuminate the role of the vacancy diffusion mechanism through nearest neighbour jumps. A system without second nearest neighbour interactions, i.e. $J_2 = 0$, was chosen. Now the interface energies are $E^{\{10\}} = \frac{2}{a}|J_1|$ and $E^{\{11\}} = \frac{2\sqrt{2}}{a}|J_1|$, giving $\{10\}$ interfaces lower energy. The resulting microstructures with different concentrations are shown in Fig. 6.5. At low concentrations, Fig. 6.5.(a), particles clearly prefer $\{10\}$ interfaces. As solute concentration increases and particles become larger, Fig. 6.5.(b), small particles still align themselves along $\langle 10 \rangle$ directions, but larger ones have various shapes. This is because the shape equilibration of large particles takes longer time than that of small particles. As average particle size increases, this equilibration becomes slow compared to the coarsening process so that the $\langle 10 \rangle$ alignment which is preferred by energetics is obscured. At equal concentrations, Fig. 6.5.(c), the structure forms interconnected domains and diffusion along interfaces is important. Despite the higher energy of $\{11\}$ interfaces, they

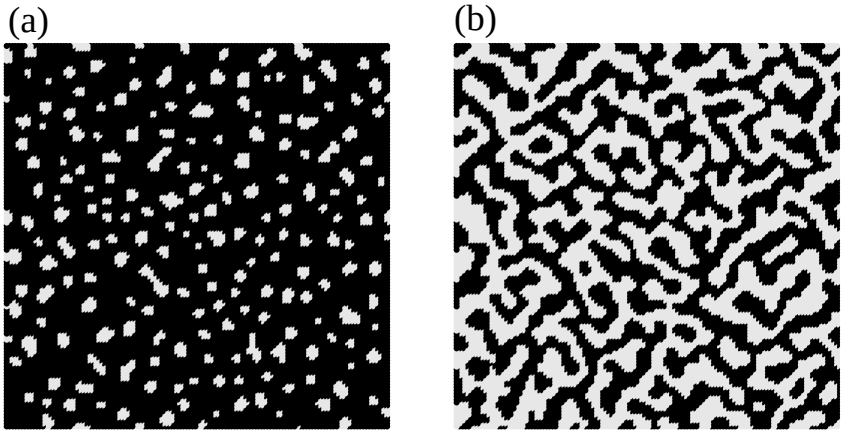


Figure 6.6: Snapshots of evolving microstructures obtained with Kawasaki dynamics Monte Carlo simulations at $T/T_c = 0.16$. In (a) $c = 0.15$, $t = 7.2 \times 10^4$ (MCS) and (b) $c = 0.50$, $t = 1.2 \times 10^5$ (MCS).

are clearly dominant in the microstructure in Fig. 6.5.(c): this is due to the slow vacancy motion and atomic transport along {11} interfaces compared to {10} interfaces. This clearly demonstrates the importance of vacancy diffusion mechanism in microstructural coarsening: interfacial energies alone are not the only factor to determine the (an)isotropy of microstructures since it is also strongly influenced by factors associated with the mechanism of diffusion.

For comparison, sequences of microstructures predicted by Kawasaki dynamics were calculated for $J_1/J_2 = \sqrt{2}$, and the results are shown in Fig. 6.6. Fig. 6.6.(a) indicates that at small concentrations and small particle sizes {10} and {11} facets are approximately equally favoured, which is consistent with their equal interfacial energies with $J_1/J_2 = \sqrt{2}$. Larger particles, however, have a clear ⟨11⟩ alignment. The corresponding simulation with vacancy dynamics, Fig. 6.9.(a), shows similar microstructures. Also at the higher concentration with Kawasaki dynamics, shown in Fig. 6.6.(b), there is a clear tendency for interfaces to align preferentially along ⟨11⟩ directions. Close inspection of Fig. 6.6.(b) reveals that the {11} facets are rougher than the relatively few {10} facets. The energies of atomic steps on {11} and {10} facets are $2|J_2|$ and $2|J_1|$ respectively; with $J_1/J_2 = \sqrt{2}$ a step on a {11} facet has $1/\sqrt{2}$ of the energy a step on a {10} facet. At low temperatures coarsening of the interconnected structure shown in Fig. 6.6.(b) occurs through the creation and propagation of steps. However, since

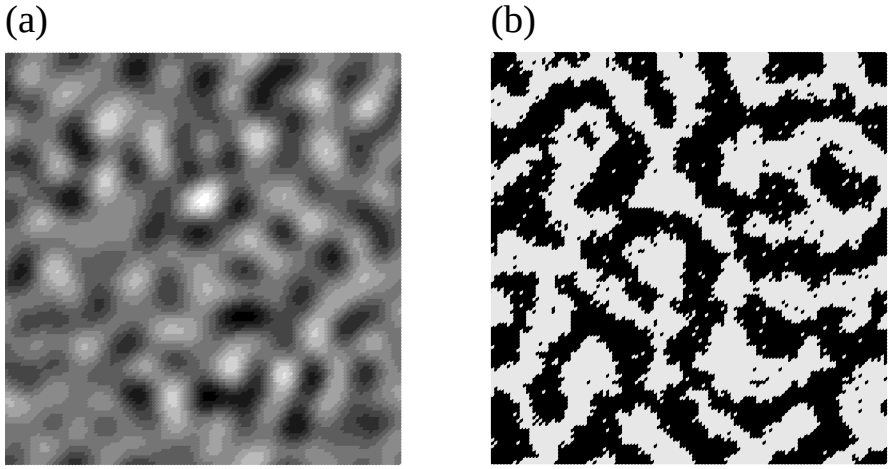


Figure 6.7: Snapshots of evolving microstructures with $c = 0.5$ and $T/T_c = 0.93$: (a) is a mean field (constant mobility) and (b) a Monte Carlo vacancy model result. The simulation times are in (a) $t = 78$ and (b) $t = 30$. The black and white regions in (a) have compositions that differ by only 0.8%.

only nearest neighbour exchanges are allowed, steps along {11} facets move more slowly than along {10} facets. By allowing Kawasaki exchanges only between next nearest neighbour sites it is found that {10} facets predominate in the microstructure. Therefore, in Kawasaki simulations kinetic factors also limit the the mobility of {11} facets, and cause their more frequent appearance in Fig. 6.6.(b).

Fig. 6.7 shows microstructures following a shallow quench to $T/T_c = 0.93$ with $c = 0.50$ (P_4 in Fig. 6.1). The initial choice of interaction parameters is used, i.e. $V_1/V_2 = J_1/J_2 = \sqrt{2}$. Now the vacancy Monte Carlo model (Fig. 6.7.(b)) is characterized by rougher interfaces, and their alignment along particular directions is much weaker than at the lower temperature (Fig. 6.2.(d)). This tendency for rough interfaces is reflected in the corresponding mean field microstructures by compositionally more diffuse interfaces (Fig. 6.7.(a)). Also, isolated $A(B)$ atoms in the $B(A)$ domains in the Monte Carlo model are reflected in the reduction in amplitude of composition modulations in the mean field model. However, this reduction is clearly too great, only ± 0.004 about the average value of 0.50, in the mean field model. The phase composition does not correspond to the equilibrium mean field value, either [3].

[3] See the mean field phase diagram in appendix A.

6.3.2 Coarsening mechanisms

At lower concentrations where solute atoms precipitate as isolated particles, theories predict microstructural coarsening to proceed at higher temperatures through LSW-evaporation and condensation of atoms, and coalescence of diffusing particles at lower temperatures, as discussed in chapter 5. In this section coarsening behaviour at different temperatures between the Monte Carlo and mean field models is compared.

Fig. 6.8 shows the results of a quench to $T/T_c = 0.16$ with $c = 0.15$ (P_3 in Fig. 6.1) for the mean field model. We see small particles with roughly circular shapes, that is maintained throughout coarsening. Some coarsening events are indicated by rectangles in Fig. 6.8, and we can see that smaller particles gradually disappear through evaporation while larger nearby particles grow, and no diffusion of entire particles is observed.

In their recent Monte Carlo study, Fratzl and Penrose showed that at low temperatures with vacancy dynamics entire particles diffuse and eventually coalesce [89]. Our Monte Carlo simulations with vacancy dynamics show similar behaviour. At $T/T_c = 0.16$ it was found that the vacancy spends about 90% of the time at, or in the immediate vicinity of, particle interfaces, and only 10% of the time does it escape into the interior of the A or B phases. The center of mass of a particle moves as the vacancy enters the particle. Occasionally the vacancy escapes

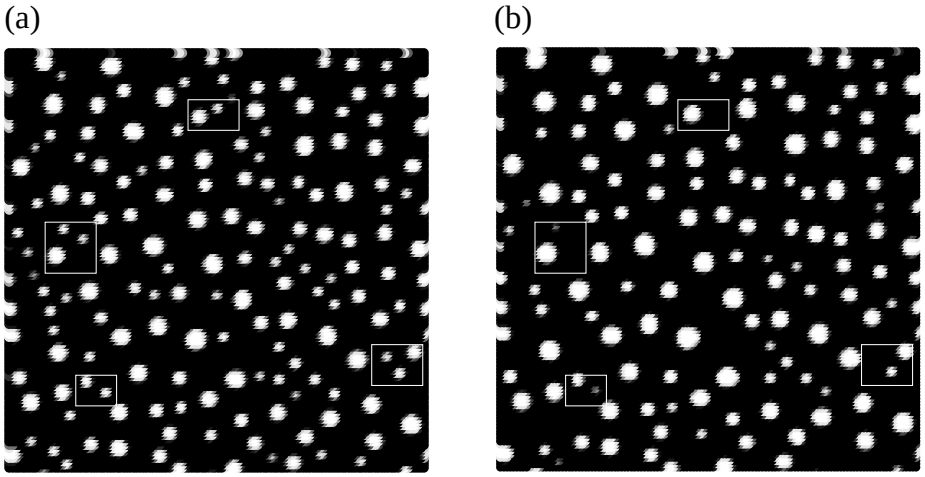


Figure 6.8: Snapshots of evolving microstructures obtained with the mean field model (constant mobility) at $T/T_c = 0.16$ and $c = 0.15$. In (a) $t = 4.0 \times 10^7$ and (b) $t = 4.7 \times 10^7$. Rectangles outline corresponding regions in (a) and (b).

and attaches itself to another particle, which then undergoes Brownian motion. Coarsening is a result of coalescence of these diffusing particles (Fig. 6.9.(a)). The average solute concentration in the matrix is $\sim 1 \times 10^{-3}$. At $T/T_c = 0.50$ (P_2 is Fig. 6.1) Brownian motion is still evident, as seen in Fig. 6.9.(b), but the increased solute concentration in the matrix, $\sim 3 \times 10^3$, indicates that the evaporation and condensation mechanism is also operative. This also reflects the vacancy behaviour: more than 60% of the time the vacancy spends in the A or B phase, and less than 30% at interfaces. Closer to T_c (P_1 in Fig. 6.1) the LSW-mechanism is the dominant process (Fig. 6.9.(c)). Particles are rough and the concentration of solute atoms in the matrix has increased to $\sim 2 \times 10^{-2}$. In this case the vacancy spends over 70% of the time in the interiors of the particles, or in the matrix.

In order to confirm the Brownian motion of entire particles at low temperatures, further Monte Carlo simulations were carried out at $T/T_c = 0.25$. Initially two approximately circular particles consisting of 13 and 113 solute atoms were centred on sites (42,42) and (85,85), shown in Fig. 6.10, and the motions of their centers of mass were followed through the time. Trajectories of the particles, shown in Fig. 6.11.(a), confirm that with vacancy dynamics the particles move in a random fashion. It was also investigated whether Brownian motion of entire particles occurs with Kawasaki dynamics with the same initial distribution of solute. By colouring the atoms of the particles at the beginning of the simulation it was possible to identify very clearly diffusion of solute between the particles. This is shown in Fig. 6.10 in comparison to the vacancy dynamics simulation. Interestingly, the LSW-mechanism was found to dominate over Brownian motion even at low temperatures, in agreement with the results of Ref. [89]. Therefore it is concluded that in two dimensions Brownian motion of particles at low temperatures is a result of the vacancy mechanism of diffusion [4].

The mean field model was applied to the same initial distribution of solute, although the configurational entropy in Eq. (6.2) requires that at least some solute was present at each matrix site, and some host concentration was present in the particles. Therefore the initial distribution of solute is not unique, but in this simulation the overall solute concentration was

[4] In three dimensional Monte Carlo simulations particle coalescence has been observed with vacancy dynamics in Ref. [90] and with Kawasaki dynamics in Ref. [91].

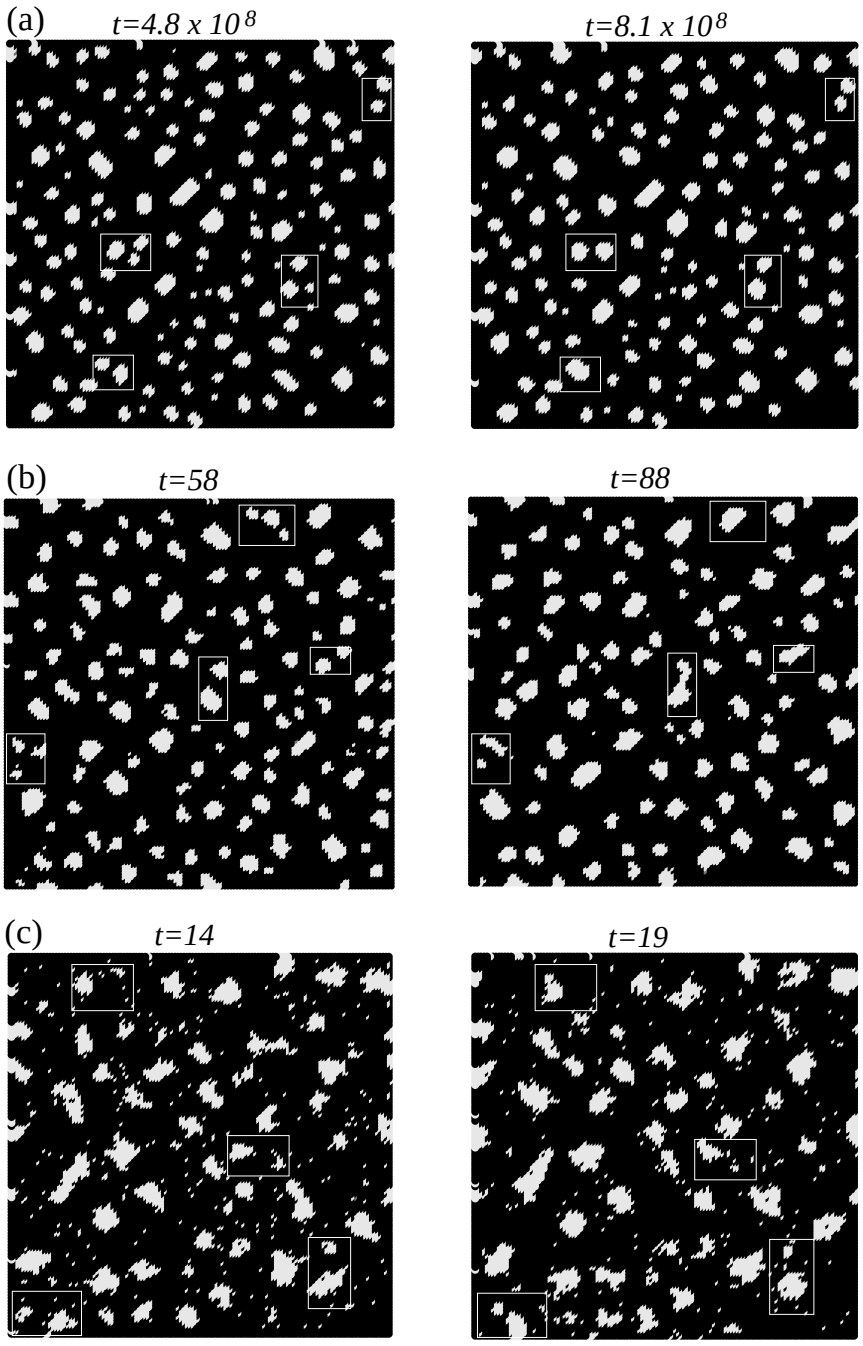


Figure 6.9: Snapshots of evolving microstructures, obtained with the Monte Carlo vacancy model, $c = 0.15$. In (a) $T/T_c = 0.16$, (b) $T/T_c = 0.50$ and (c) $T/T_c = 0.93$. Particle movement and coalescence, and evaporation can be seen by comparing the contents of the outlined rectangles at each temperature.

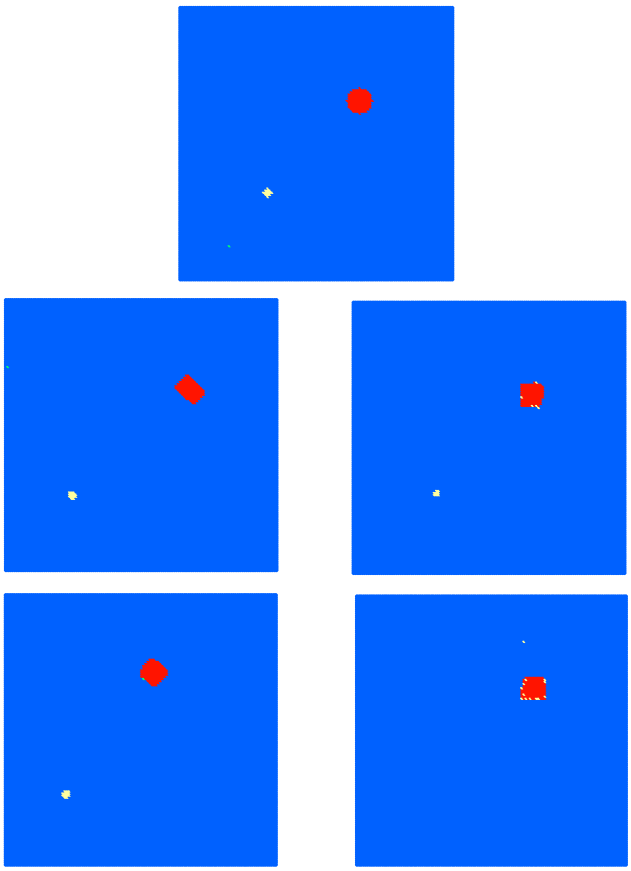


Figure 6.10: Snapshots of evolving microstructures obtained with vacancy and Kawasaki dynamics in Monte Carlo simulations at $T/T_c = 0.25$. In vacancy case the simulation times are $t = 9.7 \times 10^4$ and 6.5×10^5, and in Kawasaki case $t = 5.7 \times 10^4$ and 9.5×10^4 (MCS). Particles are colored so that the atoms belonging initially to each of the particles can later be identified. Vacancy mechanism shows random Brownian motion of particles whereas with Kawasaki dynamics atoms from the smaller particle evaporate and diffuse to the larger particle.

chosen the same as in the corresponding Monte Carlo simulation. The mean field results in Figs. 6.11.(b) and Fig. 6.12 indicate no Brownian motion, and the smaller particle shrinks and the larger particle grows. Changing the temperature did not change this qualitative picture. When the overall solute concentration was increased no evaporation was observed, and both particles grew by absorbing solute atoms from the matrix. If the particles were initially closer together, their centers of mass moved away from each other, since the region between the particles became depleted of solute, and growth could occur only in directions away from their joint center of mass.

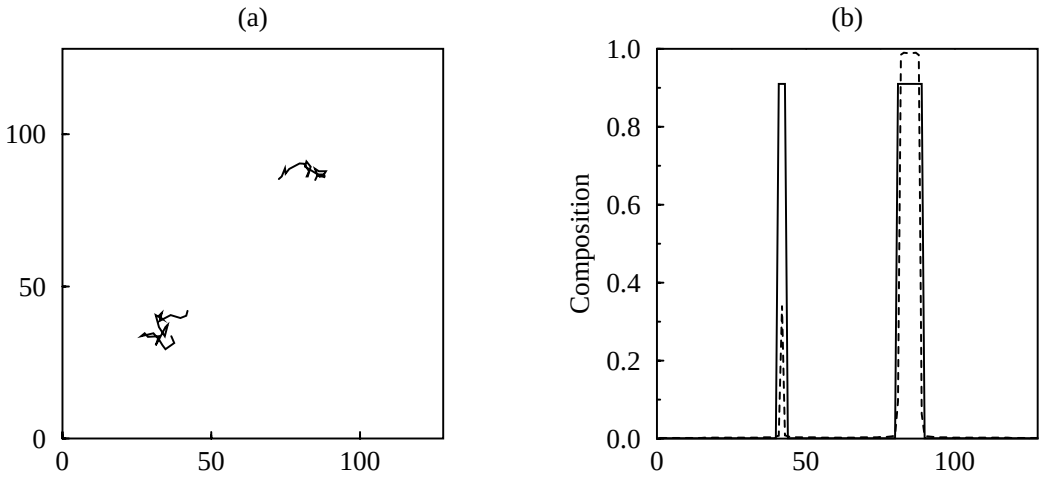


Figure 6.11: Time evolution of two particles at $T/T_c = 0.25$. The slightly higher temperature than in Fig. 6.9.(a) was chosen in order to make the Brownian motion more visible. This temperature was still low enough not to activate the LSW-mechanism. (a) A Monte Carlo vacancy diffusion result: trajectories of the centers of masses of the particles show Brownian motion. (b) A mean field (constant mobility) result: composition profiles through the sample shows the shrinkage of the smaller particle, but no Brownian motion. Solid line shows the initial composition.

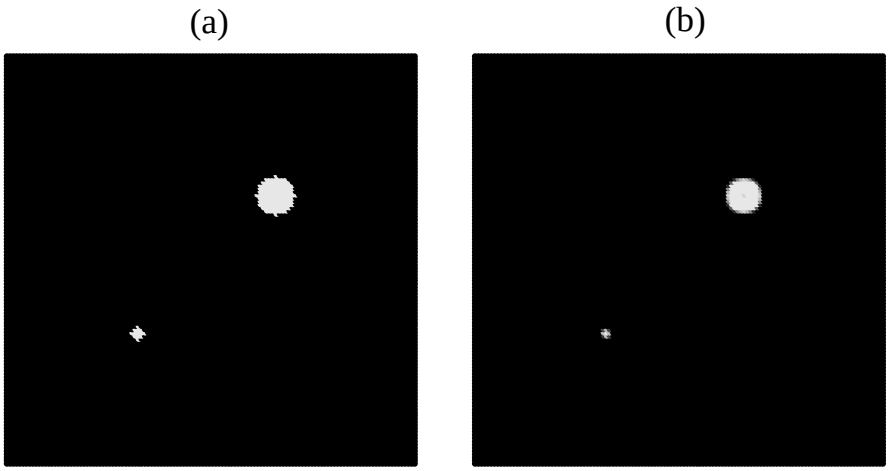


Figure 6.12: Mean field microstructures (constant mobility) of a system with two particles at $T/T_c = 0.25$. In (a) the (reduced) simulation time $t^* = Mt$ is $t^* = 0$ (M is the mobility of Eq. (6.1)), and in (b) $t^* = 0.12$. Snapshots correspond to composition profiles of Fig. 6.11.(b).

The influence of the mobility M in Eq. (6.1) on the mechanism of coarsening was investigated by making it dependent on the local atomic environment. As mentioned in chapter 4, in reality the mobility depends on the local concentration, and therefore the assumption of constant M is doubtful. In section 2.5 it was shown that the mobility in the mean field model has the general form

$$M_{ij} = \nu\sqrt{n_i n_j (1-n_i)(1-n_j)}\exp(-\frac{2E_s^A - E_i^A - E_j^A}{2k_BT})\exp(-\frac{2E_s^B - E_i^B - E_j^B}{2k_BT}) \tag{6.5}$$

where M_{ij} is the mobility for two-way diffusion along the $i-j$ bond, and ν is the attempt frequency for atomic exchanges. The mobility is specified through the saddle point energy. With the choice of saddle point energy for the Monte Carlo model, Eq. (4.2), this becomes

$$\begin{aligned} M_{ij} &= \nu\sqrt{n_i n_j (1-n_i)(1-n_j)}\exp(-\frac{2e_0}{k_BT}) \\ &= C_0\sqrt{n_i n_j (1-n_i)(1-n_j)} \end{aligned} \tag{6.6}$$

where the constant exponential term and the attempt frequency are incorporated in the constant C_0. Thus the environment dependence of the mobility in the mean field model appears *only* [5] in the pre-exponential geometric mean factor $\sqrt{n_i(1-n_i)n_j(1-n_j)}$, which is maximized when $n_i = n_j = 0.5$, and is minimized when n_i or n_j is 0 or 1. This environment dependent mobility was used in Eq. (6.1) to model [6] a system with $c = 0.15$ at $T/T_c = 0.16$, the morphologies of which with constant mobility are depicted in Fig. 6.8. Although with the environment dependent mobility the kinetics were affected, the mechanism of coarsening remained the same as for the system with constant mobility, shown in Fig. 6.8. At low concentrations the coarsening proceeded through LSW-evaporation, but increasing the concentration to $c = 0.35$ produced some coalescence events of two nearby particles by forming a "bridge" of solute between them (Fig. 6.13). There were, however, no qualitative differences between the results with constant and environment dependent mobility in this respect. The bridging mechanism was first pro-

[5] Note that this differs from the mobility obtained by Martin [17]. He assumes that the saddle point energy is fixed, and in that case the environment dependency remains also in the exponential of Eq. (6.5).

[6] It was now necessary to solve Eq. (6.1) entirely in real space without using the Fourier transform technique described in section 3.5.

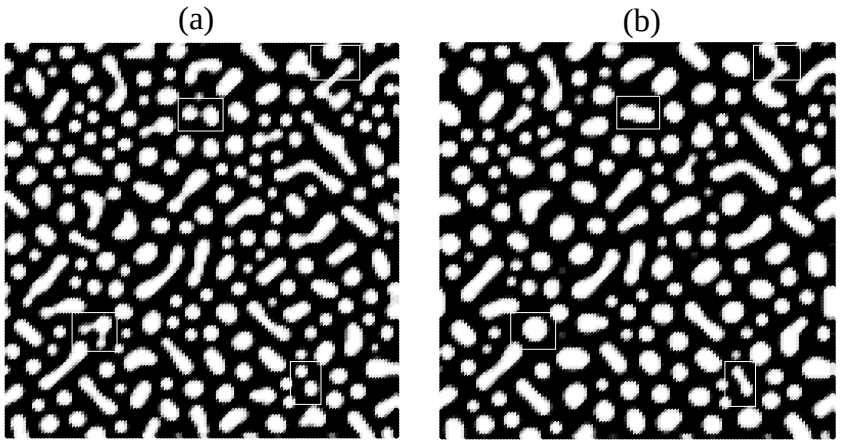


Figure 6.13: Snapshots of microstructures obtained with mean field model with environment dependent mobility, $c = 0.35$ and $T/T_c = 0.16$. The rectangles indicate some bridging events. In (a) the (reduced) simulation time is $t^* = 60$, and in (b) $t^* = 93$.

posed by Tanaka [93] for systems of high particle density, where the diffusion fluxes around the particles couple. In Refs. [18, 94] bridging was observed as a dominant mechanism at early stages of coarsening in mean field simulations, before the LSW-mechanism takes over.

Finally, Fig. 6.14 shows snapshots of vacancy Monte Carlo simulations ($J_1/J_2 = \sqrt{2}$) with $c = 0.50$. At $T/T_c = 0.16$ (Fig. 6.14.(a)) diffusion along interfaces is the dominant mechanism. In that case the vacancy spends about 90% of the time at the interface, and only 10% in the A or B phase. The solute level in the matrix is negligible. Coarsening events indicated by the rectangles in Fig. 6.14.(a) clearly demonstrate the effect of kinetics on structure morphologies and formation of {11} facets, as discussed in section 6.3.1. At $T/T_c = 0.50$ (Fig. 6.14.(b)) the vacancy occasionally escapes to the A or B phase, and some solute atoms in matrix indicate that the evaporation and condensation mechanism is activated. In this case the vacancy resides in either A or B phase 50% of the time, and now the matrix solute concentration is $\sim 2 \times 10^{-3}$. In Fig. 6.14.(c) the evaporation is the dominant coarsening mechanism. The vacancy spends over 60% of its time in either A or B phase, and less than 30% at (the vicinity of) interfaces. In this case the solute concentration in the matrix is $\sim 2.5 \times 10^{-2}$.

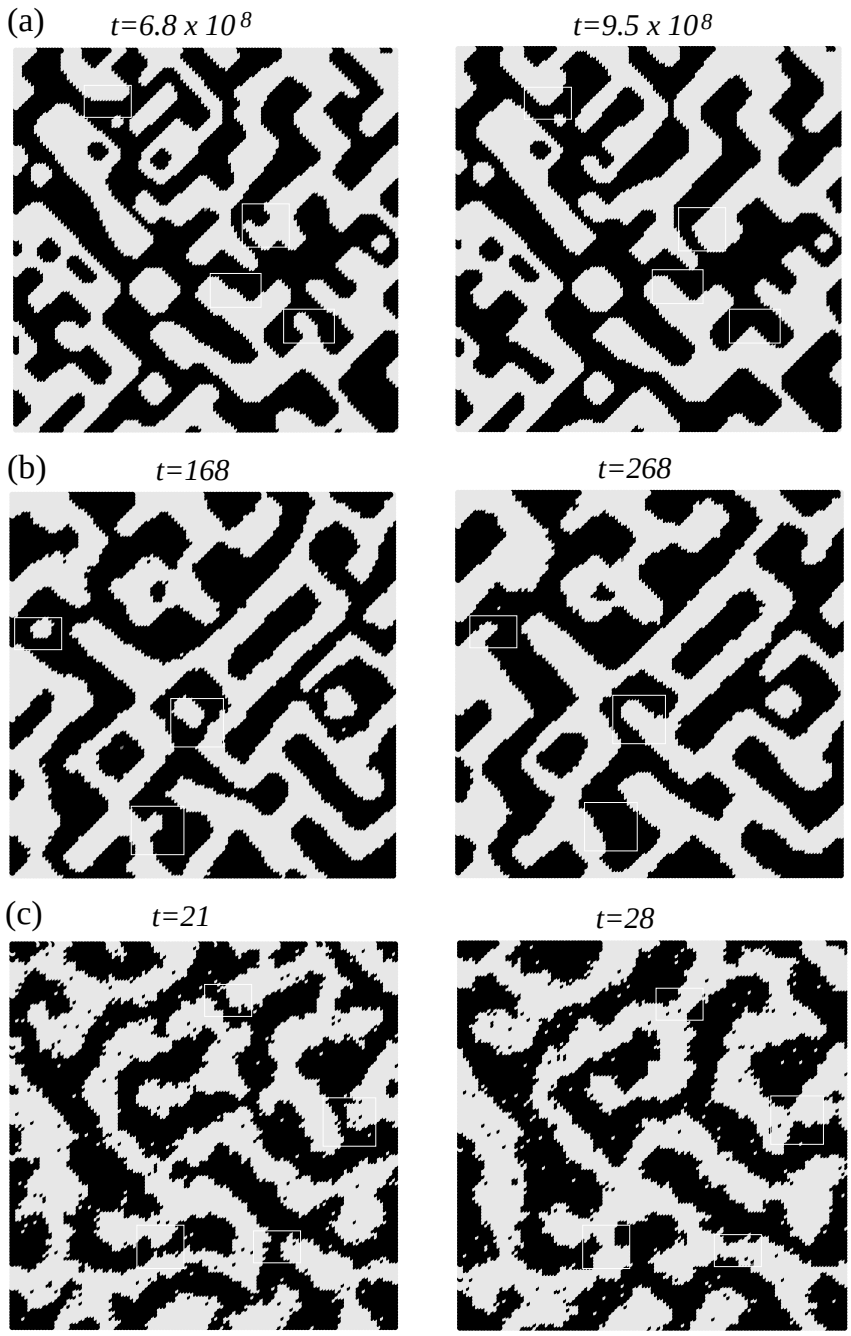


Figure 6.14: Snapshots of evolving microstructures obtained with the Monte Carlo vacancy model, $c = 0.50$. In (a) $T/T_c = 0.16$, (b) $T/T_c = 0.50$ and (c) $T/T_c = 0.93$. Some coarsening events can be seen by comparing the contents of the outlined rectangles at each temperature.

6.3.3 Kinetics

In this section the coarsening kinetics and the validity of the asymptotic LSW-$t^{1/3}$ behaviour for the mean field and Monte Carlo models are discussed. The average domain size was monitored using the spatial autocorrelation function

$$G(\mathbf{r},t) = \frac{1}{N_s}\sum_i [\sigma(\mathbf{r}_i,t)-\bar{\sigma}][\sigma(\mathbf{r}_i+\mathbf{r},t)-\bar{\sigma}], \tag{6.7}$$

and its Fourier transform, the two-dimensional structure function

$$S(\mathbf{k},t) = \frac{1}{N_s}|\sum_i (\sigma(\mathbf{r}_i,t)-\bar{\sigma})\exp(i\mathbf{k}\cdot\mathbf{r}_i)|^2 \tag{6.8}$$

where $\mathbf{r}$ and $\mathbf{r}_i$ run over the $N_s = L\times L$ lattice sites, $k_\alpha = \frac{2\pi}{L}p_\alpha$, $p_\alpha = 0, \pm 1, ..., \pm L/2$ ($\alpha = x, y$) is a wave vector in the first Brillouin zone, and $\bar{\sigma}$ is the average value of the site occupancies $\sigma(\mathbf{r}_i)$. Ensemble averaged values of $G(\mathbf{r},t)$ and $S(\mathbf{k},t)$ were obtained over several (in most cases five) independent Monte Carlo runs. A circularly averaged autocorrelation function may be defined as

$$g(r,t) = \frac{1}{N_r}\sum_{|\mathbf{x}|=r} G(\mathbf{x},t) \tag{6.9}$$

and a circularly averaged structure function as

$$s(k,t) = \frac{1}{N_k}\sum_{|\mathbf{x}|=k} S(\mathbf{x},t) \tag{6.10}$$

where N_r and N_k are the numbers of atomic sites and k-points contributing to each sum. The structure function $s(k,t)$ shows a peak at a finite wave number $k_m(t)$, the position of which decreases with time. However, the position of this maximum is not well defined owing to the discrete distribution of k-points. A more reliable measure of the inverse of the typical length scale in microstructure is the first moment of the structure function:

$$k_1(t) = \frac{\sum_k k s(k,t)}{\sum_k s(k,t)}. \tag{6.11}$$

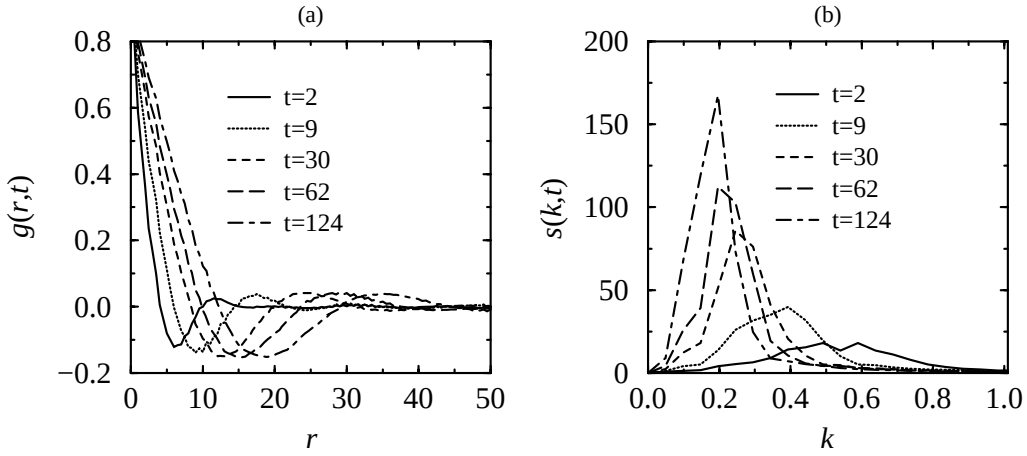


Figure 6.15: (a) Circularly averaged autocorrelation functions for the Monte Carlo vacancy diffusion model with $c = 0.50$ and $T/T_c = 0.93$ at five times, t. (b) Circularly averaged structure functions for the same system as in (a). With increasing time the peak position for the characteristic wavelength in the system moves towards smaller k values, i.e. larger wavelengths.

The circularly averaged autocorrelation and structure functions obtained for five Monte Carlo vacancy dynamics runs for the case $c = 0.50$ and $T/T_c = 0.93$ are shown in Fig. 6.15. The autocorrelation functions are scaled such that $g(0,t) = 1$ always. The increase of the average domain size, as determined by the position, $R(t)$, of the first zero of $g(r,t)$ and by the inverse, $1/k_1$, of the first moment of $s(k,t)$, is shown in Fig. 6.16. The variations of $R(t)$ and $1/k_1(t)$ with t are very similar. For comparison, the dashed line has a slope of 1/3. At very late stages of the high temperature $T/T_c = 0.93$ simulations the effective exponents [7] $n_{eff}(t) = d[\ln(1/k_1(t))]/d[\ln t]$ are 0.33 ± 0.02 with $c = 0.15$ and 0.34 ± 0.02 with $c = 0.50$. Also, for the $c = 0.50$ cases at $T/T_c = 0.16$ and $T/T_c = 0.50$, the effective exponents are close to the theoretical LSW-value, being 0.33 ± 0.03 in both cases. For $c = 0.15$ at $T/T_c = 0.16$ and $T/T_c = 0.50$ the late time exponents are well below 1/3, at 0.07 ± 0.005 and 0.24 ± 0.01, respectively.

For low temperature cluster growth in two dimensions the Binder-Stauffer phenomenological

[7] It has to be remembered that all growth law exponents in this study should be interpreted only as approximate, since neither the number of runs, nor the system sizes used, are large enough to allow accurate statistics. A 68% confidence interval is used in estimating errors in late time exponents.

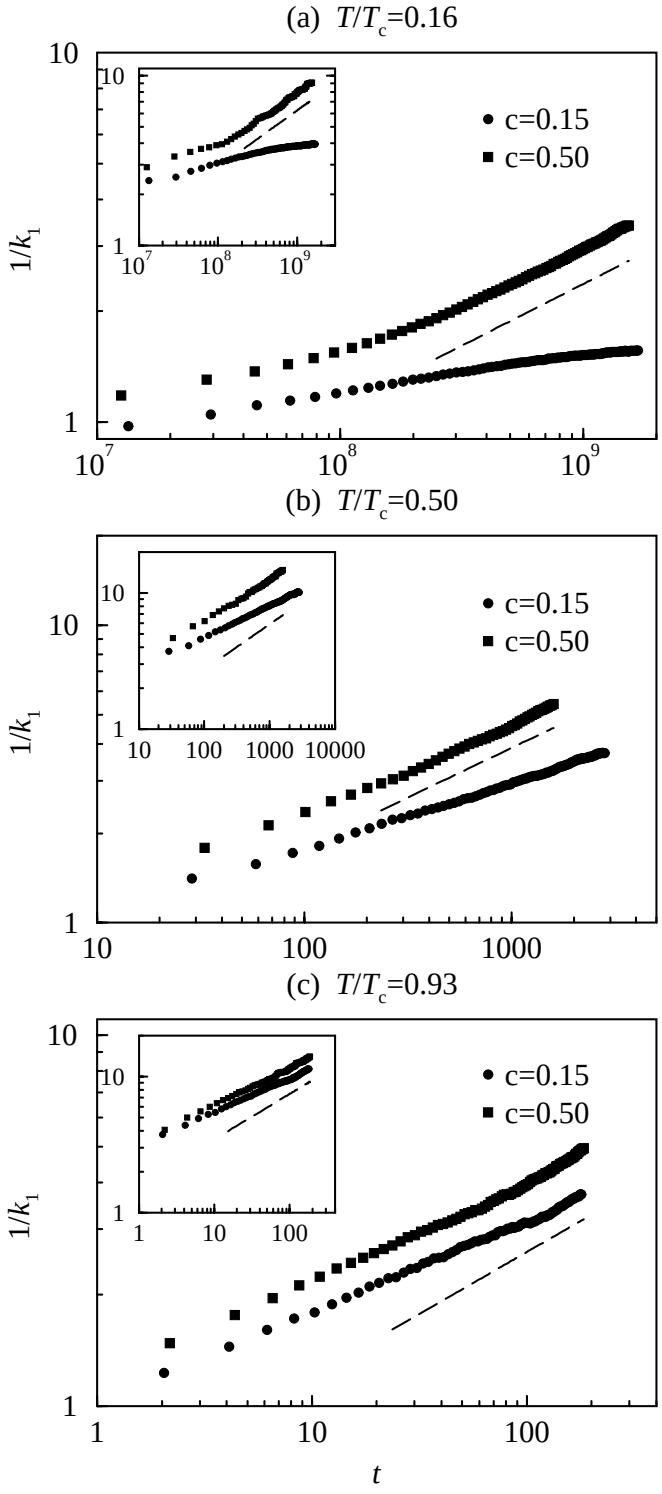


Figure 6.16: Average domain sizes $1/k_1$ as function of time from Monte Carlo vacancy diffusion simulations. The insets show the corresponding average domain size, $R(t)$, behaviour. For comparison, the dashed line has a slope of 1/3.

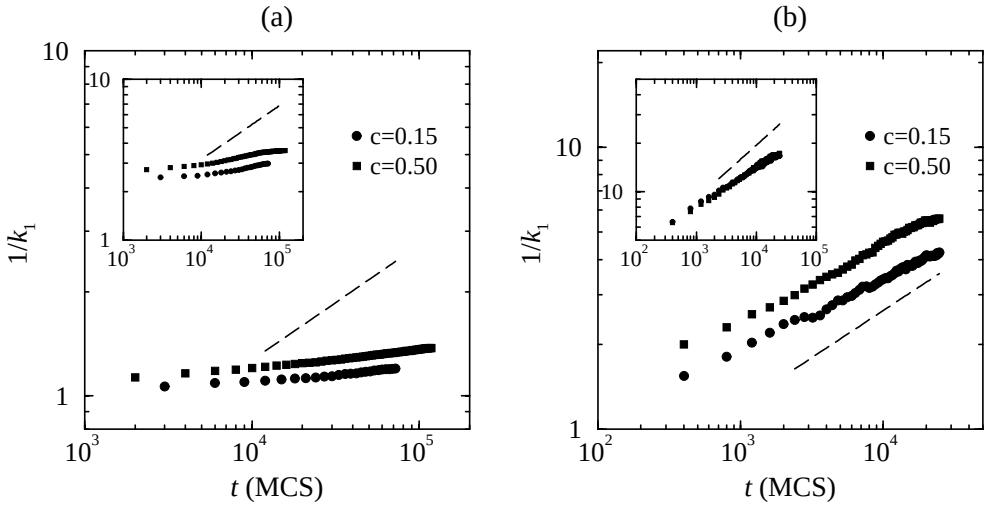


Figure 6.17: Average domain sizes $1/k_1$ as function of time from Monte Carlo Kawasaki dynamics simulations. In (a) $T/T_c = 0.16$ and (b) $T/T_c = 0.93$. The insets show the corresponding average domain size, $R(t)$, behaviour. For comparison, the dashed line has a slope of 1/3.

theory predicts an exponent of 1/5 [85]. This is higher than indicated by our Monte Carlo vacancy model results with $c = 0.15$ obtained at low temperature, $T/T_c = 0.16$. In BS-theory coarsening results from particle diffusion and coalescence, which is effected by atomic diffusion at particle surfaces. In our system, interfacial atomic diffusion slows down, as more interfaces align along the relatively immobile $\langle 11 \rangle$ directions. Vacancy migration parallel to $\{11\}$ interfaces involves jumps out of the interface along $\langle 10 \rangle$ directions costing $4|J_1|$ of energy. For the vacancy to escape altogether from a $\{11\}$ interface an energy $2|2J_1 + J_2|$ must be supplied. These are the reasons for the decreasing effective exponent in Fig. 6.16.(a). At the intermediate temperature of $T/T_c = 0.50$ (Fig. 6.16.(b)) however, the exponent is close to the BS-value. At this higher temperature there is sufficient thermal activation to drive interfacial diffusion and vacancy escape from the interface.

The increase of the average domain size as a function of time for Monte Carlo Kawasaki simulations are shown in Fig. 6.17. At $T/T_c = 0.16$ (Fig. 6.17.(a)) the growth occurs much more slowly than in the corresponding vacancy dynamics simulation, Fig. 6.16.(a). At composition $c = 0.50$ the curve does not exhibit a strongly increasing effective exponent $n_{eff}(t)$, which was seen with the vacancy model, but the growth behaviour is very similar at both compositions

$c = 0.15$ and $c = 0.50$. However, the upward bending of the growth curve in Fig. 6.16.(a) begins at domain sizes larger than reached by the Kawasaki simulation in Fig. 6.17.(a). The late time effective exponents are 0.05 ± 0.005 for $c = 0.15$ and 0.06 ± 0.001 for $c = 0.50$, which are less than observed in any of the vacancy dynamics simulations. At low temperature Kawasaki simulations (Fig. 6.17.(a)) the rejection rate is very high, and simulation times required to achieve comparable domain sizes with vacancy dynamics model are not sensible. Therefore the exponents are not fully comparable to the vacancy Monte Carlo simulations. This also demonstrates the inefficiency of Kawasaki dynamics at low temperatures; there is hardly any increase in average domain size of the microstructure even over two orders of magnitude of (Monte Carlo) time.

At high temperature $T/T_c = 0.93$ (Fig. 6.17.(b)), with $c = 0.50$ the Kawasaki coarsening kinetics are similar to the vacancy dynamics behaviour of Fig. 6.16.(c). At the beginning there is a slight tendency for upward curvature, the slope of which at later times is 0.27 ± 0.01. At very late times and large domain sizes, however, the effective exponent is slightly decreasing. This occurs at domain sizes, which are not reached by vacancy Monte Carlo simulations of the same system, and therefore exact comparisons about very late time kinetics between Kawasaki and vacancy dynamics cannot be made. With $c = 0.15$ the trends of the kinetics resemble the corresponding vacancy dynamics results, and the effective late time exponent is 0.25 ± 0.02.

Figs. 6.18.(a) and (c) show the time evolution of $1/k_1(t)$ for the mean field model with constant mobility and Fig. 6.18.(b) and (d) with environment dependent mobility with different compositions and temperatures. At $T/T_c = 0.93$ and $c = 0.15$ the alloy is in the single phase region of the mean field phase diagram. With constant mobility, the slope clearly decreases with time at $T/T_c = 0.93$ and $c = 0.50$ (Fig. 6.18.(c)), in contrast to the Monte Carlo simulations and theoretical predictions. On the contrary, with environment dependent mobility, the slope increases after an incubation period to value ~ 0.50, which clearly exceeds the theoretical LSW-prediction (Fig. 6.18.(d)). Whereas at $T/T_c = 0.93$ with constant mobility the coarsening ceases at late times, the mean field model with environment dependent mobility has no difficulties - after the incubation period - in reaching longer wavelengths. Also, considerably greater amplitudes of concentration modulations were obtained with environment dependent mobility:

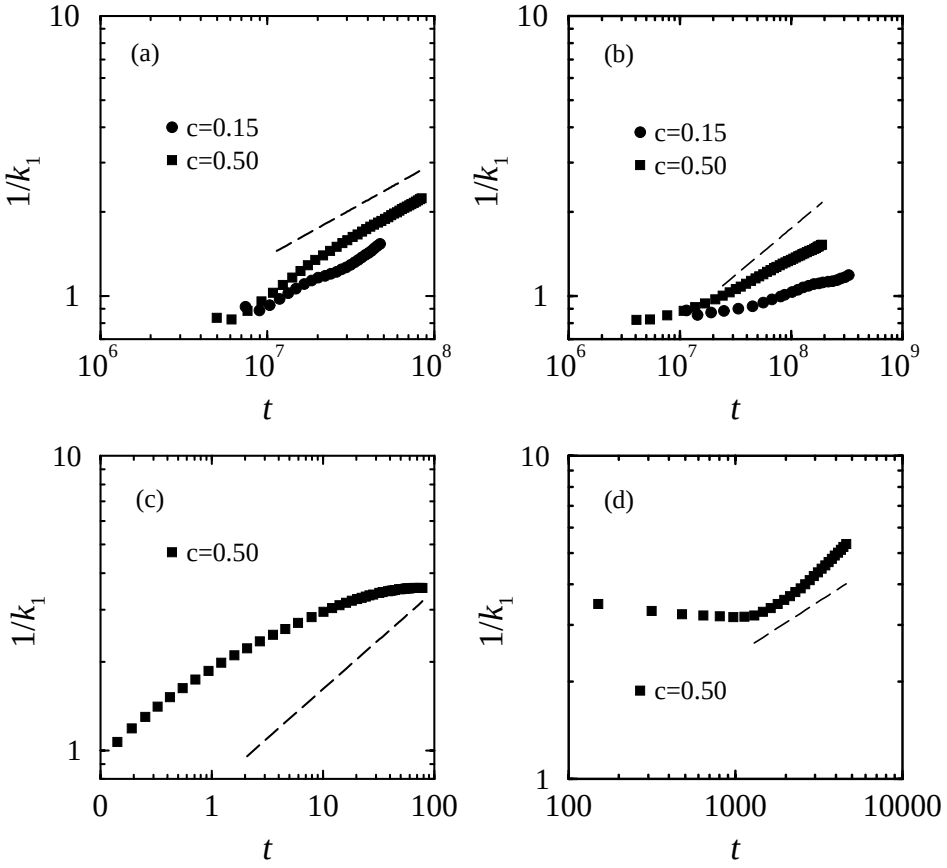


Figure 6.18: Average domain sizes $1/k_1$ vs. time from microscopic mean field models: (a) constant mobility, $T/T_c = 0.16$, (b) environment dependent mobility, $T/T_c = 0.16$, (c) constant mobility, $T/T_c = 0.93$, (d) environment dependent mobility, $T/T_c = 0.93$. For comparison, the dashed line has a slope of 1/3.

± 0.21 about the average value of 0.50 compared to ± 0.004 with the mean field model with constant mobility. The phase composition obtained with the environment dependent mobility is in agreement with the mean field phase diagram in appendix A. At $T/T_c = 0.16$ and $c = 0.50$ with constant mobility (Fig. 6.18.(a)), the late time effective exponent is ~ 0.33, but for $c = 0.15$ it is significantly greater than in the corresponding Monte Carlo case and the LSW-value, at ~ 0.40. With environment dependent mobility (Fig.6.18.(b)), at late times the low temperature growth exponents for both compositions are below 1/3, at ~ 0.11 with $c = 0.15$ and at ~ 0.20 with $c = 0.50$.

Fig. 6.16 shows that in the Monte Carlo model with vacancy dynamics model raising the temperature from $T/T_c = 0.16$ to $T/T_c = 0.93$ results in a dramatic change of time scale,

which is determined by the attempt frequency ν and the activation energy E_a. With Kawasaki dynamics time is defined through the number of attempts to exchange a pair of nearby atoms. In the mean field model the time scale is determined by the atomic mobility M. Since the mean field model with constant mobility has no intrinsic information about attempt frequencies or activation energy barriers, the time scales between the vacancy Monte Carlo model and the mean field model with constant mobility were made comparable by choosing $M = 1/\tau$, where τ is the average mean residence time of Eq. (4.6). For the mean field model with environment dependent mobility, time was scaled such that the average mobility $M = C_0 c(1-c) = 1/\tau$, where c is the average composition of the alloy. As can be seen in Fig. 6.18, this does not give fully comparable time scales between the mean field models.

Finally, the observation of Ref. [95] was confirmed that the initial kinetics are sensitive to the choice of initial conditions: the wider the distribution of site occupancies at the beginning, the easier it is to form nuclei that can grow, and the incubation period becomes shorter. However, initial conditions are expected to have no effect on late time kinetics [95].

6.3.4 Physicality of time scales in the models

The time scale in a microscopic mean field model is defined through the mobility. Whether a physically meaningful time scale for a microscopic mean field model may be defined depends on the extent to which its mobility describes the temperature and environment dependences of the real mechanism of diffusion, which in metallic alloys is usually vacancy hopping.

In the mean field approach we work with occupation probabilities of atomic sites. Diffusion in a mean field description is a process in which the occupation probability of a site becomes more, say, A-like by transfer of the A-character along the bonds between nearby sites. This flux is compensated by a transfer of B-character of the site in the reverse direction along the same bonds. Thus, each bond is a path for two-way diffusion of A and B character. This two-way diffusion is reflected in the mobility in the mean field model, given in Eq. (6.5), where two exponential factors appear, one for diffusion of A atoms along the bond and the other for the diffusion of B atoms. The activation energy appearing in the $A(B)$ exponential factor is the average activation energy for an $A(B)$ atom to jump in either direction along the bond.

For the physically reasonable choice of saddle point energy given by Eq. (4.2), the average activation energy becomes independent of the local environment, and the product of the two exponential factors becomes the constant form $\exp(-2e_0/k_BT)$ in Eq. (6.6). For diffusion by a vacancy mechanism the mobility along the $i-j$ bond contains a factor that plays a similar role to the geometric mean factor in the mean field model: $(\sigma_i^2 - \sigma_j^2)^2$, which is non-zero only if site i is vacant and site j is occupied by an A or B atom, or vice versa. But the mobility in the vacancy model also contains an exponential factor that is dependent on the local atomic environment: $\exp(-E_a^i/k_BT)$ where $E_a^i = E_s^i - E_1^i$, and the saddle point energy, E_s^i, is given by Eq. (4.2). The key point is that in Eq. (4.2) the activation energy for vacancy diffusion varies linearly with $E_2^i - E_1^i$, the difference in the energy of the system before and after the vacancy has jumped. This dependence of the activation energy on the local environment is absent in the microscopic mean field model, even when the local environment dependence of the saddle point energy is explicitly taken into account, as in Eqs. (6.5) and (4.2). It becomes important, for example, when it results in the trapping of the vacancy at interfaces, because this can lead to an altogether different mechanism of coarsening, namely Brownian motion and coalescence of particles. But if one is dealing with diffuse interfaces, or small concentration gradients, then $E_2^i - E_1^i \to 0$, and the exponential factor in the mobility in the vacancy model becomes $\exp(-e_0/k_BT)$ as compared [8] with $\exp(-2e_0/k_BT)$ in the microscopic mean field model. As noted in section 4.3, e_0 should should depend on the local, coarse-grained composition, and in this way one can recover the composition dependence of the activation energy for diffusion in solid solutions.

In two dimensional Monte Carlo models with Kawasaki dynamics it was observed that LSW-evaporation is favoured over Brownian motion of particles, whereas the vacancy dynamics model results in a variety of coarsening mechanisms over a range of temperatures. Therefore Kawasaki dynamics simulations are not capable of capturing changes in intrinsic time scales which arise from changes in relative importances of different coarsening mechanisms during the microstructural evolution. In this light the linearity between the Monte Carlo time in Kawasaki simulation and the real physical time may be doubted.

[8] If vacancy-atom interactions are taken into account this also becomes $\exp(-2e_0/k_BT)$.

6.3.5 Dynamical scaling in Monte Carlo models

For phase-separating systems it has been observed both experimentally and in computer simulations [96–98] that for long times the circularly averaged autocorrelation function scales as $g(r,t) \sim G_0(r/R(t))$ and the two-dimensional structure function as $s(k,t) \sim k_1^{-2}(t) S_0(k/k_1(t))$, where G_0 and S_0 are time-independent functions. The existence of scaling implies that the rescaled microstructures of the system are statistically equivalent at different times.

Dynamic scaling was tested for the vacancy Monte Carlo model with $c = 0.50$ and $c = 0.15$ at $T/T_c = 0.16$, and the results are shown in Fig. 6.19. With $c = 0.50$ there are clear shifts in the autocorrelation curves both in first minimum location and depth at all times (Fig. 6.19.(a)), and also the structure function peak heights and positions (Fig. 6.19.(b)) are scattered. This reflects the constantly increasing effective exponent seen in Fig. 6.16.(a): coarsening cannot be described as a simple power law, which indicates that the relative importance of different coarsening mechanism, and consequently the statistical properties of the microstructures, may

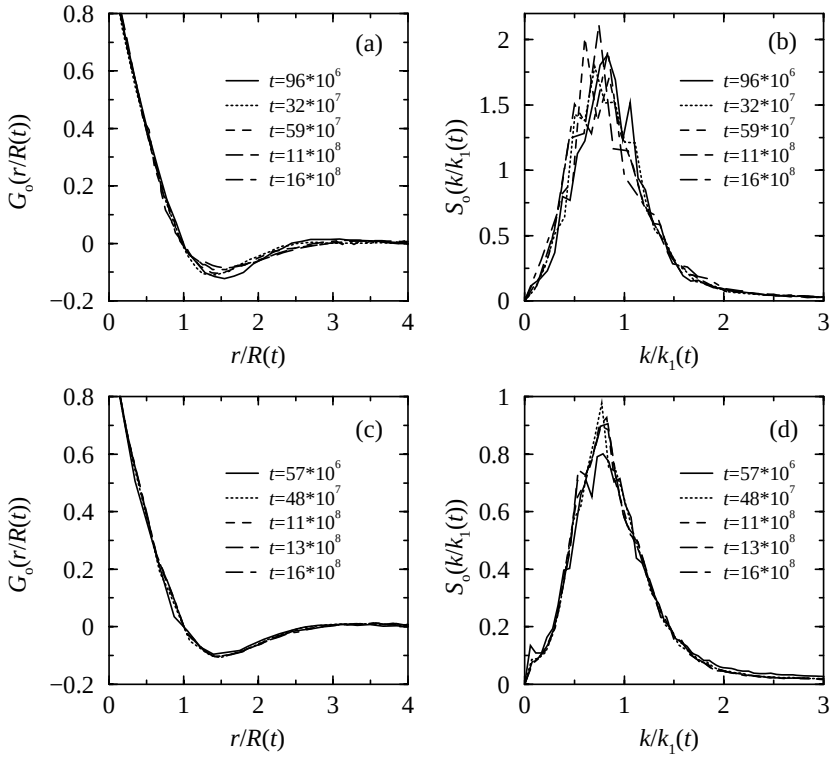


Figure 6.19: Scaled structure and autocorrelation functions at $T/T_c = 0.16$ for the vacancy Monte Carlo model. In (a) and (b) $c = 0.50$, and in (c) and (d) $c = 0.15$.

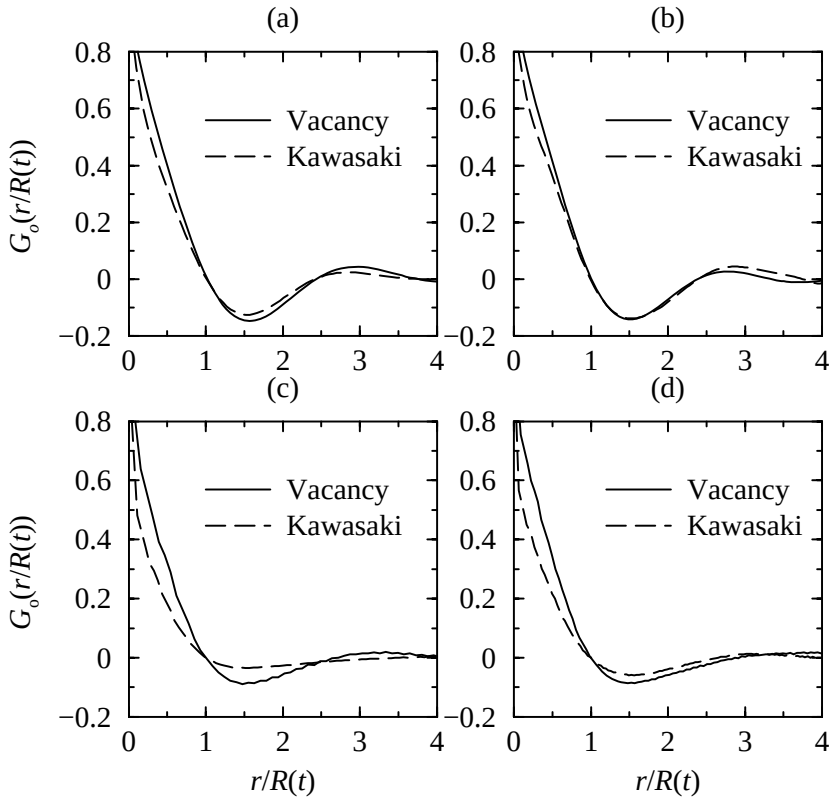


Figure 6.20: Scaled autocorrelation functions for Kawasaki and vacancy dynamics Monte Carlo models at $T/T_c = 0.93$. In (a) $c = 0.50$, $R(t) \approx 10$, (b) $c = 0.50$, $R(t) \approx 14$, (c) $c = 0.15$, $R(t) \approx 8$, (d) $c = 0.15$, $R(t) \approx 13$. The curves show the same first zero crossing, from which the average particle size was determined.

vary during the evolution of the microstructure.

With lower concentration $c = 0.15$ the autocorrelation scaling functions seem to collapse on top of each other (Fig. 6.19.(c)). However, the scarcity of lattice points in the real space autocorrelation function does not enable very accurate comparisons to be made at low concentrations. Slight differences can be seen in the scaled structure functions (Fig. 6.19.(c)) at early times and small domain sizes. The effective coarsening exponent in this case changes slowly compared to the $c = 0.50$ low temperature behaviour, and therefore some scaling is observed. Unfortunately, the simulation times in this study were not adequate to reveal the full effect of the formation of relatively immobile $\{11\}$ facets on the scaling behaviour, which was identified as a reason for the slowly decreasing effective exponent at late times.

It has been generally assumed that microstructures obtained with Monte Carlo models

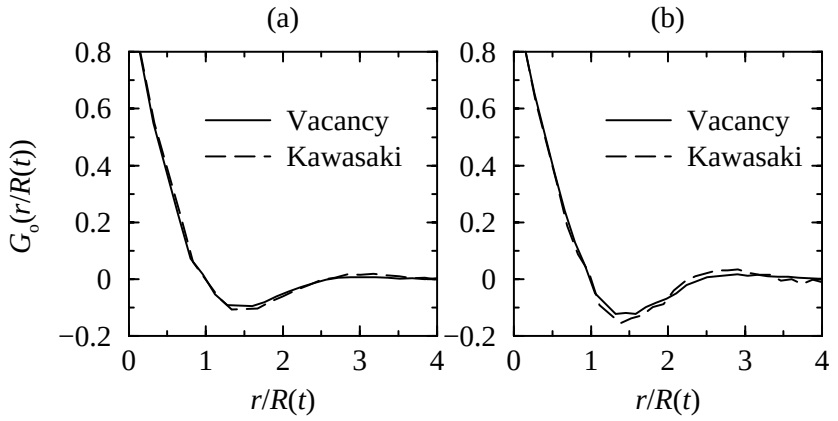


Figure 6.21: Scaled autocorrelation functions for Kawasaki and vacancy dynamics Monte Carlo models at $T/T_c = 0.16$. In (a) $c = 0.15$, $R(t) \approx 3$, (b) $c = 0.50$, $R(t) \approx 3.6$.

are not affected by the choice between Kawasaki and vacancy dynamics. This assumption was tested by comparing the scaled autocorrelation functions G_0 for microstructures with the same average domain size, $R(t)$, obtained with vacancy and Kawasaki dynamics Monte Carlo simulations, the results of which are shown in Figs. 6.20 and 6.21.

At high temperatures, Fig. 6.20, there are clear differences between the autocorrelation functions. With $c = 0.50$ (Fig. 6.20.(a)) the location and depth of the first minima and maxima differ at early stages but at later times and larger domain sizes (Fig. 6.20.(b)) the collapse of the curves improves, and the first minima overlap. With $c = 0.15$ the discrepancies between the scaling functions are more clear, as seen in Figs. 6.20.(c) and (d). The first minimum with vacancy dynamics is clearly deeper than with Kawasaki dynamics, and in all cases the Kawasaki curves drop faster at small values of $r/R(t)$. These indicate larger solute concentration in the matrix, i.e. larger tendency for evaporation with Kawasaki dynamics.

The scaled autocorrelation functions at low temperature $T/T_c = 0.16$ are shown in Fig. 6.21. In this case only one time and domain size was chosen for comparison, since the microstructural coarsening with Kawasaki dynamics was so slow that practically no differences between the Kawasaki scaling functions at different times could be seen. With $c = 0.15$ (Fig. 6.21.(a)) the overlap between the scaled curves is almost perfect, but with $c = 0.50$ (Fig. 6.21.(b)) there are some differences in locations of the first minima and maxima. Again, it has to be recalled

that with small concentrations and average domain sizes the accuracy of scaled autocorrelation functions is rather poor due to very few lattice points contributing to the curve.

These comparisons between scaled autocorrelation functions clearly show that the choice of dynamics affects also the morphologies of the microstructure: they are not necessarily found to be statistically equivalent between the two dynamics. This can also be seen as rougher microstructures with Kawasaki dynamics in some of the snapshots shown in section 6.3.1.

6.4 Simultaneous ordering and phase separation

In this section precipitation of ordered particles from a disordered matrix and subsequent coarsening of the ordered domains are examined. The interaction parameters for the mean field model were chosen as $V_1 = 1$, $V_2 = -0.8$ and $V_3 = -0.55$, and for the Monte Carlo model as $J_1 = 1$ and $J_2 = -0.5$. The correspondence of the parameters between the models is not exact, but they were selected partly because of the availability of phase diagrams. Therefore only qualitative comparisons between mean field and Monte Carlo models are made. With these choices of parameters the critical temperature for ordering in the Monte Carlo model is $k_B T_c \approx 3.8 J_1$, and the tricritical temperature is $k_B T \approx 1.3 J_1$. For the mean field model $k_B T_c^{MF} = 0.25 |\tilde{V}_{\mathbf{k}=\mathbf{k}_0}|$ and $k_B T_t^{MF} \approx 0.19 |\tilde{V}_{\mathbf{k}=\mathbf{k}_0}|$, where $\tilde{V}_{\mathbf{k}=0}$ is the Fourier transform of interaction parameter V at $\mathbf{k}_0 = \frac{2\pi}{L}(\frac{1}{2}, \frac{1}{2})$, the reciprocal lattice vector corresponding to the ordered structure. A schematic equilibrium phase diagram for a system undergoing phase separation and ordering is shown in Fig. 6.22. An exact phase diagram for the mean field model can be found for example in Ref. [41], and an approximate phase diagram for the Monte Carlo model in Ref. [99].

Note that the choice of interaction parameters for the Monte Carlo model would cause a Fourier transform of V at $\mathbf{k} = 0$, $\tilde{V}_{\mathbf{k}=0}$, to be greater than zero, and would yield ordering without phase separation in the mean field model. Also, incorporation of third nearest neighbour interactions into the Monte Carlo model would have increased the computing time considerably. Computing time for the mean field model, however, is not affected by the range of interactions, if the calculations are carried out in reciprocal space, as in this study. Only the constant

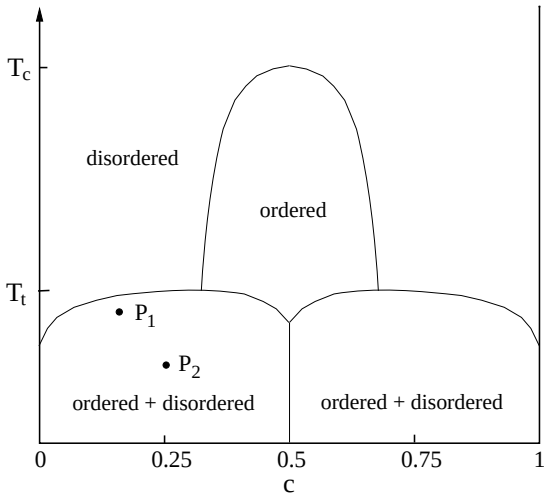


Figure 6.22: Schematic equilibrium phase diagram for a model system undergoing phase separation and ordering. Points P_1 and P_2 within the miscibility gap indicate some quenches discussed in the text.

mobility case in the mean field model was employed in this section.

6.4.1 Morphologies

Fig. 6.23.(a) shows microstructures obtained with the mean model at $c = 0.25$ and $T/T_t = 0.56$ (approximately point P_2 in Fig. 6.22). This particular system was studied in detail in Ref. [41], but the main qualitative features are repeated here for comparisons to be made with the Monte Carlo model.

At the beginning the system undergoes uniform ordering, and the resulting non-stoichiometric ordered phases are separated by antiphase boundaries. During this initial ordering there are no compositional changes in the system. The rapid uniform ordering is later followed by decomposition, which occurs predominantly at antiphase boundaries. The composition of ordered regions changes towards its equilibrium value, while antiphase boundaries are replaced by disordered solute layers.

For comparison, Fig. 6.23.(b) demonstrates the effect of elastic interactions on the morphology of the same system. The early stages are very similar to the case without elastic interactions: uniform ordering occurs throughout the system. Since the system is still compositionally homogeneous, elastic interactions, which arise due to compositional differences

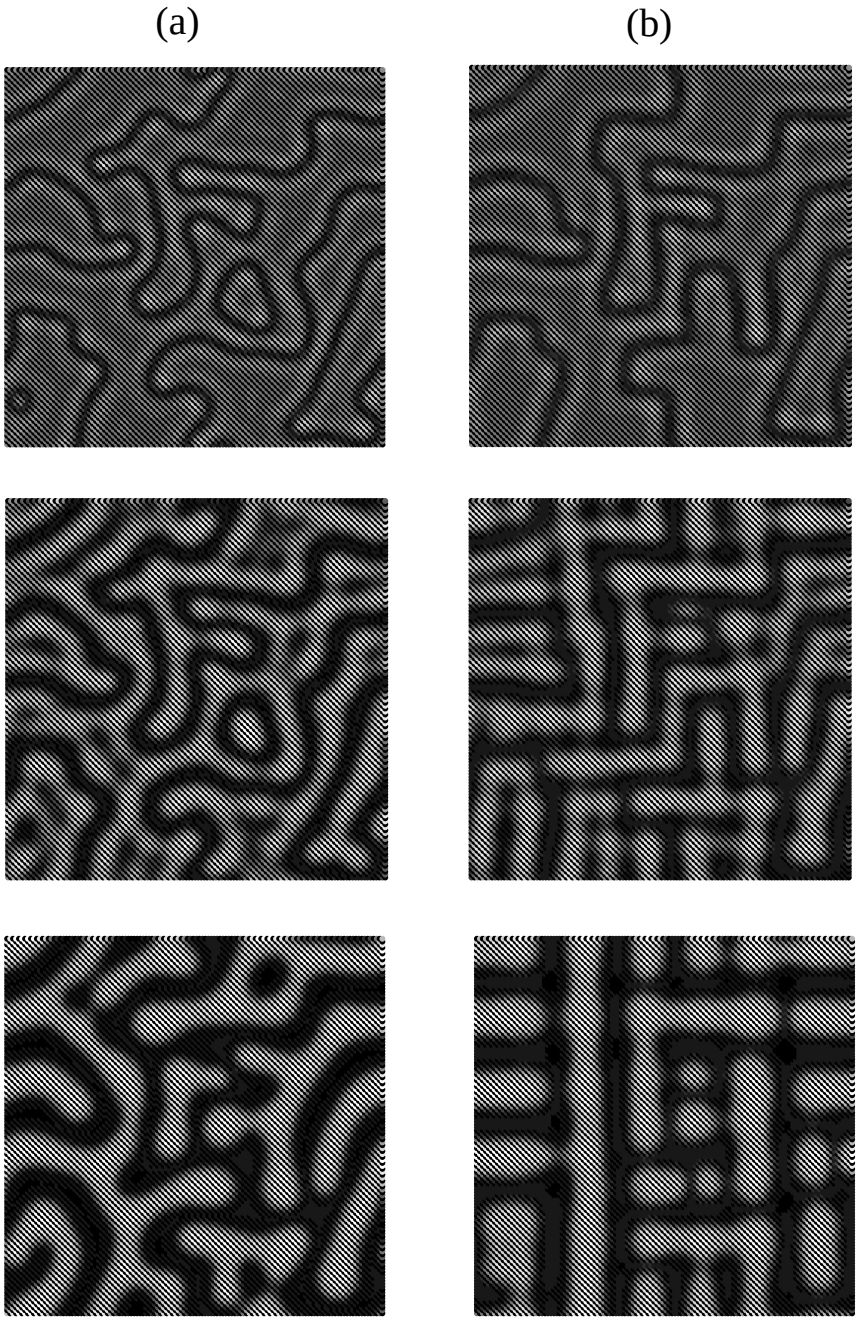


Figure 6.23: Snapshots of evolving microstructures with the mean field model with $c = 0.25$ and $T/T_t = 0.56$ showing phase separation and ordering: (a) without and (b) with elastic interactions, $B^* = 10$. Note that the presence of elastic interactions affects the critical temperature, as discussed for example in Ref. [52]. Therefore, the sequence of microstructures in (b) does not correspond to the same relative temperature as in (a), since the simulations were run at the same absolute temperature. The (reduced) simulation times $t^* = Mt$ are in (a) $t^* = 1.5$, 7 and 36, and in (b) $t^* = 0.7$, 13 and 57.

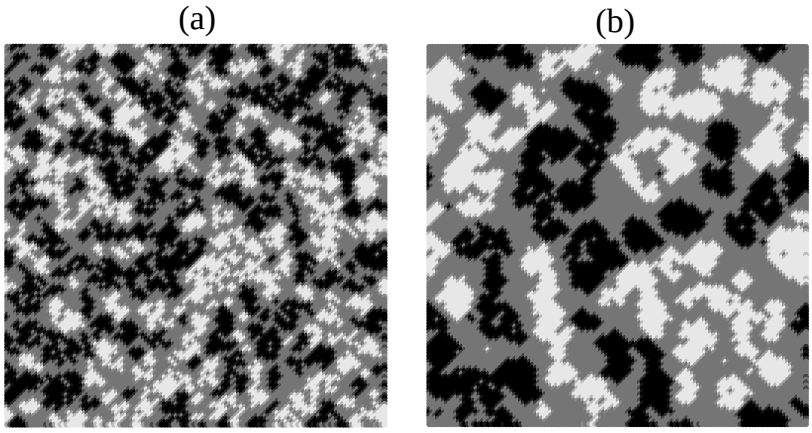


Figure 6.24: Snapshots of evolving microstructures with the Monte Carlo Kawasaki model, $c = 0.25$ and $T/T_t = 0.50$, showing phase separation and ordering. In (a) $t = 30$ (MCS) and (b) $t = 1.2 \times 10^4$ (MCS).

between phases, play no significant role yet at this stage. As the decomposition proceeds, the effect of elastic interactions becomes clear, as ordered phase prefers to align itself to $\langle 10 \rangle$ directions [9] minimizing the long range elastic interactions.

Fig. 6.24 shows microstructures obtained with the Kawasaki Monte Carlo model with $c = 0.25$ and $T/T_t = 0.50$, which approximately corresponds to the same point (P_2 in Fig. 6.22) in the phase diagram as the mean field model of Fig. 6.23.(a). Following Ref. [100], the two variants of the ordered phase in two sublattices of the system are distinguished through the variable

$$\eta_i = \frac{1}{2}\left(\sigma_i^0 + \frac{1}{4}\sum_{j \in NN(i)} \sigma_j\right) \tag{6.12}$$

where the sum goes over the nearest neighbours of site i. The sense of a variant (even or odd) is determined through σ_i^0

$$\sigma_i^0 = (-1)^{x+y}\sigma_i \tag{6.13}$$

[9] With positive elastic anisotropy, i.e. $\Delta = c_{11} - c_{12} - 2c_{44} > 0$ in Eq. (3.24), B^* is negative, and $\langle 11 \rangle$ alignment is preferred.

where x and y are the coordinates of site i. Variable η_i is -1 in within the odd variant of the ordered domains, $+1$ in the even variant, and it has intermediate values within the disordered phase. In Fig. 6.24 these values correspond to black, white and gray color, respectively. Unlike the mean field microstructures, the structure forms ordered particles immediately after the quench, and at this temperature disordered phase consists of (almost) pure B atoms. The ordered particles in Fig. 6.24 clearly have $\{11\}$ interfaces. As shown in appendix D, the energy of a $\{11\}$ interface is $E^{\{11\}} = -\frac{\sqrt{2}}{a}J_2$, and of a $\{10\}$ interface $E^{\{10\}} = -\frac{2}{a}J_2$. With $J_1 = 1$ and $J_2 = -0.5$, $\{11\}$ interfaces have lower energy, and they are therefore preferred in the system by both energetics and kinetics.

The same simulation with vacancy dynamics results in somewhat different behaviour: coarsening of the microstructure stops very soon after ordered domains are formed. The vacancy prefers to stay in disordered regions, since its binding energy to a $\{11\}$ interface is negative [10], i.e. it is energetically more favourable for the vacancy to stay in a disordered matrix than at the interface. If the vacancy enters a particle, it becomes trapped very easily. Diffusion in ordered domains is much slower than in disordered domains [101–103]. This is because vacancy diffusion through ordered domains via nearest neighbour jumps only is extremely difficult, since it distorts considerably the low energy ordered structure. It has been observed that with only nearest neighbour jumps vacancy trapping increases when ordering develops [104]. If next nearest neighbour jumps are allowed, the vacancy is able to move throughout ordered domains with no energy cost, and trapping is prevented. In reality, however, this is a highly unlikely mechanism for atomic diffusion due to the enormous activation energy, and instead the ring mechanism is likely to be operative.

With $c = 0.15$ the volume fraction of ordered domains is lower, and vacancy diffusion is easier than at higher solute concentrations. Fig. 6.25 shows snapshots of microstructures obtained with Monte Carlo simulations with $c = 0.15$ and $T/T_t = 0.90$ (point P_1 in Fig. 6.22). Again low energy $\{11\}$ interfaces are favoured, as expected, and occasional solute atoms in the matrix indicate that coarsening proceeds through LSW evaporation and condensation with both Kawasaki and vacancy dynamics. Kawasaki dynamics simulations (Fig. 6.25.(a)) show

[10] See appendix D.2.3.

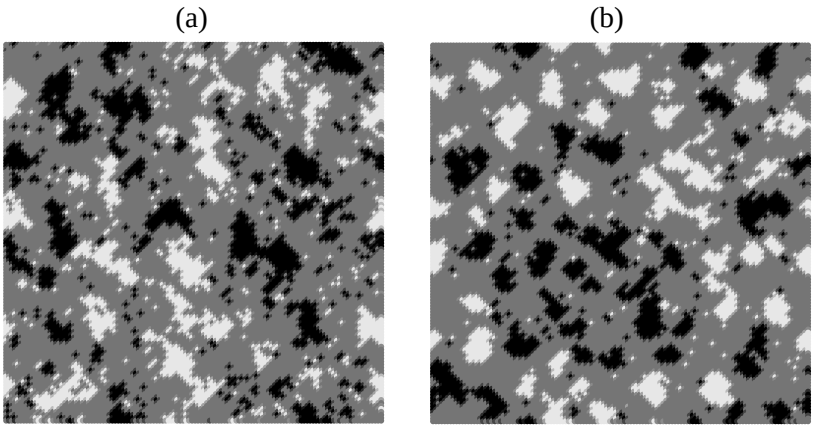


Figure 6.25: Snapshots of phase separation and ordering at $T/T_t = 0.90$ and $c = 0.15$ with (a) Kawasaki and (b) vacancy dynamics. Black and white domains are the different variants of ordered phases, as defined in Eq. (6.12), and grey denotes disordered matrix. Snapshots are chosen such that the average domain sizes are the same. Simulation time in (a) is $t = 2100$ (MCS) and in (b) $t = 0.36$.

microstructures which have rougher interfaces, and the number of solute atoms in the matrix is higher than in the corresponding vacancy dynamics microstructure (Fig. 6.25.(b)). These differences are consistent with rougher patterns observed during phase separation in section 6.3.1, and were also indicated by the scaled autocorrelation functions in Figs. 6.20 and 6.21.

6.4.2 Kinetics

The coarsening kinetics between Kawasaki and vacancy dynamics Monte Carlo simulations were compared with $c = 0.15$ and $T/T_t = 0.90$. The average domain size of the microstructure was determined by the inverse of the first moment of the radially averaged structure functions, $1/k_1$. In ordering and phase separation the structure function shows peaks close to $\mathbf{k} = (0, 0)$, corresponding to compositional heterogeneities due to decomposition, and $\mathbf{k} = \frac{2\pi}{L}(\frac{1}{2}, \frac{1}{2})$, which arises from ordering. For kinetics, only the $\mathbf{k} = (0, 0)$ long-wavelength behaviour was monitored. As in Ref. [100], only the points in the first Brillouin zone which were closer to (0,0) than to $\frac{2\pi}{L}(\frac{1}{2}, \frac{1}{2})$ were included into the long wavelength structure function.

Time evolution of average ordered domain sizes from Monte Carlo Kawasaki and vacancy dynamics simulations are shown in Fig. 6.26. The late time effective exponent, $n_{eff}(t)$, for

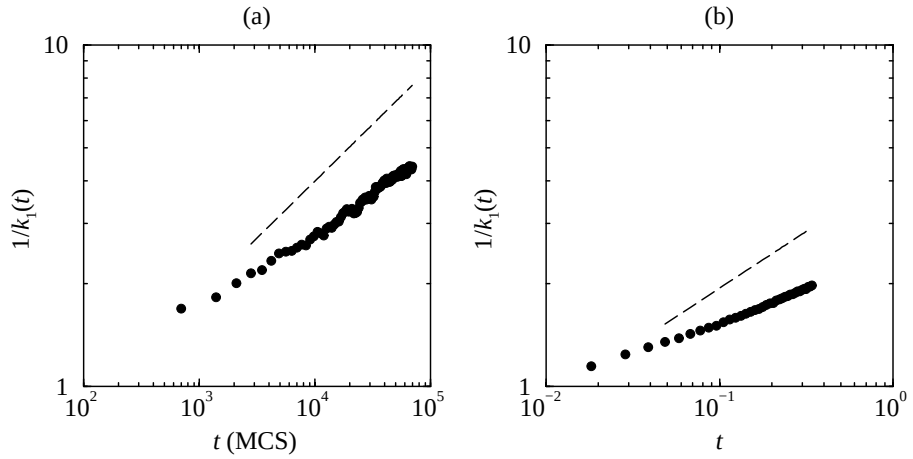


Figure 6.26: Average ordered domain sizes $1/k_1$ as function of time with $c = 0.15$ and $T/T_t = 0.90$ from Monte Carlo simulations for precipitation of ordered particles: (a) Kawasaki dynamics, (b) vacancy dynamics. The dashed line has a slope of 1/3.

Kawasaki simulations is 0.23 ± 0.03 and for vacancy simulations 0.21 ± 0.01, although the slightly increasing curvature in both cases indicates that the asymptotic growth behaviour may have not been reached yet. Note that with vacancy dynamics, simulations were not run long enough to achieve domain sizes comparable to the Kawasaki case, so that the exponents are not fully comparable with each other. The same system has been studied with Kawasaki dynamics with nearest neighbour exchanges at $T/T_t = 0.66$ by Sahni *et al.* [105], and the late time growth exponent for $c = 0.15$ case was reported as ~ 0.21 at this temperature. A more qualitative Kawasaki study at $T/T_t = 0.69$ was carried out recently by Gorentsveig *et al.* [100], and the results were reported consistent with the $R(t) = A + Bt^{1/3}$ growth law. No growth law exponents were extracted in their study, though. Athénes *et al.* studied ordering and precipitation through vacancy mechanism in a three dimensional BCC lattice [106, 107]. At $T/T_t \approx 0.5$ the growth of the mean precipitate size was found to follow the classical LSW-law. Moreover, they found that changing atomic mobilities through the asymmetry parameter $u = \epsilon^{AA} - \epsilon^{BB}$ affects the kinetic path of phase transformation at the early stages of alloy ordering.

At higher concentrations and lower temperatures vacancy trapping in ordered domains and subsequent 'locking' of the microstructures does not allow straightforward statistical interpre-

tation of the kinetics with vacancy dynamics to be made. If, despite the high activation energy, also next nearest neighbour vacancy jumps are allowed, it has been observed in computer simulations that ordering kinetics are accelerated, since the vacancy can now move easily through ordered domains without any energy cost, and prefers to stay in disordered regions [82,108,109]. As the system orders, the proportion of accepted next nearest neighbour jumps increases [109]. The trapping due to nearest neighbour jumps only has been suggested to lead to a logarithmic growth law, $R(t) \propto \ln(t)$ instead of an algebraic one [109].

6.5 Phase separation and coarsening in three dimensions

The mean field model with constant mobility was used to examine phase separation and coarsening in three dimensions. The main objective was to check whether there are qualitative differences between two and three dimensional simulations, but no systematic comparisons were carried out. Also the effect of elastic interactions on morphological development was tested. The interaction parameters for the mean field model were chosen the same as in two dimensions, e.g. $V_1 = -1$ and $V_2 = -1/\sqrt{2}$, and a $32 \times 32 \times 32$ simple cubic lattice was used. The critical temperature for the mean field model in three dimensional cubic lattice is $k_B T_c^{MF} = \frac{3}{2}|V_1 + 2V_2|$ [9].

For the Monte Carlo model, only vacancy dynamics simulations were carried out. Only first nearest neighbour interactions were included, since incorporation of second nearest neighbours was considered computationally too costly. Therefore exact comparisons between the three dimensional models cannot be made. However, the generic features of morphologies, kinetics and coarsening mechanisms seen in two dimensional simulations for phase separation and coarsening - albeit with second nearest neighbour interactions - are still evident. A larger simulation cell of $48 \times 48 \times 48$ sites in a simple cubic lattice was chosen for Monte Carlo simulations. One lattice site was vacant, corresponding to a vacancy concentration $1/48^3 = 9 \times 10^{-6}$. The critical temperature for the Monte Carlo model with only nearest neighbour interactions in a three dimensional cubic lattice is $k_B T_c \approx 4.51|J_1|$. An approximate phase diagram for the Monte Carlo model in three dimensions can be found for example on p. 200 in Ref. [110].

6.5.1 Morphologies

Fig. 6.27 shows snapshots of microstructures obtained with a mean field model after a quench to $T/T_c = 0.44$ and $c = 0.15$. In Fig. 6.27.(a) we observe spherical A-phase particles, which are randomly distributed throughout the simulation cell. During coarsening no Brownian motion of particles is observed, as expected from earlier mean field results in two dimensions. Therefore the qualitative description of phase separation remains unchanged, when modelled in three dimensions. Kinetic comparisons between two and three dimensional models were not carried out, since in sections 6.3.3 and 6.3.4 time in the (linear) mean field model was found to be a rather uninformative, meaningless and unphysical concept.

The effect of elastic interactions on morphology was also examined very briefly. In a system with elastic interactions, shown in Fig. 6.27.(b), particles align themselves along elastically soft $\langle 100 \rangle$ directions. It is interesting to note that now the particles maintain roughly equal sizes throughout the coarsening process, unlike in the model without elastic interactions.

Fig. 6.28.(a) shows microstructures with $c = 0.15$ and $T/T_c = 0.16$ obtained from three dimensional vacancy dynamics Monte Carlo simulations. We see cubical particles, the interfaces of which become clearly aligned along $\langle 100 \rangle$ directions at late times. With nearest neighbour interactions, the energies of $\{100\}$, $\{110\}$ and $\{111\}$ interfaces are

$$\begin{aligned} E^{\{100\}} &= \frac{2}{a^2}|J_1| \\ E^{\{110\}} &= \frac{2\sqrt{2}}{a^2}|J_1| \\ E^{\{111\}} &= \frac{2\sqrt{3}}{a^2}|J_1| \end{aligned} \tag{6.14}$$

i.e. $\{100\}$ interfaces have the lowest energy. In two dimensional simulations with only nearest neighbour interactions it was observed that although $\{10\}$ interfaces have lower energy, $\{11\}$ interfaces eventually dominate because vacancy motion along $\{11\}$ interfaces is slow (Fig. 6.5). This was particularly clear with $c = 0.50$ in Fig. 6.5.(c). In three dimensional simulations, however, even at late times the interfaces with the lowest energy can clearly be seen. This is the case also with $c = 0.50$, as shown in Fig. 6.28.(b).

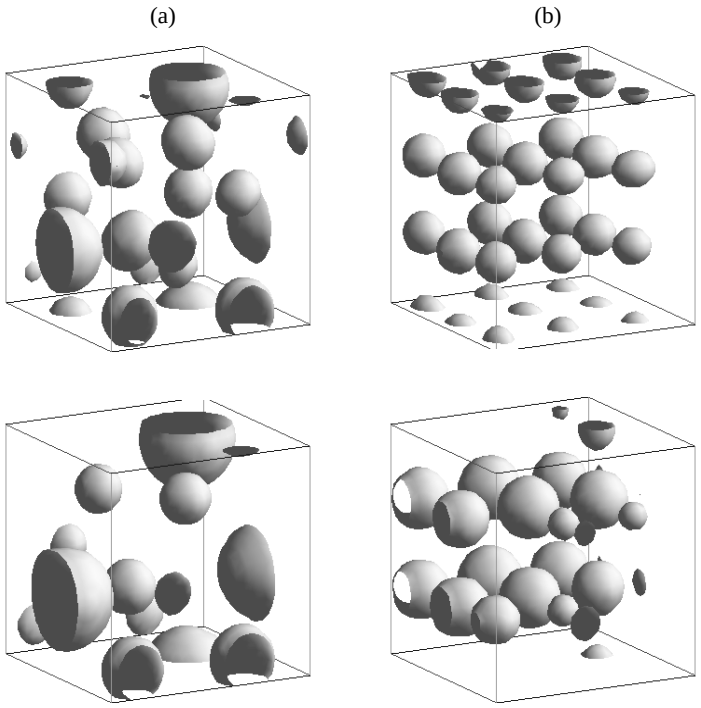


Figure 6.27: Snapshots of mean field microstructures of a system undergoing phase separation with $c = 0.15$ and $T/T_c = 0.44$. (a) No elastic interactions. (b) With elastic interactions: $B^* = 5$. Elastic interactions affect the critical temperature, but in this case the simulations were run at the same absolute temperature. Reduced simulation times are in (a) $t^* = 30$ and 43, and in (b) $t^* = 18$ and 36. Isosurfaces enclose site occupancies greater than $n_i = 0.50$.

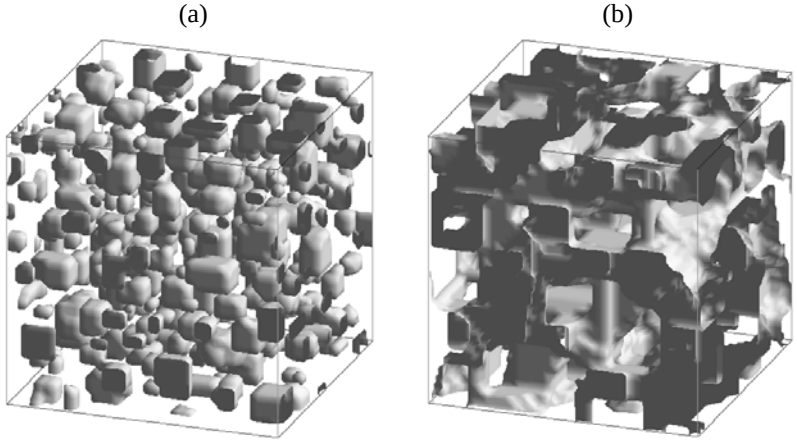


Figure 6.28: Snapshots of microstructures obtained with a vacancy Monte Carlo model at $T/T_c = 0.16$. In (a) $c = 0.15$, $t = 4.9 \times 10^7$, and (b) $c = 0.50$, $t = 8.6 \times 10^7$. Isosurfaces enclose local concentrations greater than 0.50.

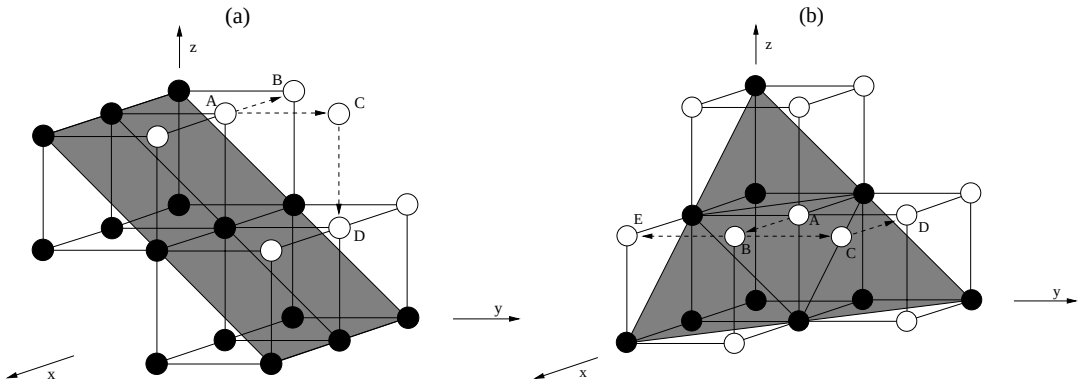


Figure 6.29: Paths for vacancy movement on {110} and {111} interfaces in a three dimensional cubic lattice. (a) At {110} interface vacancy can move free from A to B, but from A to C energy $4|J_1|$ is required. This is returned in a jump from C to D. (b) At {111} interface vacancy migration from A to E through B has activation energy of $6|J_1|$, but from B to D through C there are no energy barriers for vacancy movement.

To understand this difference we have to compare the vacancy motion at interfaces in two and three dimensions. In a two dimensional square lattice the vacancy can move along $\langle 10 \rangle$ directions freely. Vacancy migration along {11} facets involves a jump out of the interface, which costs energy $4|J_1|$, even without second nearest neighbour interactions.

In three dimensions, we consider vacancy diffusion along {100}, {110} and {111} facets. Vacancy movement along {100} interfaces is also without energy cost. It is also without energy cost if the vacancy moves along $\langle 001 \rangle$ directions in {110} interfaces, such as from A to B in Fig. 6.29.(a). For $\langle 100 \rangle$ or $\langle 010 \rangle$ jumps, such as from A to C in Fig. 6.29.(a), energy $4|J_1|$ is needed. This energy is recovered one jump later, when the vacancy returns back to the interface. At {111} interfaces, again two vacancy jumps are required. If the vacancy occupies site A at the {111} interface (Fig. 6.29.(b)), there is an energy cost of $6|J_1|$ for the outward jump to B, which is returned in jump from B to E. However, if the vacancy occupies site B, which belongs to the next layer in the $ABCABC...$ stacking sequence, there is no energy cost associated with the outward jump from B to C, and further to D. Therefore, in a three dimensional cubic lattice at {100} and {110} interfaces there are paths available for vacancy diffusion, which do not cost any energy, and at {111} interfaces the vacancy movement along the next nearest atomic layer occurs at no cost. Since most facets can now provide paths with no energy cost for vacancy

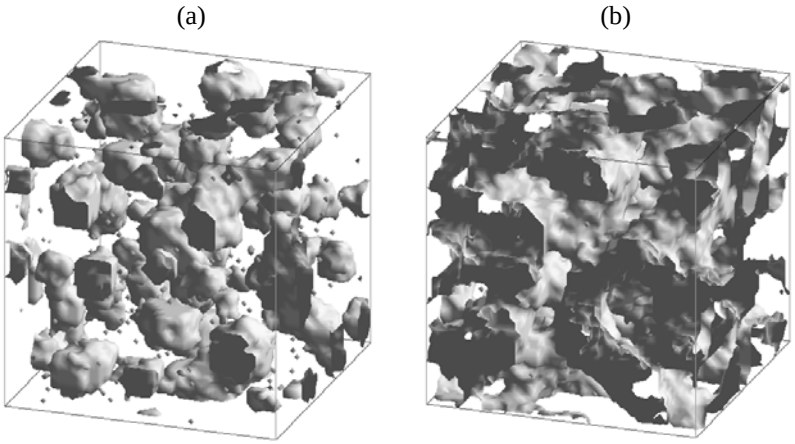


Figure 6.30: Snapshots of microstructures obtained with a vacancy Monte Carlo model at $T/T_c = 0.50$. In (a) $c = 0.15$, $t = 250$ and (b) $c = 0.50$, $t = 280$. Isosurfaces enclose local concentrations greater than 0.50.

migration, interface energies play a more dominant role in determining particle morphologies in Fig. 6.28 than in two dimensional simulations. Consequently, interface energies can be assumed to control the coarsening kinetics and evolving microstructures in binary systems, in the absence of elastic interactions.

Fig. 6.30 shows microstructures at $T/T_c = 0.50$ with $c = 0.15$ and $c = 0.50$. The higher temperature results in rougher particle shapes, and it increases the solute concentration in the matrix, as expected from two dimensional vacancy dynamics Monte Carlo simulations. There is no clear preferred interfacial alignment, and structures show all orientations.

6.5.2 Kinetics

The increase of average domain sizes in three dimensional vacancy Monte Carlo models, $1/k_1$, as a function of time is shown in Fig. 6.31. At $T/T_c = 0.16$ and with $c = 0.50$ the curve shows an increasing effective exponent, as in two dimensions, and its late time value is 0.28 ± 0.01. Similarly to the two dimensional case, with $c = 0.15$ the growth exponent remains small, at 0.13 ± 0.01 in this case. This is close to the theoretical Binder-Stauffer prediction for growth exponent in three dimensions, 1/6. However, no downward curvature, i.e. decrease in $n_{eff}(t)$, at late times is seen. This reflects the topological differences between two and three

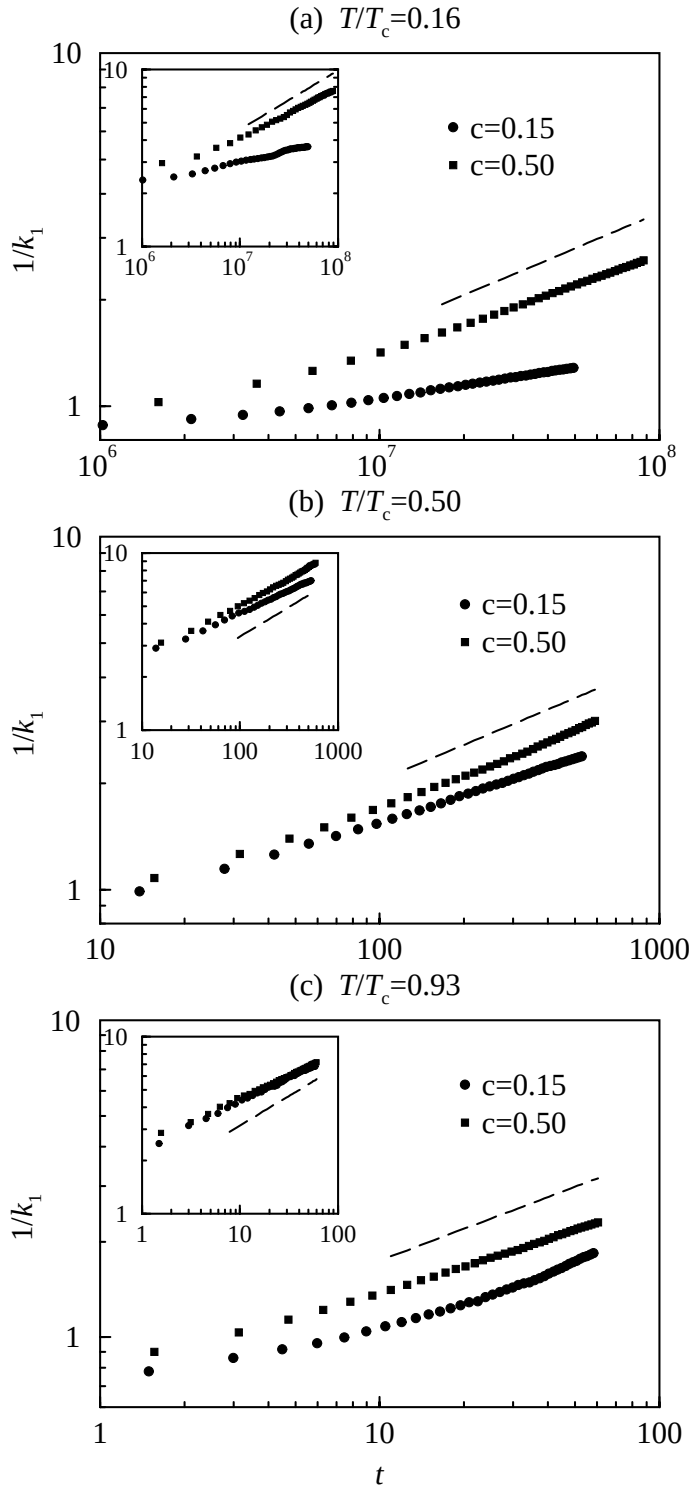


Figure 6.31: Average domain sizes $1/k_1$ as function of time from three dimensional Monte Carlo vacancy diffusion simulations. The insets show the corresponding average domain size, $R(t)$, behaviour. For comparison, the dashed line has a slope of 1/3.

dimensional systems: in three dimensions vacancies may diffuse at {100} and {110} interfaces at no energy cost, and, especially at small concentrations, the lowest energy {100} facets are clearly favoured. Immobile interfaces are not formed as easily as in two dimensional systems.

At intermediate temperatures $T/T_c = 0.50$ with $c = 0.50$, the time exponent reaches the asymptotic 1/3 limit easily, being 0.32 ± 0.01. With $c = 0.15$ the late time exponent is 0.26 ± 0.01, and clearly greater than the prediction of Binder-Stauffer theory in three dimensions. Vacancy binding energies to {100}, {110} and {111} interfaces are $2|J_1|$, $4|J_1|$ and $6|J_1|$ (or 0, if the vacancy occupies site B in Fig. 6.29.(b)), respectively, compared to the following binding energies in two dimensions (with second nearest neighbours, as in section 6.3): $2|J_1 + 2J_2|$ for {10} and $2|2J_1 + J_2|$ for {11} interfaces. Since the binding energies are lower in a three dimensional model system with nearest neighbour interactions only, the evaporation and condensation mechanism is activated more easily than in the two dimensional model studied in section 6.3. Also, from the kinetic curves and late time exponents of Fig. 6.31, the evaporation and condensation is likely to be the predominant coarsening mechanism at intermediate temperatures.

At high temperature $T/T_c = 0.93$ with $c = 0.50$ the kinetics show upwards curvature, and the late time effective exponent is 0.29 ± 0.01. With $c = 0.15$ the late time exponent 0.34 ± 0.01 exceeds the theoretical asymptotic value, which may by an anomaly due to finite size effects.

6.6 Discussion

In this chapter a comparative study of phase separation and subsequent coarsening of the microstructure was carried out using stochastic Monte Carlo and deterministic mean field models. The main objective was to investigate the role of the diffusion mechanism on morphologies, coarsening mechanisms and kinetics in model systems undergoing phase transformation. This was done by comparing the predictions for microstructural evolution between mean field and Monte Carlo models, and examining the differences between Kawasaki and vacancy dynamics in Monte Carlo simulations. Based on understanding the influence of a realistic diffusion mechanism on coarsening behaviour at different temperatures, the meaning of time scales in different models could be critically revisited. Finally, it was shown how (and why) three dimensional

simulation results may differ from behaviour observed in two dimensional systems.

The vacancy diffusion model results in different coarsening mechanisms over a range of temperatures, when a dilute random alloy is quenched into the miscibility gap. At low temperatures coarsening of the microstructure proceeds through Brownian motion and coalescence of small particles. In the late stages low energy transport paths are removed and the rate of coarsening decreases. This is the reason for the smaller exponent than is predicted by the phenomenological Binder-Stauffer theory. At intermediate temperatures, Brownian motion of particles becomes easier, and atomic evaporation and condensation are activated so that coarsening is effected by both mechanisms. At temperatures close to T_c vacancies escape more readily from interfaces, and the concentration of solute atoms in the matrix is high enough for the LSW-mechanism to dominate. When the LSW-mechanism dominates the length scale of the microstructure was found to increase with time, after long times, as $t^{1/3}$. Also, when the vacancy is trapped at interfaces of a fully connected microstructure a growth exponent 1/3 was obtained. However, this does not agree with Huse's prediction of 1/4 for coarsening enabled by interface diffusion in systems with interconnected microstructures. In two dimensions, the direct exchange Kawasaki dynamics was found to favour LSW-evaporation and condensation mechanism even at low temperatures.

At small concentrations and low temperatures, where solute is present in the form of isolated faceted particles, the particle morphology is initially dominated by interfacial energy and not by kinetics. This interpretation was checked by repeating the simulation with $J_2 = 0$. In that case $\{10\}$ facets have a lower energy than $\{11\}$ facets. At low temperatures and small concentrations it is found that $\{10\}$ facets predominate at early times, but at later times $\{11\}$ facets appear more frequently. This confirms that the morphologies of the particles are initially dominated by energetics and not kinetics. At late times in two dimensional simulations the morphologies are dominated by kinetics. In three dimensions, however, the results are somewhat different: (with nearest neighbour interactions) there are paths available for vacancy migration at no energy cost at $\{100\}$ and $\{110\}$ interfaces, and therefore the effect of kinetic factors affecting the morphology is smaller than in two dimensional systems. Consequently, it was observed that microstructural morphologies even at late times are governed by energetics. With the Monte

Carlo model, interfaces become rougher at high temperatures, but still atomically abrupt, with more $A(B)$ atoms in $B(A)$-rich domains. With the microscopic mean field model interfaces tend to be rounder and smoother at all temperatures. At temperatures close to T_c interfaces are more diffuse and the degree of inter-mixing much greater than in the Monte Carlo models.

The microscopic mean field model does not reproduce all these mechanisms of coarsening even with an environment dependent mobility. Smaller particles evaporate and disappear and neighbouring larger particles grow, but no Brownian motion of particles is observed. At larger concentrations, $c = 0.35$, coarsening through bridging between nearby particles was observed, which was predicted by mean field models with both environment dependent and constant mobilities. The free energy of the system decreases monotonically throughout the phase transformation, and there is no randomness to enable Brownian motion of particles. Above the chemical spinodal there is a nucleation barrier to phase separation, and it is necessary to seed the nucleation process artificially. Even below the spinodal the early stages of phase separation are sensitive to the initial disorder, e.g. the duration of the incubation period is sensitive to the width of the distribution of the solute concentration in the model of the random alloy [95]. In the Monte Carlo models these thermally activated processes appear naturally. Introducing an environment dependent mobility does not alter the qualitative behaviour of the mean field model.

Time in the microscopic mean field model cannot be related to real time unless the microstructure varies over length scales much greater than than the atomic scale. In contrast to the case of a vacancy mechanism of diffusion, the mobility in the microscopic mean field model does not depend on the local atomic environment. Each bond is a conduit for material transfer in both directions, and the activation energy is an average of the activation energies for an atom to jump in either direction. To a good approximation this average activation energy is independent of the local atomic environment. As for Kawasaki simulations, the often assumed linear dependence between Monte Carlo time and real physical time becomes questionable, as the importance of a realistic diffusion mechanism in models for phase transformation in binary systems is understood. The fact that with Kawasaki dynamics, LSW-evaporation and condensation is the favoured mechanism of coarsening indicates that time scales associated

with other coarsening mechanisms are suppressed. In this respect, as the average domain size increases in the system, the relative importances of different coarsening mechanisms vary, and the assumption of a linear relation between the time scales may become distorted.

Chapter 7

Future challenges

This chapter outlines some unresolved problems or less explored areas in modelling microstructural evolution, which have been prompted by this work or by the literature. Some of the topics presented have been recognized for decades, but still a mathematical framework enabling computer simulations is lacking. Although the physics is often understood the processes are complicated, and building up mathematical theories is crucial for making real breakthroughs.

7.1 Improving the atomic diffusion mechanism(s)

Although this thesis represents only a limited study on the effect of vacancy dynamics, it has clearly demonstrated that even a simple two-dimensional square lattice can reveal a variety of different types of coarsening behaviour over a range of temperatures. There are unexplored aspects in understanding the effects of diffusion mechanism on microstructural evolution. In section 6.4 simulations for simultaneous ordering and phase separation showed that with nearest neighbour jumps vacancy can easily become trapped at ordered domains. A full understanding of the effects of vacancy dynamics in this case has not been achieved. If next nearest jumps are allowed, the vacancy movement through ordered domains is enabled without any cost of energy. This certainly affects the kinetic behaviour, but in reality the occurrence of second nearest neighbour jumps is very rare due to high activation energy. Instead, incorporation of ring diffusion mechanism [58, 59, 64, 111] would provide a more realistic the description of diffusion in ordered domains. Also, as shown in section 6.5, simulations in three dimensions

can lead to somewhat different behaviour from two dimensional studies, since the topology of the system allows more freedom for vacancy movement than a two dimensional lattice, and slowing down of kinetics due to formation of immobile facets was not observed. Further investigations on the impact of system topology on vacancy motion would provide new insights into understanding the mechanisms of microstructural evolution.

The evolution of microstructure is microscopically mediated by defects. In simulation models only conservative point defects have been considered, although the non-conservative nature of point defects, i.e. vacancies and interstitials, may sometimes be important. Processes, such as defect recombination and elimination occurring in real systems, have not been taken into account. The equilibrium concentration of vacancies, for example, depends on the temperature: it is much higher at the alloy treatment temperature than at the ageing temperature within the miscibility gap. When the alloy is rapidly quenched from the high temperature, there will be a high quenched-in vacancy concentration until the excess vacancies anneal out. Vacancies tend to form clusters, which in turn may become dislocation loops [1]. Therefore, excess vacancies at early stages of phase separation provide sites for heterogeneous nucleation. In addition, quenched-in vacancies enhance the atomic diffusion at the ageing temperature, which accelerates the nucleation and growth processes.

In Monte Carlo and mean field models, the A and B atoms are located in rigid lattice sites, so that only coherent phase transformations in single crystals can be modelled. For real metals, however, this may sometimes be too great a simplification, because it also affects the atomic migration: diffusion is a structure sensitive phenomenon, and the activation energy for diffusion is lower in regions of 'bad' crystal, such as grain boundaries, dislocations and interfaces. Defected areas have generally more open crystal structure and it has been observed experimentally that the jump frequency of atoms migrating along defects is higher than for diffusion in undefected lattice [1]. Therefore diffusion along these defects may under certain circumstances become the dominant diffusion path. However, description of diffusion along grain boundaries is difficult, since generally the grain boundary structures are complex and irregular, and different mechanisms may be operative in different boundaries [77].

Theoretical and mathematical models for diffusion induced by external fields are still rather

elementary. In driven alloys the formation of point defects is enhanced due to external irradiation. In this case there is a competition between increased thermally activated diffusion and ballistic effects, such as displacement cascades and collision sequences [112]. Microstructural evolution under neutron irradiation has been receiving increasing attention due to its technological interest in nuclear power generation applications. The number of modelling studies in this area are still relatively few, but discussion has started due to the pioneering work by Martin *et al.* [90, 112–114].

7.2 Elastic energy and dissimilar elastic moduli

A description of dynamics of growth of new phase particles and coarsening of the microstructure in the presence of elastic interactions is complicated. Internal stresses affect both the final equilibrium configuration of the system, and the evolution towards it. Since elastic stresses are functions of particle shapes and their distribution within the system, there are strong spatial correlations between the particles.

There are few studies on the effect of elastic energy on evolving microstructures, since the current mathematical descriptions of elastic energy are restricted to systems with homogeneous elastic moduli. In this case the elastic energy can be expressed in closed form, and incorporated into the free energy formulation of the driving force. In the elastically inhomogeneous systems, however, the strain-induced interaction between the elements of the system cannot be reduced to pairwise interactions, as in the case of elastically homogeneous system, but the interactions are multiparticle ones. For modelling many alloys of practical importance, in which elastic moduli of the matrix and precipitates often differ, this is a serious limitation. It would be useful to establish a direct relation between the strain energy response to an incremental change of the microstructure, but this analytical framework for computer simulations of mesoscopic pattern evolution is still required.

7.3 Semicoherent interfaces and motion of dislocations

Elastic interactions arise due to the mismatch of particle and matrix lattice constants. As the average particle size increases, coherency strains cannot be maintained, but excess elastic energy is released through interfacial dislocations. At the interface a transition from coherency to semicoherency occurs. This results in release in long-range elastic interactions, but increases the energy related to the dislocation cores. These misfit dislocations will also influence glide dislocations, as they shear through the particles, but their full impact is not understood. Dislocation motion is essential in determining the ductility and toughness of the material.

The spatial extent of line defects often encompasses both atomic and mesoscopic length scales, which makes it necessary to include large numbers of atoms in the simulations. A mathematical description for how to incorporate dislocations into energy minimization approach is needed. This would enable simulations of systems in which differences in particle/matrix lattice constants are non-negligible and a transition from coherent to semi-coherent interfaces may occur.

7.4 Rafting in NiAl superalloys

There is a lot of current interest in NiAl superalloys. These single crystal nickel-base alloys, which have been developed through the last 60 years, have proved to have superior mechanical properties in high temperature structural applications, such as power generation or air travel. This is achieved through directionally aligned grains and single crystals, as a result of which the alloys can resist creep deformation at high loads to approximately 80% of the melting point [2].

The very stable nature of NiAl superalloys is due to aluminium rich ordered cubic particles, which are immersed in a disordered matrix. The coherent γ' particles have a low particle/interface energy, typically 8-20 mJ/m^2 [38], and they coarsen very slowly. The sizes of γ' phase particles and the coarsening rate directly affect the strength of the alloy. There is a slight lattice mismatch between the γ and γ', which is important in determining the utility of the superalloys. In some cases the misfit strain becomes so high that interfacial dislocations are formed between the γ and γ' phases: the precipitates become semicoherent and the interfacial

energy increases.

Since the mechanical properties of nickel-base superalloys rely on these particular microstructural features, any phenomenon affecting the morphology of the γ' precipitates is of immense technological interest. In Ni-base modern superalloys, changes in precipitate morphology due to applied uniaxial stress is called rafting. Most modern single-crystal superalloys develop lamellar structures and plates under tension and needles under compression, but in this respect creep experiments on superalloys are somewhat contradictory [40]. Although the effect of rafting on mechanical properties is not yet fully understood, it would be extremely useful to predict and control the evolution of the rafted microstructures. In order to describe rafting and imposed external loading, the thermodynamic driving force for these transformations has to be understood. This is a complicated task since different phases of the single crystal alloy are strongly coupled with the external loading through anisotropic elastic interactions. In the elastic regime, it has been shown with simple arguments that the thermodynamic driving force for rafting is proportional to the applied stress, to the difference is lattice parameters of the γ matrix and γ' particles, and to the difference of their elastic constants [38].

From a modelling point of view microstructural evolution under external loading represents a relatively unexplored area. Gayda and Srolovitz [115] attempted to model rafting by using a combined Monte Carlo/finite element approach, which relies on the elastic strain energy and an isotropic interfacial energy term. As a major drawback, large amount of computation was needed even for small lattice sizes. Vallés and Arrell [116, 117] modelled a system, where the particle/matrix interfacial strains caused by lattice misfit and external loading are relieved through a formation of a regular array of interface dislocations. By evaluating the energy and spacing of the dislocations in directions parallel and perpendicular to the axis of applied load, the anisotropy in dislocation density was cast into a quantitative criterion used in Monte Carlo simulations. Instead of incorporating the long-range elastic energy contributions, the problem was described by considering different precipitate-matrix interfacial energies along principal lattice directions. This approach allows considerably faster simulation of the microstructures than the method of Ref. [115]. A secondary effect of dislocation arrays which influences the rafting process, is an anisotropy in the diffusion rate through diffusion dislocation pipes. Diffu-

sion through dislocation pipes is faster than bulk diffusion, and therefore it is expected that the diffusion rates will be different in directions perpendicular and parallel to the applied external load. This effect is not included in the description of the model in Refs. [116, 117].

Appendix A

Mean field phase diagram

We have probabilities for site occupancies n_i, which have values $0 \leq n_i \leq 1$. The Bragg-Williams mean field free energy can be written as a sum over the lattice sites as

$$F = \frac{1}{2}\sum_{i,j}\Big\{n_i n_j \varepsilon_{ij}^{AA} + [n_i(1-n_j) + n_j(1-n_i)]\varepsilon_{ij}^{AB} + (1-n_i)(1-n_j)\varepsilon_{ij}^{BB}\Big\} + k_B T \sum_i n_i \ln n_i + (1-n_i)\ln(1-n_i) \tag{A.1}$$

In the disordered regime n_i's approach to the average composition c, and Eq. (A.1) becomes

$$F = \frac{1}{2}\sum_{i,j}\Big\{c^2(\varepsilon_{ij}^{AA} + \varepsilon_{ij}^{BB} - 2\varepsilon_{ij}^{AB}) + 2c(\varepsilon_{ij}^{AB} - \varepsilon_{ij}^{BB}) + \varepsilon_{ij}^{BB}\Big\} + Nk_BT[c\ln c + (1-c)\ln(1-c)] \tag{A.2}$$

Let us denote $\alpha_{ij} = \varepsilon_{ij}^{AA} + \varepsilon_{ij}^{BB} - 2\varepsilon_{ij}^{AB}$ and $\beta_{ij} = \varepsilon_{ij}^{AB} - \varepsilon_{ij}^{BB}$. Now $\sum_{i,j}\alpha_{ij} = N\tilde{\alpha}(0)$, where $\tilde{\alpha}(0)$ is the Fourier transform of α_{ij} at $\mathbf{k} = 0$ (correspondingly for β_{ij} and ε_{ij}^{BB}), which gives

$$F = \frac{1}{2}Nc^2\tilde{\alpha}(0) + cN\tilde{\beta}(0) + \frac{1}{2}N\tilde{\varepsilon}^{BB}(0) + Nk_BT[c\ln c + (1-c)\ln(1-c)] \tag{A.3}$$

The solubility limits are found by the common tangent construction of the free energy curve. The alloy exists as a two-phase mixture in compositions, between which the free energy curve lies above the common tangent (Fig. A.1). Mathematically the points of common tangents are

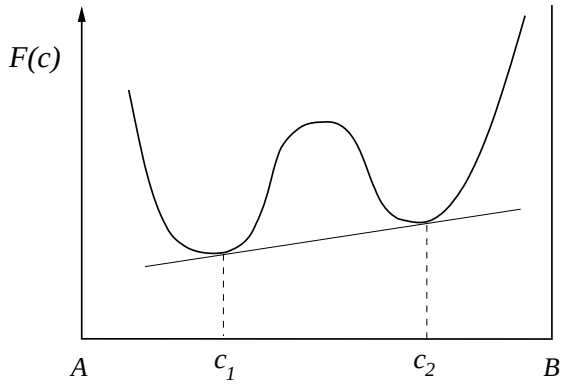


Figure A.1: Free energy as a function of concentration. The common tangent construction determines the solubility limits which separate the two-phase mixtures.

expressed as

$$\frac{F(c_1) - F(c_2)}{c_1 - c_2} = \left(\frac{\partial F}{\partial c}\right)_{c=c_1} = \left(\frac{\partial F}{\partial c}\right)_{c=c_2} \tag{A.4}$$

From Eq. (A.4) we can see that the points of common tangents, and therefore the equilibrium phase diagram, do not change, if the free energy is shifted by an amount μc, where μ is a constant [9]. By doing the shift, we can make the free energy symmetric around $c = 0.5$:

$$\begin{aligned} f^*(c) &= \frac{F}{N} - c\tilde{\beta}(0) - \frac{1}{2}c\tilde{\alpha}(0) \\ &= \frac{1}{2}\tilde{\alpha}(0)c(1-c) + \frac{1}{2}\tilde{\varepsilon}^{BB}(0) + k_BT[c\ln c + (1-c)\ln(1-c)]. \end{aligned} \tag{A.5}$$

Decomposition takes place, if $\tilde{\alpha}(0) \leq 0$. The reduced free energy then reads as

$$f(c) = \frac{f^*(c)}{|\tilde{\alpha}(0)|} = -\frac{1}{2}c(1-c) + \frac{1}{2}\frac{\tilde{\varepsilon}^{BB}(0)}{|\tilde{\alpha}(0)|} + \frac{k_BT}{|\tilde{\alpha}(0)|}[c\ln c + (1-c)\ln(1-c)]. \tag{A.6}$$

Now the common tangent and the solubility curve is determined by condition

$$\frac{df(c)}{dc} = 0 \tag{A.7}$$

which is mathematically simple to solve compared to applying Eq. (A.4) directly to Eq. (A.3)

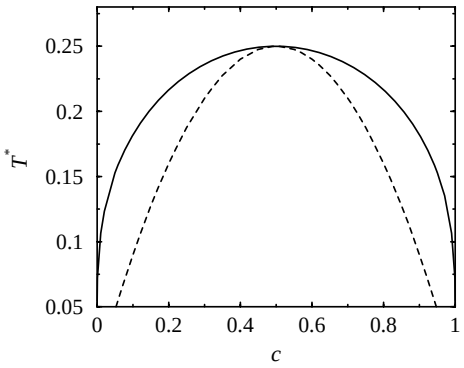


Figure A.2: The equilibrium mean field phase diagram. T^* is the reduced temperature $T^* = k_BT/|\tilde{\alpha}(0)|$, thick line is the solubility curve, Eq. (A.9), and dashed line describes the spinodal, Eq. (A.11).

.

[1]. We get

$$\frac{1}{2} - c + \frac{k_BT}{|\tilde{\alpha}(0)|} \ln \frac{c}{1-c} = 0 \tag{A.8}$$

or

$$\frac{k_BT}{|\tilde{\alpha}(0)|} = \frac{c - \frac{1}{2}}{\ln \frac{c}{1-c}}. \tag{A.9}$$

The solubility curve is plotted [2] in Fig. A.2. The spinodal is defined as

$$\frac{d^2 f(c)}{dc^2} = 0 \tag{A.10}$$

which gives

$$\frac{k_BT}{|\tilde{\alpha}(0)|} = c(1-c). \tag{A.11}$$

In Fig. A.2 the spinodal is denoted by the dashed line.

[1] This is because the free energy in Eq. (A.3) is not symmetric, and the common tangent has a slope different from zero.

[2] Note that L'Hospital's rule is used at $c = 0$ and $c = 0.5$.

Appendix B

Discretization of Cahn equation

The continuum Cahn equation for a conserved field variable, e.g. concentration, reads as

$$\frac{dc(\mathbf{r},t)}{dt} = M\nabla^2 \frac{\delta F}{\delta c(\mathbf{r},t)}. \tag{B.1}$$

Without losing generality, we can examine it in 1D, when we have $\nabla^2 \equiv \frac{\partial^2}{\partial x^2}$. Now we can approximate (see Fig. B.1.)

$$\frac{\partial f}{\partial x} = f_{i+1} - f_i \tag{B.2}$$

and

$$\frac{\partial}{\partial x}\frac{\partial f}{\partial x} = \frac{\partial}{\partial x}(f_{i+1} - f_i) \tag{B.3}$$

$$= f_{i+1} - f_i - f_i + f_{i-1} \tag{B.4}$$

$$= f_{i+1} + f_{i-1} - 2f_i \tag{B.5}$$

$$= \sum_{j \in N(i)} (f_j - f_i) \tag{B.6}$$

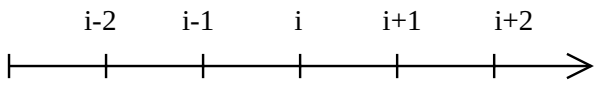


Figure B.1: Space discretization in one dimension.

where $N(i)$ denotes the nearest neighbours of site i. Denote $f_i \equiv \frac{\partial F}{\partial c_i}$, which gives the microscopic Khachaturyan equation:

$$\frac{\partial c_i}{\partial t} = \sum_{j \neq i} M_{ij} (\frac{\partial F}{\partial c_j} - \frac{\partial F}{\partial c_i}). \tag{B.7}$$

Appendix C

Elastic energy approximation

Strain energy due to concentration inhomogeneities is [9]

$$E_{el} = \frac{1}{2N} \sum_{\mathbf{k}} \tilde{B}_{\mathbf{e}} |\tilde{n}_{\mathbf{k}}(t)|^2 \tag{C.1}$$

where the long-wavelength limit of $\tilde{B}_{\mathbf{e}}$ reads as

$$\tilde{B}_{\mathbf{e}} = -e_i \sigma^0_{ij} \Omega_{(jk)\mathbf{e}} \sigma^0_{kl} e_l + \langle e_i \sigma^0_{ij} \Omega_{(jk)\mathbf{e}} \sigma^0_{kl} e_l \rangle. \tag{C.2}$$

For a cubic substitutional solution we have

$$u^0_{ij} = \varepsilon_0 \delta_{ij} \tag{C.3}$$

$$\lambda_{1111} = \lambda_{2222} = \lambda_{3333} = c_{11} \tag{C.4}$$

$$\lambda_{1122} = \lambda_{2233} = \lambda_{1133} = c_{12} \tag{C.5}$$

$$\lambda_{1212} = \lambda_{1313} = \lambda_{2323} = c_{44} \tag{C.6}$$

which gives

$$\sigma^0_{ij} = \lambda_{ijkl} u^0_{kl} = \varepsilon_0 (c_{11} + 2c_{12}) \delta_{ij}. \tag{C.7}$$

Green's tensor for elasticity $\Omega_{\mathbf{e}}$ has the properties $\Omega_{\mathbf{e}}\Omega_{\mathbf{e}}^{-1} = \mathbf{1}$ and $\Omega_{\mathbf{e}}^{-1} = \lambda_{ijkl}e_k e_l$. From these (after some tedious calculations) we get the components of the tensor $\Omega_{\mathbf{e}}$:

$$\Omega_{(ii)\mathbf{e}} = \frac{c_{44} + (c_{11} - c_{44})(e_j^2 + e_k^2) + \xi(c_{11} + c_{12})e_j^2 e_k^2}{c_{44}D_{\mathbf{e}}} \tag{C.8}$$

$$\Omega_{(ij)\mathbf{e}} = -\frac{(c_{12} + c_{44})(1 + \xi {e_k}^2)}{c_{44}D_{\mathbf{e}}}e_i e_j \tag{C.9}$$

where $\xi = \frac{c_{11}-c_{12}-2c_{44}}{c_{44}}$ is the elastic anisotropy parameter and

$$D_{\mathbf{e}} = c_{11} + \xi(c_{11} + c_{12})(e_1^2e_2^2 + e_1^2e_3^2 + e_2^2e_3^2) + \xi^2(c_{11} + 2c_{12} + c_{44})e_1^2e_2^2e_3^2. \tag{C.10}$$

For simplicity, let's denote $L_{\mathbf{e}} = e_i\sigma_{ij}^0\Omega_{jk\mathbf{e}}\sigma_{kl}^0 e_l$ in Eq. (C.2). After inserting Eqs. (C.7) and (C.9) it becomes

$$L_{\mathbf{e}} = (\varepsilon_0)^2\frac{(c_{11} + 2c_{12})^2}{c_{11}}\phi_{\mathbf{e}} \tag{C.11}$$

where

$$\phi_{\mathbf{e}} = \frac{(1 + 2\xi(e_1^2e_2^2 + e_1^2e_3^2 + e_2^2e_3^2) + 3\xi^2e_1^2e_2^2e_3^2)c_{11}}{c_{11} + \xi(c_{11} + c_{12})(e_1^2 + e_1^2e_3^2 + e_2^2e_3^2) + \xi^2(c_{11} + 2c_{12} + c_{44})e_1^2e_2^2e_3^2}. \tag{C.12}$$

This result is exact, but in order to estimate analytically the mean value $\langle\phi_{\mathbf{e}}\rangle$ needed in Eq. (C.2), we can approximate Eq. (C.12) by

$$\hat{\phi}_{\mathbf{e}} \cong 1 + 4\frac{\Delta}{c_{11} + c_{12} + 2c_{44}}(e_1^2e_2^2 + e_1^2e_3^2 + e_2^2e_3^2) + 54\frac{\Delta^2e_1^2e_2^2e_3^2}{(c_{11} + c_{12} + 2c_{44})(c_{11} + 2c_{12} + 4c_{44})} \tag{C.13}$$

where $\Delta = c_{11} - c_{12} - 2c_{44}$. This function equals Eq. (C.12) along the symmetric directions, $\mathbf{e}||[100], [111], [110]$. For other directions $\hat{\phi}_{\mathbf{e}}$ deviates by no more than a few percent from the

exact values of $\phi_{\mathbf{e}}$. Now

$$\langle\hat{\phi}_{\mathbf{e}}\rangle \cong 1 + \frac{4}{5}\frac{c_{11}-c_{12}-2c_{44}}{c_{11}+c_{12}+2c_{44}} + \frac{18}{35}\frac{(c_{11}-c_{12}-2c_{44})^2}{(c_{11}+2c_{12}+4c_{44})(c_{11}+c_{12}+c_{44})} \tag{C.14}$$

because in 3D $\langle e_1^2 e_2^2\rangle = 1/15$ and $\langle e_1^2 e_2^2 e_3^2\rangle = 1/105$. Configurationally dependent elasticity in the mean field approximation (C.2) now becomes

$$\begin{aligned}\tilde{B}_{\mathbf{e}} &= -L_{\mathbf{e}} + \langle L_{\mathbf{e}}\rangle \\ &= (\varepsilon_0)^2\frac{(c_{11}+2c_{12})^2}{c_{11}}\Big[\frac{-4\Delta}{c_{11}+c_{12}+2c_{44}}\{(e_1^2e_2^2+e_1^2e_3^2+e_2^2e_3^2-\frac{1}{5}) \\ &- \frac{27\Delta}{2(c_{11}+2c_{12}+4c_{44})}(e_1^2e_2^2e_3^2-\frac{1}{105})\}\Big].\end{aligned} \tag{C.15}$$

For a 2D case this can be written as

$$\begin{aligned}\tilde{B}_{\mathbf{e}} &= \varepsilon_0^2\frac{(c_{11}+2c_{12})^2}{c_{11}}\Big[\frac{-4\Delta}{c_{11}+c_{12}+2c_{44}}\{e_1^2e_2^2-\frac{1}{8}\}\Big] \\ &= B^*(e_1^2e_2^2-\frac{1}{8})\end{aligned} \tag{C.16}$$

because $\langle e_1^2 e_2^2\rangle = 1/8$ in 2D and $B^* = \frac{-4\Delta\varepsilon_0^2(c_{11}+2c_{12})^2}{c_{11}(c_{11}+c_{12}+2c_{44})}$.

Appendix D

Energies at interfaces

D.1 Interface energies

The energy of an $\{xy\}$ interface is defined as

$$E^{\{xy\}} = \frac{E^{int} - E^0}{l}. \tag{D.1}$$

where E^{int} is the energy of the system with the interface, E^0 energy without the interface, and l is the length of the interface.

D.1.1 Pure A and B phases

In Fig. D.1.(a), atoms marked with a cross are affected by the $\{10\}$ interface. The energy of these atoms is $E^{int} = 2 \cdot \frac{1}{2} \cdot 2J_1 = 2J_1$, and the energy of A and B atoms in bulk material is $E^0 = 2 \cdot \frac{1}{2}(4J_1 + 4J_2) = 4(J_1 + J_2)$ Therefore, the energy of an $\{10\}$ interface is

$$E^{\{10\}} = \frac{2J_1 - 4(J_1 + J_2)}{a} = \frac{-2(J_1 + 2J_2)}{a} \tag{D.2}$$

where a is the lattice parameter.

At $\{11\}$ interface, four atoms marked with a cross in Fig. D.1.(b) are considered. The energy of an atom at the immediate vicinity of the interface is $\frac{1}{2} \cdot 2 \cdot J_2 = J_2$, and of an atom further in the bulk $\frac{1}{2}(4J_1 + 2J_2) = 2J_1 + J_2$, giving $E^{int} = 2(2J_1 + J_2) + 2J_2$. The energy of

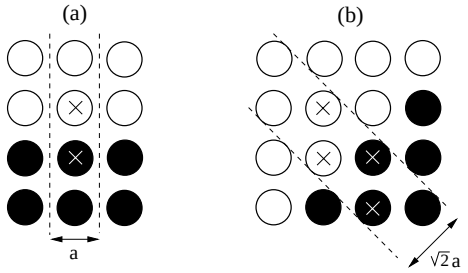


Figure D.1: (a) {10} and (b) {11} interfaces. Atoms marked with a cross are affected by the interface, and a is the lattice constant of a square lattice.

an atom in the bulk is $2(J_1 + J_2)$, and the energy of a {11} interface becomes

$$E^{\{11\}} = \frac{[2(2J_1 + J_2) + 2J_2] - 4 \cdot 2(J_1 + J_2)}{\sqrt{2}a} = \frac{-2\sqrt{2}(J_1 + J_2)}{a}. \tag{D.3}$$

If $J_1 = \sqrt{2}J_2$, energies of {10} and {11} interfaces are equal: $E^{\{10\}} = -2(2+\sqrt{2})J_1/a = E^{\{11\}}$. If $|J_1| > |\sqrt{2}J_2|$, then $E^{\{10\}} < E^{\{11\}}$.

D.1.2 Ordered particles in a disordered matrix

At {10} interfaces marked atoms in Fig. D.2.(a) are considered. The energy of these atoms is $E^{int} = \frac{1}{2}[(2J_1 + 4J_2) + 4J_1 + (-2J_1 + 4J_2) - 4J_1] = 4J_2$, and the energy of the same atoms in pure ordered and disorderd phases is $E^0 = \frac{1}{2}[2(4J_1 + 4J_2) + 2(-4J_1 + 4J_2)] = 8J_2$. Therefore, the energy of a {10} interface is

$$E^{\{10\}} = \frac{4J_2 - 8J_2}{2a} = \frac{-2J_2}{a}. \tag{D.4}$$

A {11} interface is shown in Fig. D.2.(b). Now $E^{int} = \frac{1}{2}[(4J_1+2J_2)+4J_2+(-4J_1+2J_2)] = 4J_2$. At {11} interfaces great care has to be taken to define what the reference phase for each atom without the interface is. Namely, the atom indicated by the arrow in Fig. D.2.(b) has equal number of wrong bonds to be considered an atom belonging either to an ordered or to a disordered phase. Therefore its energy without the interface is defined as an average of energies of being in an ordered or disordered phase. Without the interface the energy of the atoms then becomes $E^0 = \frac{1}{2}[(4J_1 + 4J_2) + \frac{1}{2}(4J_1 + 4J_2 - 4J_1 + 4J_2) + (-4J_1 + 4J_2)] = 6J_2$. The energy of

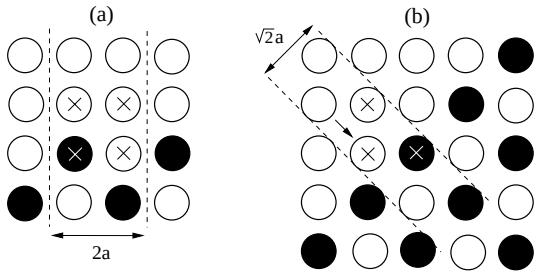


Figure D.2: (a) {10} and (b) {11} ordered particle/matrix interfaces. Atoms marked with a cross are affected by the interface. a is the lattice constant of a square lattice.

a {11} interface is

$$E^{\{11\}} = \frac{4J_2 - 6J_2}{\sqrt{2}a} = \frac{-\sqrt{2}J_2}{a}. \tag{D.5}$$

With $J_1 = 1$ and $J_2 = -\frac{1}{2}$, a {11} interface has lower energy.

D.2 Vacancy binding energies to interfaces

Vacancy binding energy is the difference in total energy of the system, when the vacancy is at the interface or in the bulk:

$$E_b^{\{xy\}} = E_v^{bulk} - E_v^{int}. \tag{D.6}$$

D.2.1 Pure A and B phases: $\epsilon^{AA} = \epsilon^{BB}$

If we have interactions up the second nearest neighbours in a two dimensional square lattice, the vacancy binding energy to a {10} interface (Fig. D.3.(a)) is

$$E_b^{\{10\}} = 2J_1 - (4J_1 + 4J_2) = -2(J_1 + 2J_2) \tag{D.7}$$

and to a {11} interface (Fig. D.3.(b))

$$E_b^{\{11\}} = 2J_2 - (4J_1 + 4J_2) = -2(2J_1 + J_2). \tag{D.8}$$

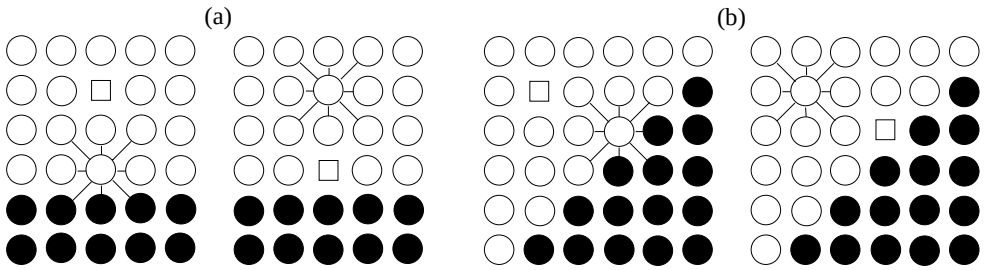


Figure D.3: Vacancy binding to (a) {10} and (b) {11} interfaces. The marked bonds contribute to the energy difference, when the vacancy binding energies are determined by Eq. (D.6).

If $J_2 = \sqrt{2}J_1$, the binding energies are $E_b^{\{10\}} = 2(\sqrt{2}+1)|J_1|$, and $E_b^{\{11\}} = (4\sqrt{2}+1)|J_1|$, i.e. the binding energy to a {11} interface is greater than to a {10} interface.

D.2.2 Pure A and B phases: $\epsilon^{AA} \neq \epsilon^{BB}$

In this case the correction term due to the vacancy cannot be ignored in Eq. (6.3). Let us denote $K_1 = \frac{1}{4}(\epsilon_1^{AA} - \epsilon_1^{BB})$ and $K_2 = \frac{1}{4}(\epsilon_2^{AA} - \epsilon_2^{BB})$. Now the vacancy binding energy to a {10} interface is

$$E_b^{\{10\}} = (2J_1 - 4K_1 - 4K_2) - (4J_1 + 4J_2 - 2K_1) = -2(J_1 + 2J_2) - 2(K_1 + 2K_2) \tag{D.9}$$

and to a {11} interface it is

$$E_b^{\{11\}} = (2J_2 - 4K_1 - 4K_2) - (4J_1 + 4J_2 - 2K_2) = -2(2J_1 + J_2) - 2(2K_1 + K_2). \tag{D.10}$$

Since J's do not define K's in a unique way, by adjusting K_1 and K_2 the binding energies of the vacancy to interfaces can be changed. Although this has no effect on the equilibrium phase diagram, it is likely to affect the coarsening mechanism.

D.2.3 Ordered particles in a disordered matrix

The vacancy binding energy to a {10} interface (Fig. D.4.(a)) is

$$E_b^{\{10\}} = (2J_1 + 4J_2) - (4J_1 + 4J_2) = -2J_1. \tag{D.11}$$

Alternatively, the vacancy may occupy an interfacial site on top of a white atom in Fig. D.4.(a), in which case the vacancy binding energy becomes

$$E_b^{\{10\}} = 4J_1 - (4J_1 + 4J_2) = -4J_2. \tag{D.12}$$

For a {11} interface the vacancy binding energy is

$$E_b^{\{11\}} = 4J_2 - (4J_1 + 4J_2) = -4J_1. \tag{D.13}$$

With $J_1 = 1$ and $J_2 = -\frac{1}{2}$ the binding energy to a {11} interface is negative, which means that the vacancy prefers to stay in the disordered matrix rather than at the interface. For a {10} interface the sign of the binding energy is site dependent.

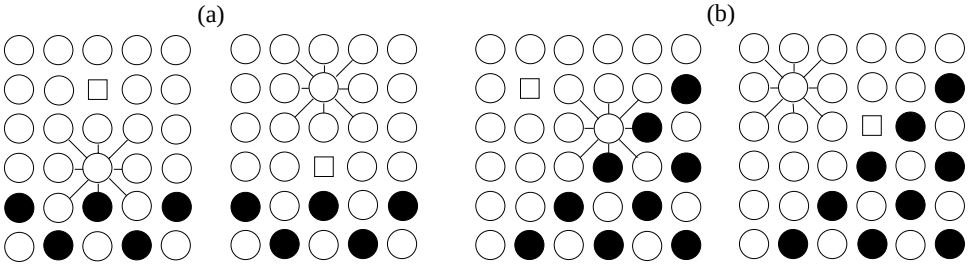


Figure D.4: Vacancy binding to (a) {10} and (b) {11} interfaces. The marked bonds contribute to the energy difference, when the vacancy binding energies are determined in Eq. (D.6).

Bibliography

[1] D.A. Porter, K.E. Easterling, *Phase Transformations in Metals and Alloys*, Chapman & Hall, London (1992).

[2] D.L. Anton, Ni_3Al in Nickel-based superalloys, in *Intermetallic Compounds*, Vol. 2, ed. by J.H. Westbrook and R.L. Fleischer, John Wiley (1994).

[3] J.W. Cahn, J.E. Hilliard, Free energy of a non-uniform system. I. Interfacial free energy, J. Chem. Phys. **28**, 258 (1958).

[4] J.W. Cahn, J.E. Hilliard, Free energy of a non-uniform system. III. Nucleation in a two-component incompressible fluid, J. Chem. Phys. **31**, 688 (1959).

[5] J.W. Cahn, On spinodal decomposition, Acta Metall. **9**, 795 (1961).

[6] J.W. Cahn, On spinodal decomposition in cubic crystals, Acta Metall. **10**, 179 (1962).

[7] G. Arfken, *Mathematical Methods for Physicists*, Third Edition, Academic Press, London (1985).

[8] Y. Wang, L.Q. Chen, A.G. Khachaturyan, Modeling of dynamical evolution of micro/mesoscopic morphological patterns in coherent phase transformations, in *Computer Simulation in Materials Science*, ed. by H.O. Kirchner *et al.*, Kluwer, London (1996).

[9] A.G. Khachaturyan, *Theory of Structural Transformations in Solids*, Wiley, New York (1983).

[10] H. Metiu, K. Kitahara, J.Ross, Stochastic theory of the kinetics of the phase transitions, J. Chem. Phys. **64**, 292 (1976).

[11] H. Metiu, K. Kitahara, J.Ross, A derivation and comparison of two equations (Landau-Ginzburg and Cahn) for the kinetics of phase transitions, J. Chem. Phys. **65**, 393 (1976).

[12] K. Kitahara, H. Metiu, J. Ross, A stochastic theory of cluster growth in homogeneous nucleation, J. Chem. Phys. **63**, 3156 (1975).

[13] E. Salje, Kinetic rate laws as derived from order parameter theory I: Theoretical concepts, Phys. Chem. Min. **15**, 336 (1988).

[14] M.A. Carpenter, E. Salje, Time-dependent Landau theory for order/disorder processes in minerals, Mineral. Mag. **53**, 483 (1989).

[15] S. Dattagupta, V. Heine, S. Marais, E. Salje, A rate equation for atomic ordering in mean field theory: I. Uniform case, J. Phys. Cond. Matt. **3**, 2963 (1991).

[16] S. Dattagupta, V. Heine, S. Marais, E. Salje, A rate equation for atomic ordering in mean field theory: II. General considerations, J. Phys. Cond. Matt. **3**, 2975 (1991).

[17] G. Martin, Atomic mobility in Cahn's diffusion model, Phys. Rev. B **41**, 2279 (1990).

[18] V.G. Vaks, S.V. Beiden, V. Yu. Dobretsov, Mean-field equations for configurational kinetics of alloys at arbitrary degree of non-equilibrium, JETP Lett. **61**, 68 (1995).

[19] G. Martin, P. Bellon, F. Soisson, Modelling diffusion controlled solid state kinetics in equilibrium and driven alloys, Defect and Diffusion Forum **143-147**, 385 (1997).

[20] L.Q. Chen, J.A. Simmons, Microscopic master equation approach to diffusional transformations in inhomogeneous systems - single-site approximation and direct exchange mechanism, Acta Metall. Mater. **42**, 2943 (1994).

[21] L.Q. Chen, Thermodynamics and kinetics of order-disorder processes derived from cluster activation method and microscopic diffusion theory, Phys. Rev. B **49**, 3791 (1994).

[22] C. Geng, L.Q. Chen, Computer simulation of vacancy segregation during spinodal decomposition and Ostwald ripening, Scripta Metall. Mater. **31**, 1507 (1994).

[23] C. Geng, L.Q. Chen, Spinodal decomposition and pattern formation near crystalline surface, Surf. Sci. **355**, 229 (1996).

[24] G.H. Vineyard, Theory of order-disorder kinetics, Phys. Rev. **102**, 981 (1956).

[25] P.M. Chaikin, T.C. Lubensky, *Principles of condensed matter physics*, Cambridge University Press, Cambridge (1995).

[26] E.K.H. Salje, Application of Landau theory for the analysis of phase transitions in minerals, Phys. Reports **215**, 49 (1992).

[27] A.G. Khachaturyan, S. Semenovskaya, T. Tsakalos, Elastic strain energy of inhomogeneous solids, Phys. Rev. B **52**, 15909 (1995).

[28] C. Zener, Theory of strain interaction of solute atoms, Phys. Rev. **74**, 639 (1948).

[29] H.E. Cook, D. De Fontaine, On the elastic free energy of solid solutions I. Microscopic theory, Acta Metall. **17**, 915 (1969).

[30] H. Yamauchi, D. De Fontaine, Elastic interaction of defect clusters with arbitrary strain fields in an anisotropic continuum, Acta Metall. **27**, 763 (1979).

[31] J.R. Willis, T.J. Gosling, Real-space lattice statics description of a random lattice, in *Mathematics of Microstructure Evolution*, ed. by L.Q. Chen *et al.*, EMPMD Monograph Series **4**, The Minerals, Metals & Materials Society (1996).

[32] J.K. Lee, Coherency strain analyses via a discrete atom method, Scripta Metall. Mater. **32**, 559 (1995).

[33] A. Onuki, Ginzburg-Landau approach to elastic effects in the phase separation of solids, J. Phys. Soc. Japan **58**, 3065 (1989).

[34] A. Onuki, Long-range interactions through elastic fields in phase-separating solids, J. Phys. Soc. Japan **58**, 3069 (1989).

[35] H. Nishimori, A. Onuki, Pattern formation in phase-separating alloys with cubic symmetry, Phys. Rev. B **42**, 980 (1990).

[36] A.M. Bratkovsky, E.K.H. Salje, S.C. Marais, V. Heine, Strain coupling as the dominant interaction in structural phase transitions, Phase Trans. **64**, 79 (1995).

[37] A.M. Bratkovsky, V. Heine, E.K.H. Salje, Strain effects, particularly in phase transitions, Phil. Trans. R. Soc. London A **354**, 2875 (1996).

[38] F.R.N. Nabarro, Rafting in superalloys, Met. Mat. Trans. A **27**, 513 (1996).

[39] F.R.N. Nabarro, C.M. Cress, P. Kotschy, The thermodynamic driving force for rafting in superalloys, Acta Mater. **44**, 3189 (1996).

[40] J.C. Chang, S.M. Allen, Elastic energy changes accompanying rafting in nickel-base superalloys, J. Mater. Res. **6**, 1843 (1991).

[41] L.Q. Chen, A.G. Khachaturyan, Computer simulation of structural transformations during precipitation of an ordered intermetallic phase, Acta Metall. Mater. **39**, 2533 (1991).

[42] L.Q. Chen, A.G. Khachaturyan, Formation of virtual ordered states along a phase-decomposition path, Phys. Rev. B **44**, 4681 (1991).

[43] L.Q. Chen, A.G. Khachaturyan, Kinetics of virtual phase transformation during precipitation of ordered intermetallics, Phys. Rev. B **46**, 5899 (1992).

[44] L. Reinhard, P.E.A. Turchi, Transient ordered states in phase-separating alloys, Phys. Rev. Lett. **72**, 120 (1994).

[45] A.G. Khachaturyan, S.V. Semenovskaya, J.W. Morris Jr., Theoretical analysis of strain-induced shape changes in cubic precipitates during coarsening, Acta Metall. **36**, 1563 (1988).

[46] M. McCormack, A.G. Khachaturyan, J.W. Morris Jr., A two-dimensional analysis of the evolution of coherent precipitates in elastic media, Acta Metall. Mater. **40**, 325 (1992).

[47] Y. Wang, L.Q. Chen, A.G. Khachaturyan, Strain-induced modulated structures in two-phase cubic alloys, Scripta Metall. Mater. **25**, 1969 (1991).

[48] Y. Wang, L.Q. Chen, A.G. Khachaturyan, Particle translational motion and reverse coarsening phenomena in multiparticle systems induced by a long range elastic interaction, Phys. Rev. B **46**, 11194 (1992).

[49] L.Q. Chen, Y. Wang, A.G. Khachaturyan, Kinetics of tweed and twin formation during an ordering transition in an substitutional solid solution, Phil. Mag. Lett. **65**, 15 (1992).

[50] L.Q. Chen, Y. Wang, A.G. Khachaturyan, Transformation-induced elastic strain effect on the precipitation kinetics of ordered intermetallics, Phil. Mag. Lett. **64**, 241 (1991).

[51] Y. Wang, L.Q. Chen, A.G. Khachaturyan, Shape evolution of a precipitate during strain-induced coarsening - a computer simulation, Scripta Metall. Mater. **25**, 1387 (1991).

[52] Y. Wang, L.Q. Chen, A.G. Khachaturyan, Kinetics of strain-induced morphological transformation in cubic alloys with a miscibility gap, Acta Metall. Mater. **41**, 279 (1993).

[53] L.Q. Chen, A.G. Khachaturyan, Dynamics of simultaneous ordering and phase separation and effect of long-range Coulomb interactions, Phys. Rev. Lett. **70**, 1477 (1993).

[54] S. Semenovskaya, A.G. Khachaturyan, Kinetics of strain-related morphology transformation in $YBa_2Cu_3O_{7-\delta}$, Phys. Rev. Lett. **67**, 2223 (1991).

[55] S. Semenovskaya, A.G. Khachaturyan, Structural transformations in nonstoichiometric $YBa_2Cu_3O_{6+\delta}$, Phys. Rev. B **64**, 241 (1991).

[56] S. Semenovskaya, Y. Zhu, M. Suenaga, A.G. Khachaturyan, Twin and tweed microstructures in $YBa_2Cu_3O_{7-\delta}$ doped by trivalent cations, Phys. Rev. B **47**, 12182 (1993).

[57] J.W. Christian, *The Theory of Transformations in Metals and Alloys*, Pergamon Press, Oxford (1975).

[58] M. Arita, M. Koiwa, S. Ishioka, Diffusion mechanism in ordered alloys - a detailed analysis of six-jump vacancy cycle in a two-dimensional ordered lattice, Trans. JIM **29**, 439 (1988).

[59] M. Arita, M. Koiwa, S. Ishioka, Diffusion mechanisms in ordered alloys - a detailed analysis of six-jump vacancy cycle in the B2 type lattice, Acta Metall. **37**, 1363 (1989).

[60] Z.W. Lai, G.F. Mazenko, O.T. Valls, Classes for growth kinetics problems at low temperatures, Phys. Rev. B **37**, 9481 (1988).

[61] A.B. Bortz, M.H. Kalos, J.L. Lebowitz, A new algorithm for Monte Carlo simulation of Ising spin systems, J. Comp. Phys. **17**, 10 (1975).

[62] M. A. Novotny, A new approach to an old algorithm for the simulation of Ising-like systems, Computers in Physics **9**, 46 (1995).

[63] W.M. Young, E.W. Elcock, Monte Carlo studies of vacancy migration in binary ordered alloys: I, Proc. Phys. Soc. **89**, 735 (1966).

[64] M. Athénes, P. Bellon, G. Martin, Identification of novel diffusion cycles in B2 ordered phases by Monte Carlo simulation, Phil. Mag. A **76**, 565 (1997).

[65] C.C. Battaille, D.J. Srolovitz, J.E. Butler, A kinetic Monte Carlo method for the atomic-scale simulation of chemical vapor deposition: application to diamond, J. Appl. Phys. **82**, 6293 (1997).

[66] T.F. Lindsey, B. Fultz, Microstructural dependence of vacancy diffusion in ordered alloys, J. Appl. Phys. **75**, 1467 (1994).

[67] P. Fratzl, O. Penrose, Ising model for phase separation in alloys with anisotropic elastic interaction I. Theory, Acta Metall. Mater. **43**, 2921 (1995).

[68] P. Fratzl, O. Penrose, Ising model for phase separation in alloys with anisotropic elastic interaction II. A computer experiment, Acta Mater. **44**, 3227 (1996).

[69] M. Hagen, M.W. Finnis, Point defects and chemical potentials in ordered alloys, Phil. Mag. A **77**, 447 (1998).

[70] S. Marais, V. Heine, C. Nex, E. Salje, Phenomena due to strain coupling in phase transitions, Phys. Rev. Lett. **66**, 2480 (1991).

[71] S. Marais, E. Salje, V. Heine, Kinetic rate laws derived from order parameter theory V: computer simulations of ordering processes using a soft Ising model, Phys. Chem. Minerals **18**, 180 (1991).

[72] J.W. Martin, R.D. Doherty, *Stability of Microstructure in Metallic Systems*, Cambridge University Press, Cambridge (1976).

[73] I.M. Lifshitz, V.V. Slyozov, The kinetics of precipitation from supersaturated solid solutions, J. Phys. Chem. Solids **19**, 35 (1961).

[74] C. Wagner, Theorie der Alterung von Niederschlägen durch Umlösen (Ostwald-Reifung), Z. Elektrochem. **65**, 581 (1961).

[75] R.D. Vengrenovitch, On the Ostwald ripening theory, Acta Metall. **30**, 1079 (1982).

[76] A.J. Bray, Theory of phase-ordering kinetics, Adv. Physics **43**, 357 (1994).

[77] A.P. Sutton, R.W. Balluffi, *Interfaces in Crystalline Materials*, Oxford University Press, Oxford (1995).

[78] D. Huse, Corrections to late-stage behaviour in spinodal decomposition, Lifshitz-Slyozov scaling and Monte Carlo simulations, Phys. Rev. B **34**, 7845 (1986).

[79] K. Yaldram, K. Binder, Spinodal decomposition of a two-dimensional model alloy with mobile vacancies, Acta Metall. Mater. **39**, 707 (1991).

[80] P. Fratzl, O. Penrose, Kinetics of spinodal decomposition in the Ising model with vacancy diffusion, Phys. Rev. B **50**, 3477 (1994).

[81] P. Fratzl, O. Penrose, Reply to " Comment on 'Kinetics of spinodal decomposition in the Ising model with vacancy diffusion' " , Phys. Rev. B **53**, 2890 (1996).

[82] C. Frontera, E. Vives, A. Planes, Monte Carlo study of the relation between vacancy diffusion and domain growth in two-dimensional binary alloys, Phys. Rev. B **48**, 9321 (1993).

[83] C. Frontera, E. Vives, T. Castán, A. Planes, Comment on "Kinetics on spinodal decomposition in the Ising model with vacancy diffusion", Phys. Rev. B **53**, 2886 (1996).

[84] J.G. Amar, F.E. Sullivan, R.D. Mountain, Monte Carlo study of growth in the two-dimensional spin-exchange kinetic Ising model, Phys. Rev. B **37**, 196 (1988).

[85] K. Binder, D. Stauffer, Theory for the slowing down of the relaxation and spinodal decomposition of binary mixtures, Phys. Rev. Lett. **33**, 1006 (1974).

[86] K. Binder, Theory for the dynamics of "clusters". II. Critical diffusion in binary systems and the kinetics of phase separation, Phys. Rev. B **15**, 4425 (1977).

[87] K. Binder, D. Stauffer, Statistical theory of nucleation, condensation and coagulation, Adv. Physics **25**, 343 (1976).

[88] K. Binder, M.H. Kalos, "Critical clusters" in a supersaturated vapor: theory and Monte Carlo simulation, J. Stat. Phys. **22**, 363 (1980).

[89] P. Fratzl, O. Penrose, Competing mechanisms for precipitate coarsening in phase separation with vacancy dynamics, Phys. Rev. B **55**, R6101 (1997).

[90] F. Soisson, A. Barbu, G. Martin, Monte Carlo simulation of copper precipitation in dilute iron-copper alloys during thermal ageing and under electron irradiation, Acta Mater. **44**, 3789 (1996).

[91] A. Cerezo, J.M. Hyde, M.K. Miller, S.C. Petts, R.P. Setna, G.D.W. Smith, Atomistic modelling of diffusional phase transformations, Phil. Trans. R. Soc. Lond. A **341**, 313 (1992).

[92] K. Binder, D.W. Heerman, *Monte Carlo Simulation in Statistical Physics*, Springer-Verlaag, Berlin (1988).

[93] H. Tanaka, A new coarsening mechanism of droplet spinodal decomposition, J. Chem. Phys. **103**, 2361 (1995).

[94] V. Yu. Dobretsov, V.G. Vaks, G. Martin, Kinetic features of phase separation under alloy ordering, Phys. Rev. B **54**, 3227 (1996).

[95] J.M. Hyde, A.P. Sutton, J.R.G. Harris, A. Cerezo, A. Gardiner, Modelling spinodal decomposition at the atomic scale: beyond the Cahn-Hilliard model, Modell. Sim. Mat. Sci. Eng. **4**, 33 (1996).

[96] J.D. Gunton, M. San Miguel, P. Sahni, The dynamics of first-order phase transitions, in *Phase Transitions and Critical Phenomena*, Vol. 8, ed. by C. Domb and J.H. Lebowitz, Academic, London (1983).

[97] J.L. Lebowitz, J. Marro, M.H. Kalos, Dynamical scaling of structure function in quenched binary alloys, Acta Metall. **30**, 297 (1982).

[98] P. Fratzl, J.L. Lebowitz, O. Penrose, J. Amar, Scaling functions, self-similarity and the morphology of phase-separating systems, Phys. Rev. B **44**, 4794 (1991).

[99] K. Binder, M. Bowker, J.E. Inglesfield, P.J. Rous, *Cohesion and Structure of Surfaces*, Elsevier, Amsterdam (1995).

[100] V.I. Gorentsveig, P. Fratzl, J.L. Lebowitz, Kinetics of joint ordering and decomposition in binary alloys, Phys. Rev. B **55**, 2912 (1997).

[101] H. Bakker, On diffusion kinetics in ordered binary alloys, Phil. Mag. A **40**, 525 (1979).

[102] G. Yu, K. Lücke, On the theory of short range ordering kinetics under special consideration of correlation effects, Acta Metall. Mater. **40**, 2523 (1992).

[103] C.C. Wang, S.A. Akbar, Diffusion in ordered alloys and intermetallic compounds, Acta Metall. Mater. **41**, 2807 (1993).

[104] B. Fultz, Suppressed kinetics of short range ordering at low temperatures, J. Chem. Phys. **87**, 1604 (1987).

[105] P.D. Sahni, J.D. Gunton, S.L. Katz, R.H. Timpe, Dynamics of phase separation in two-dimensional tricritical systems Phys. Rev. B **25**, 389 (1982).

[106] M. Athénes, P. Bellon, G. Martin, F. Haider, A Monte Carlo study of B2 ordering and precipitation via vacancy mechanism in B.C.C. lattices, Acta Mater. **12**, 4739 (1996).

[107] M. Athénes, P. Bellon, G. Martin, F. Haider, Monte Carlo simulation of simultaneous ordering and precipitation in BCC lattice, J. Physique IV **6**, C2-53 (1996).

[108] E. Vives, A. Planes, Kinetics of vacancy-driven order-disorder transition in a two-dimensional binary alloy, Phys. Rev. Lett. **68**, 812 (1992).

[109] E. Vives, A. Planes, Vacancy-driven ordering in a two-dimensional binary alloy, Phys. Rev. B **47**, 2557 (1993).

[110] J. Marro, A.B. Bortz, M.H. Kalos, J.L. Lebowitz, Time evolution of a quenched binary alloy. II Computer simulation of a three-dimensional model system, Phys. Rev. B **12**, 2000 (1975).

[111] M. Athénes, P. Bellon, G. Martin, Monte Carlo simulation of diffusion in B2 ordered phase, Defect and Diffusion Forum **143-147**, 297 (1997).

[112] G. Martin, P. Bellon, Driven alloys, Solid State Phys. **50**, 189 (1997).

[113] Y. Grandjean, P. Bellon, G. Martin, Kinetic model for equilibrium and nonequilibrium segregation in concentrated alloys under irradiation, Phys. Rev. B **50**, 4228 (1994).

[114] P. Bellon, Y. Grandjean, G. Martin, R.S. Averback, Atomistic modeling of kinetics in intermetallics, J. Physique IV **6**, C2-11 (1996).

[115] J. Gayda, D.J. Srolovitz, A Monte Carlo finite-element model for strain energy controlled microstructural evolution: "rafting" in superalloys, Acta Metall. **37**, 641 (1989).

[116] D.J. Arrell, J.L. Vallés, Interfacial dislocation based criterion for the prediction of rafting behavior in superalloys, Scripta Metall. Mater. **30**, 149 (1994).

[117] J.L. Vallés, D.J. Arrell, Monte Carlo simulation of anisotropic coarsening in nickel-base superalloys, Acta Metall. Mater. **42**, 2999 (1994).